SINGLE-WALLED METAL OXIDE NANOTUBES AND NANOTUBE MEMBRANES FOR MOLECULAR SEPARATIONS

A Thesis
Presented to
The Academic Faculty

by

Dun-Yen Kang

In Partial Fulfillment
of the Requirements for the Degree
Doctor of Philosophy in the
School of Chemical & Biomolecular Engineering

Georgia Institute of Technology
August 2012

SINGLE-WALLED METAL OXIDE NANOTUBES FOR MOLECULAR SEPARATIONS

Approved by:

Dr. Sankar Nair, Advisor
School of Chemical & Biomolecular Engineering
Georgia Institute of Technology

Dr. Christopher W. Jones, Advisor
School of Chemical & Biomolecular Engineering
Georgia Institute of Technology

Dr. Haskell W. Beckham
School of Materials Science and Engineering
Georgia Institute of Technology

Dr. William J. Koros
School of Chemical & Biomolecular Engineering
Georgia Institute of Technology

Dr. David S. Sholl
School of Chemical & Biomolecular Engineering
Georgia Institute of Technology

Date Approved: April, 26th, 2012

To My Grandfather

ACKNOWLEDGMENTS

I would like to thank my thesis advisors, Dr. Christopher Jones and Dr. Sankar Nair for their support, guidance, and inspiration. They have made all the difference in my life. I would like to thank ConocoPhillips for funding this research. I also extend my gratitude to my collaborators, Dr. Johannes Leisen, Dr. Ji Zang, Dr. Nicholas Brunelli, and Ipek Yucelen for their support and scientific discussion.

TABLE OF CONTENTS

LIST OF TABLES

LIST OF FIGURES

SUMMARY

Single-walled nanotubes have been considered essential "building-blocks" in nanotechnology and emerging materials for molecular recognition-based applications, such as molecular sensing, catalysis, and separations. Two critical obstacles in the development of functional nanotube-based devices are: (a) the difficulty of creating diverse functionality at the interior surfaces of single-walled nanotubes, and (b) the lack of effective approaches for fabricating scalable technological platforms with nanotube materials. This thesis describes my work addressing key fundamental issues in nanotube science and technology; particularly regarding the synthesis, characterization, and functionalization of single-walled metal oxide nanotubes (SWNTs) (Chapters 2, 3, 4),and approaches for applying SWNTs in scalable separation platforms for potentially achieving high performance (Chapters 5, 6, 7).

The above, rather ambitious, objectives were addressed in a step-wise manner in this work. First, I acquired a detailed fundamental understanding of the inner surface properties of aluminosilicate SWNTs (Chapter 2).

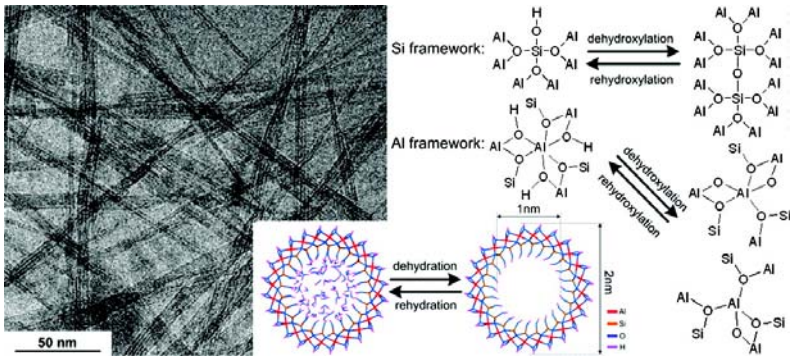

The investigations included elucidating molecular level details of dehydration and dehydroxylation phenomena in aluminosilicate single-walled nanotubes with a combination of several temperature-dependent solid-state characterization techniques. Critical information from this study enables a number of subsequent processes such as interior modification, molecular transport, and controlled delivery of molecules.

In Chapter 3, a successful post-synthesis interior functionalization methodology is discussed, with the appropriately dehydrated or dehydroxylated nanotubes as the starting materials.

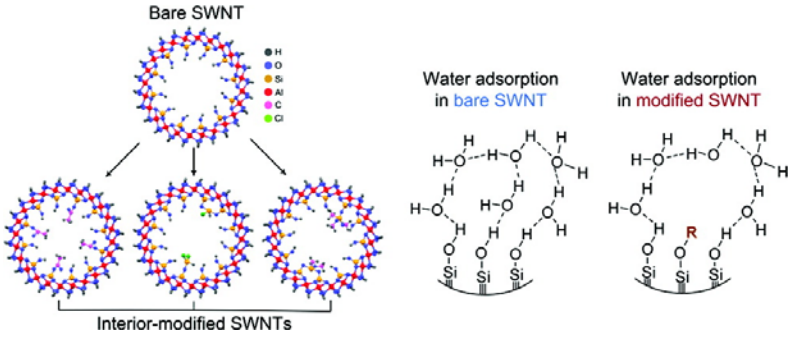

Through surface reactions involving organosilane precursors and the inner wall of the nanotube, diverse organic entities can be immobilized at the inner

surface of aluminosilicate nanotubes and thereby the hydrophilicity and interior surface properties can be tailored. This study was the first unambiguous demonstration of covalent modification of the interior of single-walled nanotube materials.

The investigations in Chapter 4 reveal a direct (*in situ*) route for synthesizing organic-functionalized alumino-silicate nanotubes via the use of organosilanes with functional groups in the synthesis itself (as opposed to post-synthesis modification).

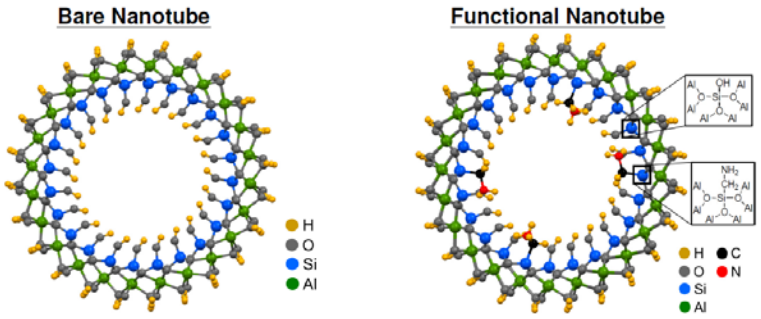

This work creates a one-step route for the incorporation of functional groups at the interior of nanotubes, thus bypassing the limitations of the low functional group loading as well as additional processing steps in the post-synthesis functionalization methodology of Chapter 3. The two functionalization methods developed (post-synthesis and direct functionalization) together may enable a range of applications of nanotube materials, including separations, catalysis, and molecular capture/encapsulation/storage.

The direction of the work then turned to the fabrication of nanotube-containing membranes. In view of the absence of a good predictive model for the performance of nanotube-containing membranes, Chapter 5 describes the development of analytical models for quantitatively predicting the separation properties of composite membranes containing (nano)tubular fillers.

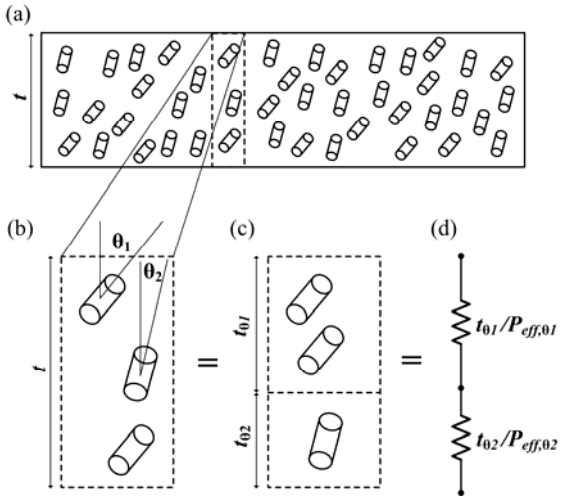

These models provide useful guidance for evaluating/optimizing existing nanotube-based membranes as well as preparing nanotube-based membranes with novel device architectures and enhanced separation performance.

In Chapter 6, the fabrication and characterization of free-standing nanotube/ polymer composite membranes with good organic-inorganic interface adhesion and good nanotube dispersion is discussed.

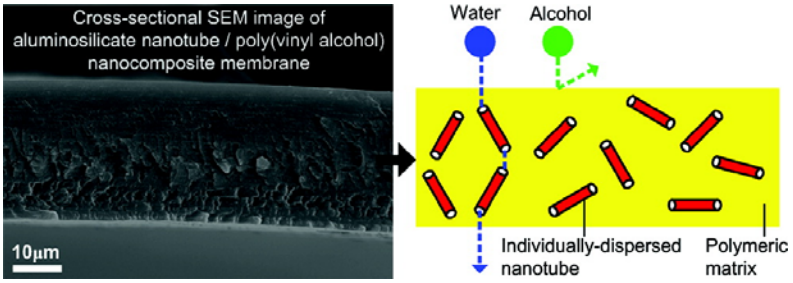

A detailed investigation of the structure and propreties of these membranes (at nano-, micro-, and macro- length scales) is presented. It is shown that hese nanocomposite membranes could be effectively used to construct scalable membrane separation devices. This work is the first demonstration of a defect-free membrane containing well-dispersed nanotube materials. Molecular level insights on the morphological changes of polymer chains due to nanotube incorporation have also been carefully investigated.

In order to further develop nanotube membranes of potential technological interest, Chapter 7 presents the development of prototype thin supported composite membranes (< 500 nm) with bare and amine-functionalized nanotubes, and a preliminary evaluation of their CO_2/CH_4 separation performance.

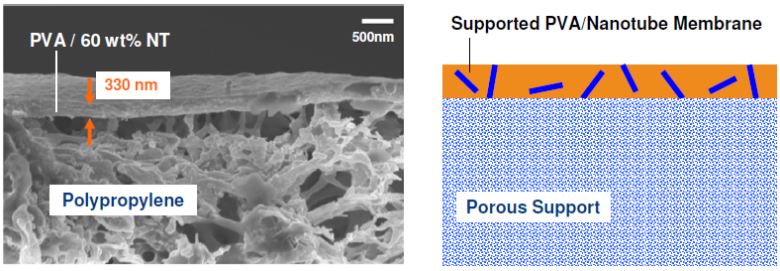

A significant improvement (nearly one order of magnitude) of membrane permeance and slightly enhanced CO_2/CH_4 selectivity (with incorporation of amine-functionalized nanotubes) was observed. Although this prototype thin membrane is far from being optimized, an important finding is that the observed performance enhancement is likely due to a portion of incorporated nanotubes spanning across the membranes, thereby providing direct mass transport pathways for molecules. This study is, for the first time, a demonstration that functional nanotube materials can be incorporated in scalable thin film/membrane platforms and act as molecular transport channels through the thin film.

Chapter 8 presents my conclusions and a brief discussion of potential directions for future research.

CHAPTER 1

INTRODUCTION

1-1 Nanotubes for molecular transport and separations

Nanotubular materials are important "building blocks" of nanotechnology, based upon their incorporation into nanoscale devices. In particular, the synthesis and applications of carbon nanotubes have been extensively studied for two decades.[1-6] One application area has been the use of carbon nanotubes for molecular separations, owing to some of their unique properties. One such important property, extremely fast mass transport of molecules within carbon nanotubes associated with their low friction inner nanotube surfaces, has been demonstrated via computational and experimental studies.[7-11] Furthermore, the behavior of adsorbate molecules in nano-confinement is fundamentally different than in the bulk phase, which could lead to the design of new sorbents.[12-14] Finally, their one-dimensional geometry could allow for alignment in desirable orientations[15-18] for given separation devices to optimize the mass transport. Despite possessing such attractive properties, several intrinsic limitations of carbon nanotubes inhibit their application in large scale separation processes: the high cost of carbon nanotube synthesis and membrane formation (by microfabrication processes), as well as their lack of surface functionality, which significantly limits their molecular selectivity. Although outer-surface modification of carbon nanotubes has been developed for nearly two decades,[19-23] interior modification via covalent chemistry is still challenging due to the low reactivity of the inner-surface. Specifically, forming covalent bonds at inner walls of carbon nanotubes requires a transformation from sp^2 to sp^3 hybridization. The formation of sp^3 carbon is energetically unfavorable for concave surfaces.[23,24] Hence, the interior functionalization of carbon nanotubes remains a challenge.

1-2 Nanotube/polymer nanocomposite membranes

Preparing a nanotube/polymer nanocomposite membrane is a potentially effective way to apply nanotubular materials in industrial-scale molecular transport and separation processes. Polymeric membranes are already prominent for separations applications due to their low fabrication and operation costs.[25-28] However, the main challenge for utilizing polymer membranes for future high-performance separations is to overcome the tradeoff between permeability and selectivity.[26,28] A combination of the potentially high throughput and selectivity of nanotube materials with the processibility and mechanical strength of polymers may allow for the fabrication of scalable, high-performance membranes.[29-32] Although nanotubular materials have been extensively studied for two decades, there are only few reports on the subject of nanotube/polymer membranes with carbon nanotubes as fillers for molecular separation.[33-36] One main challenge in preparing a nanotube/polymer membrane is the intrinsically poor adhesion between bare carbon nanotubes and polymeric materials. A number of studies have been reported on modifying the outer surface of carbon nanotubes to enhance its compatibility with polymers, but no reports have convincingly shown that a defect-free nanocomposite membrane containing carbon nanotubes has been fabricated. Defects in the membrane directly limit selectivity and defeat the advantageous transport properties of the nanotubes.[34]

1-3 Single-walled metal oxide nanotubes

In the above discussion, certain intrinsic drawbacks of carbon nanotubes for molecular separation have been stated: high cost, difficulty of inner-surface modification for improving molecular selectivity, as well as difficulties in outer-surface modification for preparing a defect-free nanocomposite membrane. These high barriers facing the use of carbon nanotubes in membranes can be compared with certain favorable properties of

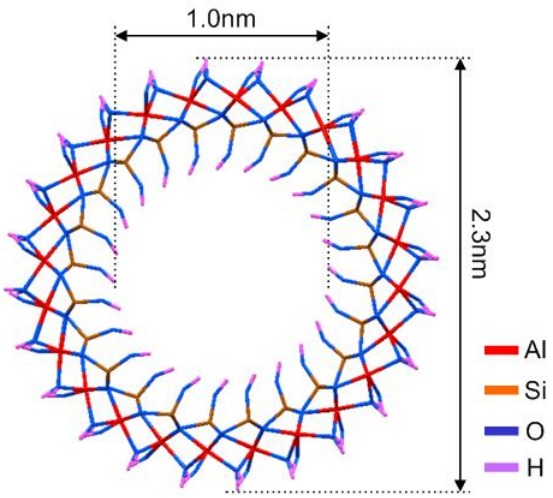

Figure 1.1. Cross-sectional structure of aluminosilicate single-walled nanotube.

metal oxide nanotubes. In particular, metal oxide nanotubes have a much lower cost due to moderate synthesis conditions (usually hydrothermal or solvothermal), higher surface reactivity (similar to a metal oxide or hydroxide) that is advantageous to surface modification, and controllable dimensions (such as length in the ~20-500 nm range), which can allow fabrication of thin membranes.[37,38] In the present work, I will focus on a specific single-walled metal oxide nanotube (SWNT) with an aluminosilicate composition (Figure 1.1). This SWNT is the synthetic analog of the nanotubular mineral imogolite, and has created substantial interest in recent years.[39-43] It possesses several unique and attractive properties for molecular transport and adsorption and membrane formation, such as controllable and monodisperse dimensions,[43,44] extraordinary hydrophilicity and surface silanol density,[45] and fast mass transport (e.g. for water and alcohols).[8,10,46] The inner surface of the aluminosilicate SWNT can be expected to resemble those of metal oxide/hydroxide and silicate materials, and thus are more amenable to surface modification than carbon nanotubes. The aluminosilicate SWNTs contain silanol (Si-OH) groups on the inner surface and hence can potentially be functionalized in a manner analogous to the well-known techniques for functionalization of mesoporous and microporous silicas.[47-50] On the other hand, the hydroxyl groups at the

external surfaces of aluminosilicate SWNTs may possess good affinity to hydrophilic polymers.[51] This could open the route for fabricating high-quality nanotube/polymer membranes.

1-4 Topics of this dissertation

The present work is aimed at addressing the aforementioned key issues regarding metal oxide nanotubes for their application in molecular transport and separation technologies. First, the dehydration and dehydroxylation of aluminosilicate SWNTs is investigated, to determine the appropriate pretreatment conditions prior to the post-synthesis interior surface functionalization (Chapter 2). The inner wall functionalization of aluminosilicate SWNT is achieved via two approaches: post-synthesis functionalization (Chapter 3) and direct functionalization (Chapter 4). In a parallel theoretical development (Chapter 5), a quantitative model is developed for describing the separation performance of nanocomposite membranes containing nanotubular fillers. Aluminosilicate SWNT/polymer membranes (in the form of dense films) of high microstructural quality are prepared, and their separation performance is evaluated (Chapter 6). Finally, in Chapter 7, the preparation of thin (< 500 nm), supported, aluminosilicate SWNT/polymer membranes is demonstrated and a preliminary investigation of their structure and properties is presented. Overall, this dissertation makes a significant step forward in the synthesis, characterization, and processing of nanotubes and nanotube-containing membranes that can be used in molecular transport and separation applications.

CHAPTER 2

DEHYDRATION AND DEHYDROXYLATION OF SINGLE-WALLED ALUMINOSILICATE NANOTUBES

The capability to control the chemistry of the inner surface of the aluminosilicate SWNTs thus has significant implications for molecular transport inside the nanotube. The inner-wall modification is difficult, and no convincing results suggesting inner-wall functionalization have been published. It is hypothesized that the extraordinarily high surface silanol density of the inner wall (~9.1 OH/nm^2)[45] makes the material highly hydrophilic at ambient conditions. The strong binding of water molecules to the inner wall may hinder functionalization of the surface. Therefore, a comprehensive knowledge of dehydration and subsequent dehydroxylation phenomena (due to condensation of hydroxyls) on the SWNT surface is critical for accessing reactive surface sites and for creating a new class of inner-wall functionalized SWNT materials. In this chapter, I report a systematic qualitative and quantitative investigation of dehydration and dehydroxylation phenomena in aluminosilicate SWNTs over a wide temperature range of 25 to 450 °C. The structure and composition of the SWNT are assessed by a combination of techniques including in situ XRD, FTIR, NMR, TGA-MS, and N_2 physisorption. Based upon the results, a quantitative model is proposed for the dehydration and dehydroxylation phenomena occurring in the SWNT upon heat treatment. Furthermore, a unique rehydroxylation phenomenon that occurs in the dehydrated SWNT upon re-exposure to water is elucidated. As a result, this study leads to the preparation of a range of well-characterized heat treated materials amenable to inner-wall surface functionalization.

2-1 Experimental details

2-1-1 SWNT synthesis and purification

Tetraethyl orthosilicate (TEOS) was mixed with aluminum-tri-sec-butoxide in a glovebox filled with nitrogen. The mixture was added to an aqueous 38mM perchloric acid solution with a molar ratio Si:Al:HClO4 = 1.1:2:1, under vigorous stirring at room temperature in ambient conditions for 24 h. The solution was then diluted with DI water by a factor of 3.6 and refluxed at 95 °C for 4 days. Once the temperature was brought to 95 °C, the solution turned from cloudy to clear in about 1 h. After the solution was decreased to room temperature, a 30 wt % ammonia solution was added dropwise into the product solution until gelation of the suspended nanotubes occurred. The gel was isolated by centrifugation at 7000 rpm for 15 min. The supernatant was discarded, and a few drops of 10 N hydrochloric acid were added to the gel, thereby redispersing the nanotubes. The resulting viscous solution was purified by dialysis against DI water for 3 days using a 15000 Dalton membrane. The purified suspension was dried at 60 °C to obtain a powder sample of the SWNTs.

2-1-2 Electronic microscopy

The as-synthesized dialyzed product solution was imaged by cryogenic transmission electronic microscope (cryo-TEM) to confirm the presence of the SWNTs and to obtain clear images of these materials that cannot be obtained by conventional TEM. 4 μL aliquots of single-walled metal oxide (aluminosilicate) nanotubes were applied onto glow-discharged, 200 mesh, holey carbon-coated copper grids (EMSciences, Hatfield, Pennsylvania) and flash-frozen (plunge frozen) in liquid ethane using a Vitrobot Mark II system (FEI, Hillsboro, Oregon). Plunge-frozen samples were stored under liquid nitrogen until viewed in the electron microscope. Cryo-electron micrographs were

collected at the Emory University Robert P. Apkarian Integrated Electron Microscopy Core using a JEOL JEM-1210 microscope operated at 100 kV. The microscope is equipped with a LaB_6 filament and a Gatan CT-3500 cold stage. Images were acquired with a Gatan UltrascanTM 2k × 2k charged-couple device (CCD camera) (Gatan, Inc. Pleasanton, CA).

2-1-3 Thermogravimetric analysis and mass spectroscopy (TGA-MS)

These experiments were performed on a Netzsch STA449 TGA connected to a Netzsch QMS403 mass analyzer. About 20 mg of SWNT sample was heated under He in the range of 25 700 °C.

2-1-4 Nitrogen physisorption

Nitrogen physisorption measurements were performed with a Micromeritics ASAP 2010 at 77 K. The nanotube sample was placed in an analysis tube, degassed, and heat treated at the desired temperature for 12 h in a 25 mTorr vacuum before each measurement. Heat treatments at higher temperatures, e.g., 300 400 °C, were conducted in a separate 15 mTorr vacuum line for 5 h, and the sample was then transferred into the analysis tube in a nitrogen glovebox before degassing and physisorption measurements. To obtain a rehydrated nanotube sample, the sample after heat treatment at 400 °C was cooled to room temperature and allowed to equilibrate in contact with saturated water vapor for 12 h. In contrast to the other characterization methods reported in this chapter (which characterize the rehydrated sample directly), physisorption measurements were made on the rehydrated sample only after it was degassed under vacuum at 250 °C.

2-1-5 Solid-state NMR

The nanotube sample for solid-state NMR experiments was first placed in a flask connected to a 15 mTorr vacuum line and heat treated at the desired temperature for 5 h.

The rehydrated sample was treated as described above. The treated sample was transferred to a nitrogen drybox and packed into a 7-mm rotor capped with one O-ring cap. ^{1}H, ^{27}Al, and ^{29}Si MAS NMR experiments were carried out on a Bruker DSX 300 spectrometer at frequencies of 276.2, 78.1, and 59.6 MHz, respectively. For ^{1}H MAS NMR studies, the sample was spun at 5 kHz. A single pulse of $\pi/2$ and a repetition time of 4 s was used. The sample was spun at 5-6 kHz for ^{27}Al MAS NMR experiments, for which a single pulse of $\pi/6$ and a repetition time of 0.1 s were used. For ^{29}Si MAS NMR, DP and CP measurements were performed with repetition times of 10 and 5 s, respectively, with a $\pi/2$ single pulse and a 5 kHz spinning rate. The chemical shifts of ^{27}Al was referenced to $AlCl_3$ and ^{1}H and ^{29}Si to 3-(trimethylsilyl)-1-propanesulfonic acid sodium salt.

2-1-6 FT-IR

A 2 mg nanotube sample was mixed with 40 mg potassium bromide (KBr) and pressed into a pellet. The sample pellet was placed in a Harrick high temperature cell with KBr windows. The sample pellet was heat treated under a 15-millitorr vacuum at various temperatures ranging from 25-450^{o}C for 5 hours each. The cell was then cooled to room temperature and filled with argon before conducting FT-IR measurements. The FT-IR spectra were obtained on a Bruker IFS 66v/S spectrometer with 256 scans and a resolution of 2 cm^{-1}. Peak area integrations were performed using the OPUS 6.5 program (Bruker).

2-1-7 X-ray diffraction (XRD) measurements and simulations

In situ powder x-ray diffraction (XRD) was performed on PAnalytical X'pert Pro diffractometer operating with a Cu Kα source. The powder sample was placed in an Anton Paar TTK 450 temperature-control chamber. The sample was heat-treated at a desired temperature for 5 hrs under a vacuum of 7.5 militorr, and high-resolution

diffraction data were then rapidly collected with an X'Celerator detector scanning from 2-30^{o} 2θ with a step size of 0.02^{o}. X-ray diffraction simulations were performed using the Reflex module of the Materials Studio 3.2 molecular simulation package (Accelrys, Inc.). A polarization factor of 0.5 was used, assuming the sample is in powder form. The instrumental broadening was accounted for by a well known angle-independent full-width-at-half-maximum (FWHM) expression containing parameters (U, V and W). The values of these three parameters (U=0.6787, V=-0.2563 and W=0.03378), were obtained by fitting the peak shape of the experimental diffraction pattern of LaB_6 (NIST) measured on the same instrument. Atomistically detailed nanotube models with various degrees of hydration were constructed by adapting techniques described in the simulation studies of water adsorption and transport in the aluminosilicate SWNTs.[10,46] The XRD simulations were carried out with atomistically detailed models of nanotube bundles containing various numbers of nanotubes in different bundling patterns (hexagonal, monoclinic, and orthogonal).

2-2 Aluminosilicate SWNT morphology and thermogravimetric analysis

The cryo-TEM images of as-made aluminosilicate SWNTs are shown in Figure 2.1. The as-synthesized SWNT samples possess monodispersed diameter.

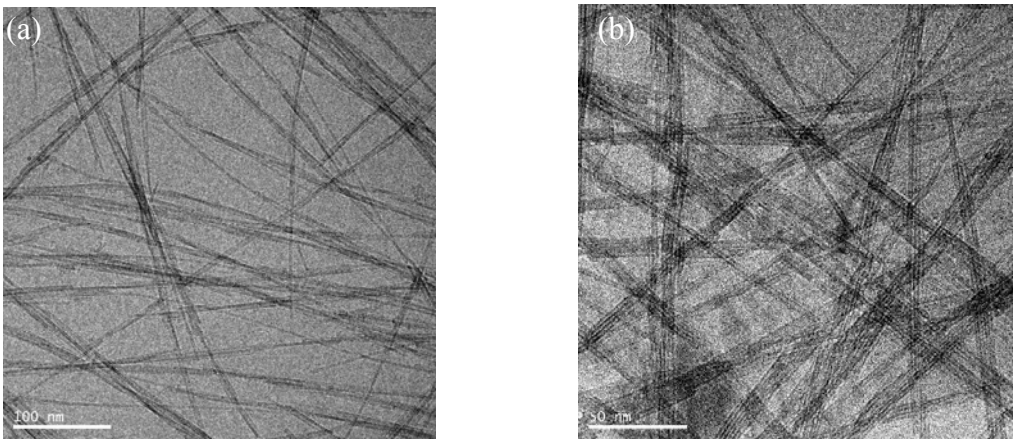

Figure 2.1. Cryo-TEM images of as-synthesized aluminosilicate SWNTs with (a) low and (b) high magnification.

I investigated aluminosilicate SWNT dehydration and dehydroxylation phenomena by TGA-MS (Figure 2.2). According to the TGA and differential TGA curves, there are two pronounced weight losses at around 100°C and 350°C. These can be clearly assigned to dehydration and dehydroxylation respectively. Simultaneously, the molecular weight channels 17 (corresponding to OH) and 18 (H_2O) in the mass spectrum showed two sets of concurrent peaks. The ratio of the integrated ionic current of channel 17 and 18 is around 0.25. These observations represent a well-known signature of water molecules,[52] and it is therefore clear that water molecules leave the nanotube during the entire measurement (25-700°C). Furthermore, the trends of both ionic current channels agree with the differential TGA curve. Therefore, it can be concluded that the SWNT dehydration is complete by about 250°C, and the subsequent dehydroxylation reaches its maximum rate at about 340°C.

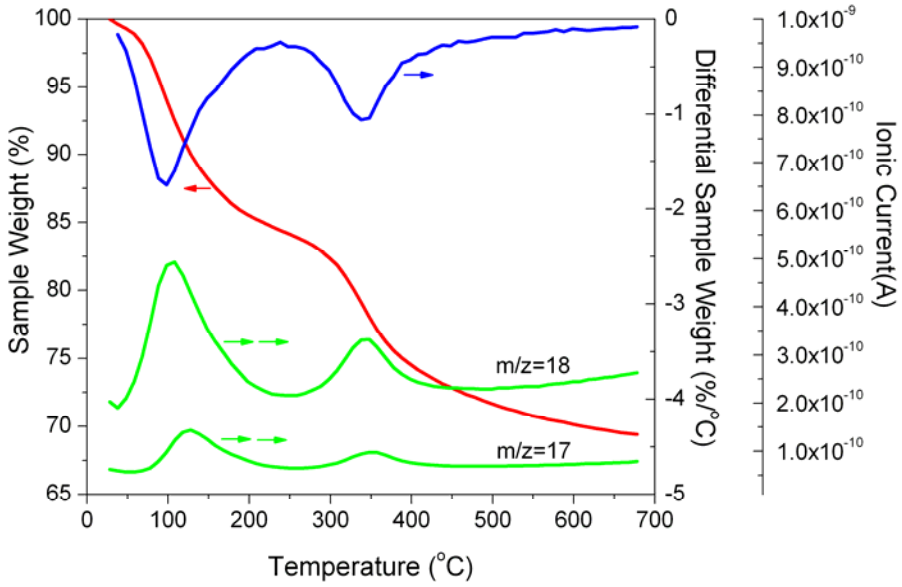

Figure 2.2. TGA, differential TGA, and TGA/MS ionic current traces. The ratio of ionic current between channels *m/z* =18 and *m/z* =17 clearly indicates that both weight losses from SWNT correspond to water molecules leaving the pores.

2-3 Solid-state NMR

^{1}H NMR is an excellent probe of the hydrogen environment in the aluminosilicate SWNTs. The ^{1}H NMR investigation is summarized in Figure 2.3.

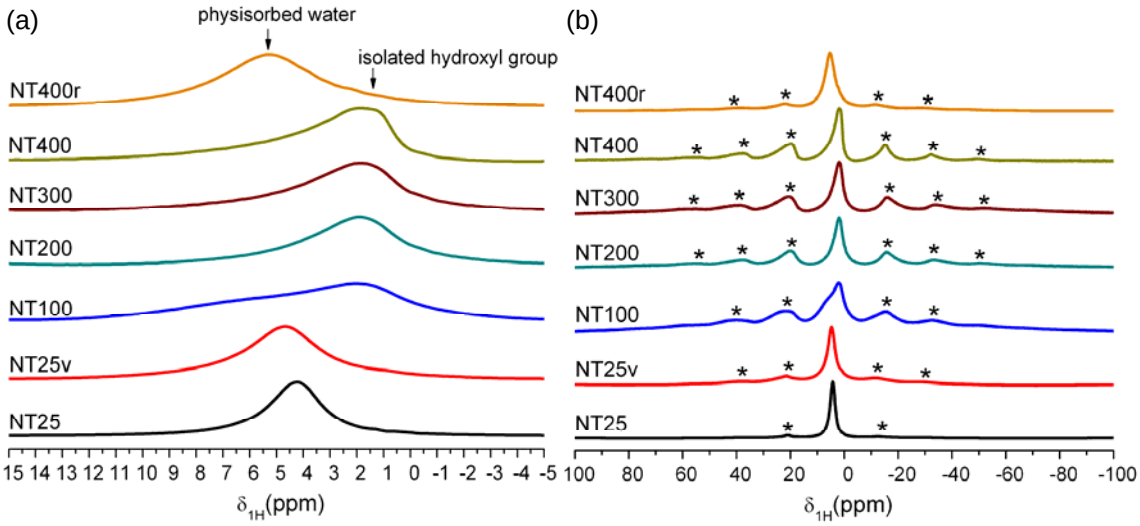

Figure 2.3. (a) ^{1}H NMR for the SWNT sample in different pre-treated conditions. Sample NT25 is the original SWNT sample, NT25v is the same sample after degassing at room temperature under vacuum, and samples NT100-NT400 represent samples heat treated at the corresponding temperatures (100-400°C). NT400r represents the rehydrated sample. (b) A larger spectral region of ^{1}H NMR including spinning side-bands, denoted by asterisks, for the SWNT sample heat-treated at different temperatures.

Sample NT25 is the original SWNT sample, NT25v is the same sample after degassing at room temperature under vacuum, and samples NT100-NT400 represent samples heat treated at the corresponding temperatures (100-400°C). NT400r represents the rehydrated sample. Two peaks are observed in the spectra (Figure 2.3a): the peak between 4-6 ppm is assigned to protons from physisorbed water in the pore of the

aluminosilicate SWNT, whereas the peak at ~1.8 ppm is assigned to the isolated hydroxyl groups.[53-55] For samples containing a significant amount of physisorbed water (NT25, NT25v, and NT400r), the NMR signal from water dominates the spectra. On the other hand, for "anhydrous" samples such as NT200, NT300 and NT400, the spectra are dominated by the NMR signal from isolated hydroxyl groups. A clear transition region, wherein the two peaks are of similar magnitude, is observed in the sample NT100. Furthermore, the above peak assignment can be further confirmed by the larger spectral region including spinning side-bands, as summarized in Figure 2.3b. Previous studies suggest that the relative intensity of the central band and the spinning side-band in ^{1}H solid-state NMR spectra strongly correlates to the concentration and mobility of the protons in the system.[56-58] A higher proton concentration and mobility lead to a higher intensity of the central band relative to the spinning side-band. There is a monotonic increase of the relative intensities of the spinning side-band and the central band from sample NT25 to NT 400v, when the SWNT sample undergoes dehydration and subsequent dehydroxylation. This observation is due to two factors: the loss of protons during heat-treatment, and the loss of more mobile protons present in physisorbed water (in comparison to protons from hydroxyl groups) during dehydration.

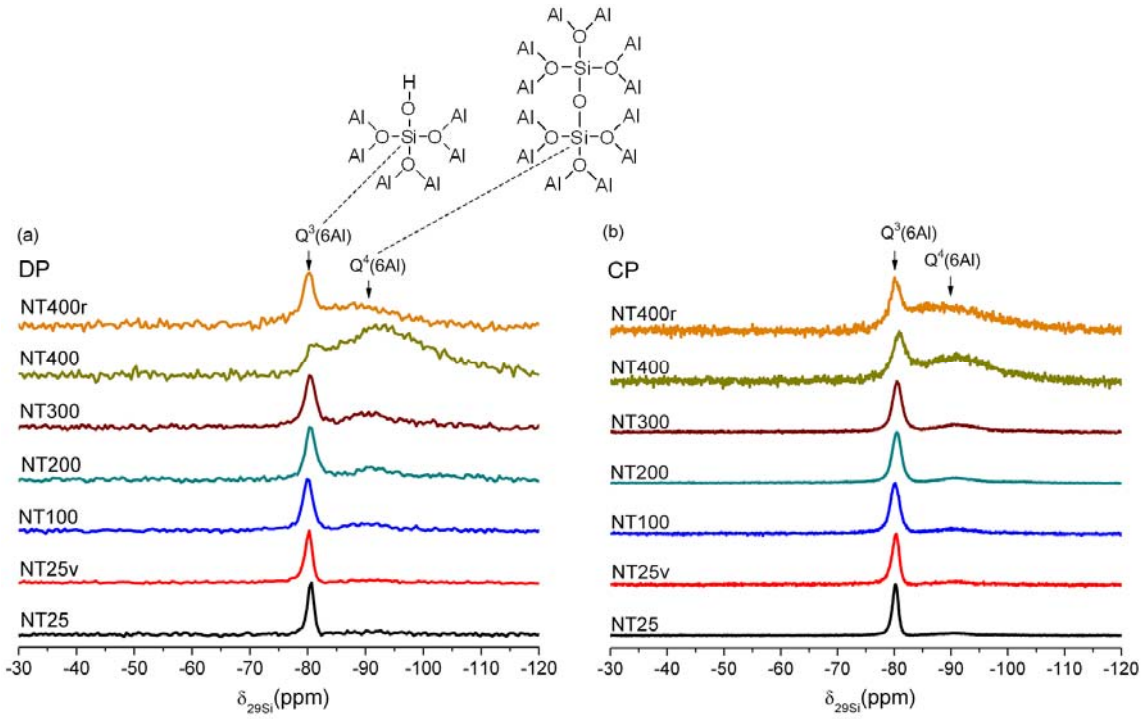

Figure 2.4. (a) ^{29}Si direct-polarized (DP) NMR and (b) ^{29}Si cross-polarized (CP) NMR for SWNT samples heat-treated at different temperatures.

Direct polarization (DP-) and cross polarization (CP-) ^{29}Si NMR were then used to provide a molecular-level understanding of the interior wall structure of the SWNT during heat treatment (Figures 2.4a and 2.4b). In the case of CP-NMR, the signal is enhanced by the presence of protons in proximity to the silicon atoms. In the original SWNT sample (NT25), only one peak located at -79 ppm is seen and is assigned to Q^3(6Al), in good agreement with the study of Frost et al.[59] In the heat-treated samples a second, broader peak around -90 ppm is observed, its intensity being relatively insignificant for NT100-NT300 but becoming prominent for NT400. This peak was rationalized in previous works as a structural transformation from imogolite (SWNT) into a non-tubular material called allophane,[60,61] based upon the similarity of the NMR spectrum to that of allophone. However, the transformation of tubular imogolite into non-tubular allophane would be expected to involve drastic and irreversible morphological

and structural changes in the ^{27}Al NMR spectra, vibrational spectra, XRD patterns, and N_2 physisorption isotherms. Since such irreversible and drastic changes are not observed (as discussed below), and considering the fact that the inner wall of the imogolite SWNT and the allophane have a very similar silanol structure,[62,63] it is more appropriate to assign the broad peak at -90 ppm to the condensation of adjacent silanols, thus leading to a transformation of the Si coordination environment from Q^3(6Al) into Q^4(6Al). The latter is more shielded than Q^3(6Al) and is well-known to show an up-field chemical shift.[64,65] Furthermore, the CP-NMR spectra show a more pronounced Q^3(6Al) peak in relation to the Q^4(6Al) peak. This is clear due to the enhancement of the former peak by a proximal proton coming from silanol group, whereas this is not possible for the Q^4(6Al) signal from fully condensed silanols. When the SWNT sample is rehydrated (NT400r), a distinct change (in comparison to NT400) occurs. The Q^3(6Al) signal dominates the spectrum again, as in the samples NT25-NT300. This is clear evidence of a rehydroxylation phenomenon, wherein most of the condensed Q^4(6Al) silicon atoms in NT400 are transformed (by hydrolysis) back into silanols when the anhydrous dehydroxylated sample is re-exposed to moisture. Note that there is no obvious difference between the DP-NMR and CP-NMR spectra for NT400r, since the protons from the hydroxyl group can enhance the Q^3(6Al) signal whereas the protons from physisorbed water are able to enhance the Q^4(6Al) signal.

Based on the initial chemical composition of the inner wall, I can quantitatively summarize the dehydroxylation and rehydroxylation phenomena of the SWNT interior in the following scheme:

$$SiO_{2.5}H \underset{\text{re-exposed to moisture}}{\overset{\text{heat}}{\rightleftharpoons}} (1-x)SiO_{2.5}H + xSiO_2 + 0.5xH_2O \quad (2.1)$$

where $0 \leq x \leq 1$. The value of x is obtained from the ratio of the integrated Q^3(6Al) and Q^4(6Al) peak areas in DP spectra. The value of x = 0.04, 0.20, and 0.73 for NT25,

NT300, and NT400 respectively, corresponding to the increasing condensation of silanols upon heat treatment. Upon rehydroxylation to yield sample NT400r, the value of x falls to 0.29.

While ^{29}Si NMR elucidates structural changes in the interior of the SWNT, ^{27}Al NMR (Figure 2.5) gives information on structural changes occurring in the nanotubular gibbsite (aluminum hydroxide) layer comprising its outer surface. The peak at 4 ppm is assigned to the octahedrally coordinated aluminum, which is the only type of aluminum present in the purified original SWNT material (NT25).[61] The spectra remain unchanged until NT400, wherein a broad shoulder is observed. When the anhydrous dehydroxylated SWNT sample is rehydroxylated (NT400r), the shoulder further resolves into clear peaks at 30 ppm and 60 ppm. The peak at 60 ppm is clearly assigned to tetrahedral aluminum[66,67] whereas there are several possible assignments for the peak at 30 ppm. Previous studies suggest that the peak in the range of 20-50 ppm can be reasonably assigned to distorted-tetrahedral aluminum,[68,69] distorted-octahedral aluminum,[66] or penta-coordinated alumunim.[70,71] In the following discussion, the peak at 30 ppm was assigned to penta-coordinated aluminum in analogy to the structural transformation of gibbsite under calcination. The detailed study shows that it is appropriate to attribute the penta-coordinate Al to local changes in the structure of the SWNT due to (reversible) condensation of a fraction of the silanol groups and a concomitant (irreversible) decrease in the coordination environment of a fraction of the aluminum atoms.

Based upon the ^{27}Al spectra, I propose a model for the (irreversible) SWNT dehydroxylation at the outer surface:

$$Al_2O_{4.5}H_3 \xrightarrow{heat} (1-y-z)Al_2O_{4.5}H_3 + 2yAlO_{4/3} + 2zAlO_{5/3} + 1.5(y+z)H_2O \quad (2.2)$$

where $0 \leq (y,z) \leq 1$, and $AlO_{4/3}$ and $AlO_{5/3}$ represent tetrahedral and penta-coordinated aluminum respectively. A quantitative analysis was performed for the values of y and z in a manner similar to the analysis of the ^{29}Si NMR spectra. For example, I obtained (y,z) = (0,0) and (0.06, 0.14) for NT25 and NT400 respectively, reflecting the conversion of octahedral aluminum during heat treatment. On the other hand, the rehydroxylated sample NT400r gives (y,z) = (0.09, 0.06). However, it must be cautioned that the quantitative interpretation of ^{27}Al NMR spectrum for sample NT400 is less reliable than that for NT400r, since it has been suggested that reliable quantitative analysis of ^{27}Al NMR spectra should be derived from fully hydrated samples,[72,73] whereas NT400 is completely dehydrated. Specifically, differences in coordination environment and hydration level may affect the intensity of ^{27}Al signals due to its quadrupole moment, and thus may contribute to the better resolution of the NMR signals from penta-coordinated and tetrahedral aluminum in sample NT400r as compared to NT400.

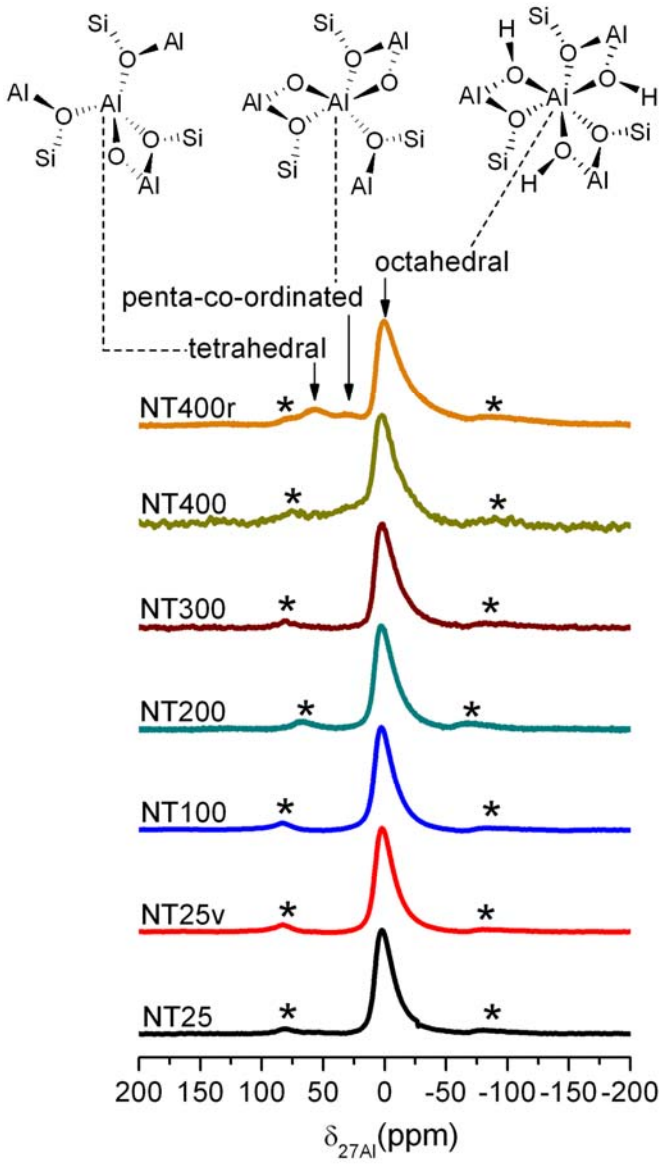

Figure 2.5. ^{27}Al NMR spectra of SWNT samples heat-treated at different temperatures. Asterisks denote the spinning side-band artifacts.

2-4 Nitrogen Physisorption

N_2 physisorption measurements for SWNT samples heat-treated at different temperatures were performed to investigate how dehydration, dehydroxylation, and structural transformation affects the SWNT pore volume (Figure 2.6). The original SWNT sample (NT25) did not show a significant pore volume, due to occupation of the pores by physisorbed water. The physisorption isotherms from the SWNT sample degassed at ambient conditions (NT25v) and heat-treated at 100°C (NT100) show characteristics of an IUPAC Type II isotherm,[74] which indicates non-porosity due to pore blocking by physisorbed water. In contrast, as the SWNT samples become more dehydrated (NT200 and NT300), the shape of the isotherm transforms to an IUPAC Type I,[74] distinctly suggesting activation of the porosity of the SWNT interior. The monotonic increase in the pore volume from NT25 to NT200 is due to SWNT dehydration, and from NT200 to NT 300 by dehydroxylation, in qualitative agreement with TGA-MS and FTIR studies discussed later in this report.

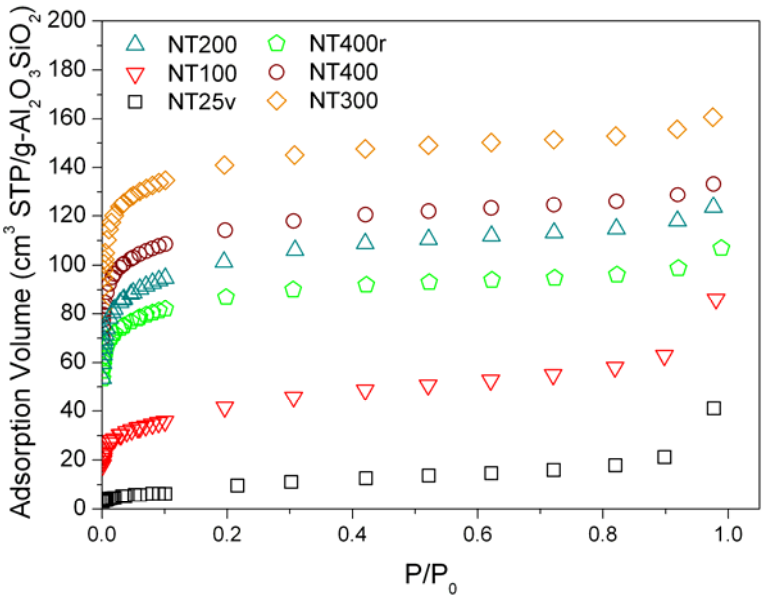

Figure 2.6. N_2 physisorption isotherms of SWNT samples at different conditions.

However, a pore volume decrease is observed as the heat treatment temperature goes from 300 ^{o}C to 400^{o}C. This phenomenon could be rationalized by partial pore blocking caused by the structural transformations accompanying dehydroxylation. Even though the wall structure of NT400 is likely to be partially "damaged" or disordered, the isotherm still shows a high microporosity. The further drop in pore volume for NT400r, in comparison to NT400, is presumably due to the decrease in pore volume due to the reconstitution of a substantial number of silanol groups, as well as the reoccupation of the SWNT pores with some amount of strongly physisorbed water. However, a study of SWNT structural deformation accompanied by pore collapse at high temperature (T >400^{o}C) is beyond the scope of the present paper. This aspect has been studied by Mackenzie *et al*.

2-5 FT-IR

The IR absorbance spectra of samples heat-treated and degassed at different temperatures are summarized in Figure 2.7a. The absorption at 1630 cm^{-1} is well known to represent the scissoring mode of physisorbed water. The rather broad absorption in the 2800-3800 cm^{-1} region is due to various stretching vibrations of O-H groups in the material: silanols at the inner surface, bridging Al-(OH)-Al groups at the outer surface, physisorbed water, and hydrogen bonding interactions between these species. Due to the intrinsically limited resolution of solid-state IR spectra, an assignment of the roles of these individual vibrational species is not possible. However, since all IR spectra were collected *in situ* on the same sample, a quantitative estimate of the amount of water and hydroxyl groups can be made on the basis of the integrated areas under the two respective absorbance peaks. Figure 2.7b shows the concentration of physisorbed water in the different samples, normalized by the water concentration in the SWNT sample at ambient conditions (NT25). This result confirms that the vast majority (~90%) of the physisorbed water is removed by vacuum heat treatment up to 150°C, and that the SWNT sample is

completely dehydrated by 250°C. The hydroxyl concentration in samples NT250-NT450, normalized by the hydroxyl concentration of the "baseline" dehydrated sample (NT250), is also shown in Figure 2.7b. It is suggested that around 30% of the hydroxyl groups (~2.7 -OH/nm^2) survive at 450°C.

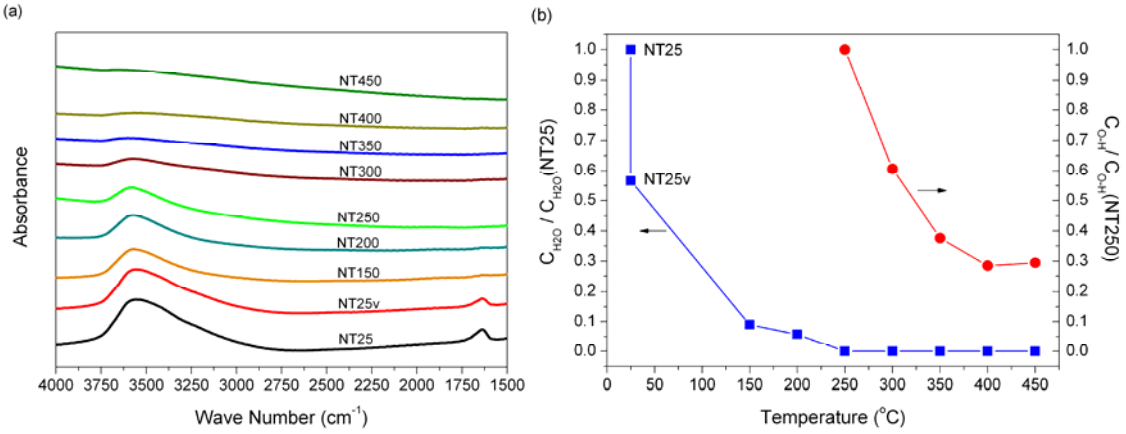

Figure 2.7. (a) FT-IR spectra of heat-treated SWNT samples. All spectra are plotted to scale and stacked in a vertical series. (b) Normalized physisorbed water concentration, and normalized hydroxyl group concentration, in the SWNT at different heat-treatment temperatures as calculated from FT-IR spectra.

2-6 XRD measurements and simulations

To complete the study of the SWNT structure during dehydration and to investigate the packing of the SWNTs in the solid sample, I performed *in situ* XRD measurements on SWNT samples heat-treated at various temperatures. The experimental results (Figures 2.8a and 2.8b) show a substantial intensity increase of the first peak at 3.9° 2θ upon dehydration from NT25 to NT250. On the other hand, the fourth peak at 13.3° 2θ remains constant in intensity. Beyond a heat treatment temperature of 250°C, there is a monotonic decrease in the intensity of the first peak due to the structural transformation and partial pore collapse, which are also suggested in the nitrogen physisorption isotherms.

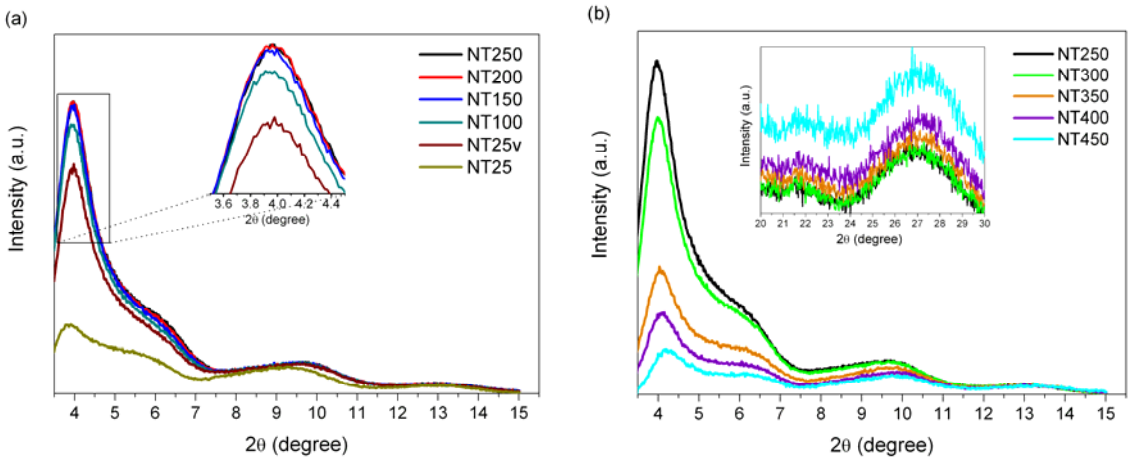

Figure 2.8. *In situ* XRD patterns of the SWNT sample: (a) from room temperature to 250°C, and (b) from 250-450°C. All patterns are plotted to scale.

A detailed XRD simulation study was performed in order to extract reliable structural information during nanotube dehydration. In a previous work, I qualitatively interpreted the XRD patterns of SWNT film samples in terms of Bragg diffraction from a crystalline bundle of nanotubes. Several later studies investigated the XRD patterns more quantitatively.[75-77] In particular, a more accurate model of the XRD patterns can be obtained by considering diffraction from small SWNT bundles (each composed of only a few nanotubes). However, a good agreement between experimental and simulated XRD patterns could not be achieved due to the effects of several parameters such as the number of SWNTs in a single bundle, the number of gibbsite structural units in the SWNT circumference, inter-nanotube distance, and the degree of hydration. I performed a systematic XRD simulation study on both dehydrated and hydrated SWNTs to achieve the best fit of the simulated XRD patterns.

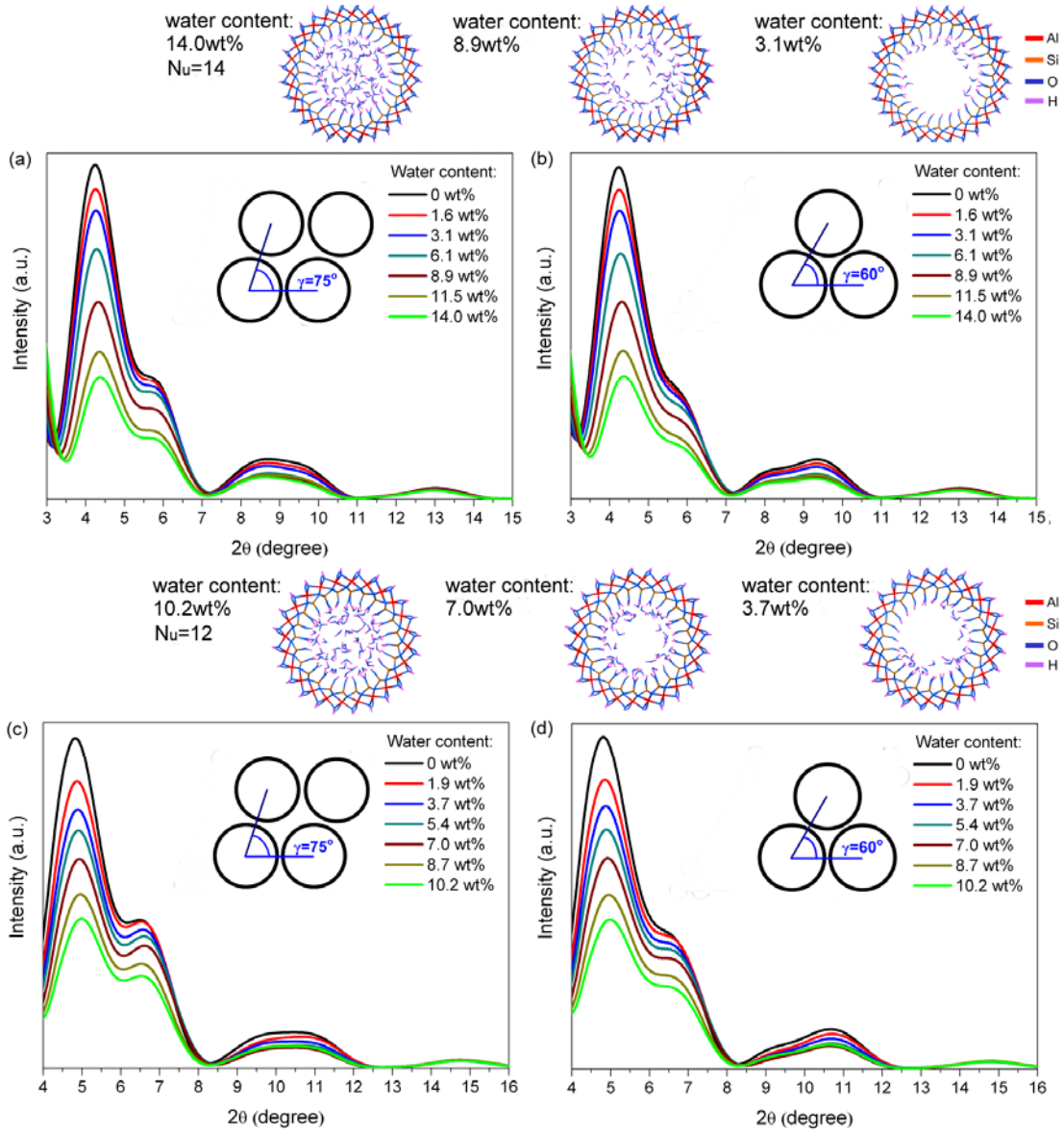

Figure 2.9. Simulated XRD patterns of the SWNT sample with different diameters, bundle structures, and water contents: (a) N_u=14, 2x2 bundling; (b) N_u=14, triangular bundling; (c) N_u=12, 2x2 bundling; and (d) N_u=12, triangular bundling. The SWNT-water models are obtained by grand canonical Monte Carlo (GCMC) simulations. Examples of SWNT-water models are also shown.

After extensive parameter variation studies, it was found that the best agreement with the experimental XRD patterns could be obtained by either a 2x2 bundle of SWNTs with a monoclinic packing angle of 75°, or a triangular arrangement of 3 SWNTs with a hexagonal packing angle of 60°. Although a hexagonal packing is intuitively assumed in many studies, a monoclinic packing angle of ~78° has also been proposed previously[42,78] based on circular dichroism and XRD measurements. Another important parameter is the number of replicating gibbsite units (N_u) in the SWNT circumference. Several recent computational studies employing quantum chemistry or classical forcefield techniques, suggest that the thermodynamically favored value of N_u = 12. However, the XRD simulations show that models with N_u = 14 agree somewhat better with experimental data. It is not possible to conclusively identify the exact value of N_u based upon the XRD patterns. Hence, in Figure 2.9 I depict simulation results for both values of N_u and for both the "best fit" packing models.

In all four cases, the intensity of the first peak strongly correlates with the amount of physisorbed water whereas the intensity of the fourth peak stays constant. Thus, the effect of hydration on the XRD patterns of the present SWNTs is analogous to the effect of C_{60} buckyballs in the pores of carbon nanotubes (i.e., "pea-pod" structures)[79-81] on the XRD patterns of carbon nanotube bundles. Therefore, I can quantitatively correlate the integrated intensity of the first peak (as obtained from the simulated XRD patterns) with the water content (Figure 2.10a). Strongly linear correlations are derived for all the four SWNT packing models. With these correlations, I can calculate the water content of the SWNTs from the experimental XRD data (Figure 2.10b). The results indicate that there is ~15 wt% water physisorbed in the SWNT in ambient conditions. This is in good agreement with the TGA results (shown in Figure 2.10b) as well as with Monte Carlo simulation results. However, the shape of the TGA curve cannot be directly compared to the XRD results owing to the different conditions of these experiments. The former is a

dynamic water loss measurement carried out under flowing helium, whereas the XRD patterns are from samples equilibrated under vacuum.

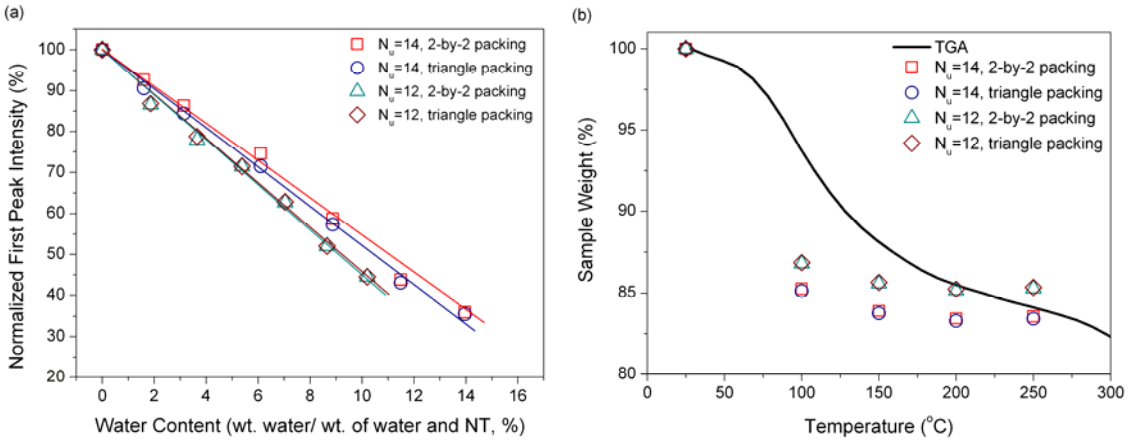

Figure 2.10. (a) Correlations of the first low-angle peak from simulated XRD patterns versus the weight fraction of water for four sets of simulation parameters. (b) SWNT sample weight loss calculated from experimental *in situ* XRD patterns and the correlation function derived in (a). The TGA trace is also included for comparison.

2-7 Summary

The phenomenology and mechanisms of dehydration and dehydroxylation in single-walled aluminosilicate nanotubes have been evaluated comprehensively in this chapter. A quantitative dehydration investigation *via* FT-IR, TGA and XRD, suggests that the SWNT sample contains *ca.* 15% physisorbed water under ambient conditions and becomes completely dehydrated at 250°C. Dehydroxylation, which (reversibly) transforms Q^3(6Al) silicons into Q^4(6Al) and (irreversibly) transforms octahedral aluminum into penta-coordinated and tetrahedral aluminum, takes place beyond 250°C as elucidated by NMR spectroscopy. A quantitative model for these processes was deduced from my investigation. A unique rehydroxylation phenomenon, which transforms condensed Q^3(6Al) silicons back into Q^4(6Al) silicons upon re-exposure to water vapor, has been found by ^{29}Si NMR and N_2 physisorption. Furthermore, N_2 physisorption and XRD show that dehydration and initial dehydroxylation lead to a high microporosity of

the nanotubes, whereas dehydroxylation at 400^{o}C or higher leads to partial pore collapse. The SWNT reaches its maximum pore volume (~1.4 times that of the anhydrous SWNT obtained at 250^{o}C) at 300^{o}C, at which temperature about 40% dehydroxylation has also occurred and an inner-surface silanol concentration of 5.5 -OH/nm^2 exists. Hence, I conclude that heat treatment under vacuum at 250-300^{o}C is an optimal pre-treatment condition, for full dehydration and yielding maximum pore volume while maintaining the nano-tubular structure, before surface modification of the SWNT under anhydrous conditions. Based on the present observations, the SWNTs can potentially be applied for molecular separation, adsorption, molecular encapsulation, and catalysis, after appropriate functional groups are introduced. Finally, I show that the XRD patterns of the SWNTs at various degrees of dehydration can be quantitatively modeled and matched to experimental data. This investigation yielded four likely models for SWNT packing and number of gibbsite units (N_u) among the many possibilities, as well as provided a quantitative correlation between the water content and X-ray scattering intensity from the SWNT.

CHAPTER 3

POST-SYNTHESIS INTERIOR FUNCTIONALIZATION OF SINGLE-WALLED ALUMINOSILICATE NANOTUBES

In this chapter, I describe a general strategy for the interior modification of aluminosilicate SWNTs, as illustrated by three reagents: acetyl chloride, methyltrimethoxysilane, and trichlorosilane. The modified SWNTs are carefully assessed by a combination of solid-state techniques including nitrogen physisorption, thermogravimetric analysis (TGA), powder X-ray diffracton (XRD), transmission electron microscopy (TEM), solid-state NMR, and water adsorption. Based on the results, I demonstrate that the organic functional groups are immobilized on the inner wall of the aluminosilicate SWNT by condensation with the inner-surface silanols. Furthermore, a detailed study of water adsorption yields an understanding of adsorption mechanisms in the bare and modified SWNT samples, and demonstrates the variation of SWNT surface hydrophilicity resulting from interior modification. The reported methodology for modifying SWNTs with various organic groups can be broadly applied to make the SWNTs functional for a range of applications involving selective interactions of the nanotube with molecules based on their shape, size, and chemical properties.

3-1 Experimental details

3-1-1 Post-synthesis interior functionalization of aluminosilicate SWNT

The synthesis and purification of the as-synthesized SWNT sample is reported in the previous chapter. For SWNT interior modification, 500 mg of as-synthesized SWNT powder was first placed in a flask connected to a 15 millitorr vacuum line and heat treated at 250^{o}C for 24 hours, after which it is considered fully dehydrated based upon the

study in Chapter 2. The heat-treated SWNT sample was then transferred to a nitrogen glove box and *ca.* 5mL of hexane solvent was added into the flask. The functionalizing reagent (acetyl chloride, trimethylmethoxysilane, or trichlorosilane) was then transferred into the flask, with the reagent to SWNT hydroxyl groupmolar ratio being ~ 2. The mixture was allowed to stir under nitrogen for 24 hours. The flask was then connected to the vacuum line and treated at 180^{o}C for 24 hours to remove the solvent and unreacted reagent. The resulting powder samples were used for characterization studies. The label "NT" denotes the bare SWNT, whereas "NT-A", "NT-M", and "NT-T" denote the SWNT treated by acetyl chloride, methyltrimethoxysilane, and trichlorosilane respectively.

3-1-2 Solid-state NMR

The SWNT sample was first packed into a 7 mm rotor. ^{13}C, ^{27}Al and ^{29}Si MAS NMR experiments were carried out on a Bruker DSX 300 spectrometer at frequencies of 75.5, 78.1 and 59.6MHz. For ^{13}C cross-polarization (CP) MAS NMR studies, the sample was spun at 5 kHz, and a single pulse of $\pi/2$ and repetition time of 4 s was used. The sample was spun at 5-6 kHz for ^{27}Al MAS NMR tests, for which a single pulse of $\pi/6$ and a repetition time of 0.1 s was used. For ^{29}Si MAS NMR, direct-polarization (DP) and cross-polarization (CP) tests were performed with repetition times of 10 s and 5 s respectively, at $\pi/2$ single pulse and 5 kHz spinning rate. The chemical shifts of ^{13}C, ^{27}Al, and ^{29}Si were referenced to adamantane, aluminum trichloride, and 3-(trimethylsilyl)-1-propanesulfonic acid sodium salt, respectively.

3-1-3 X-ray Diffraction (XRD)

Powder X-ray diffraction (XRD) was performed on a PAnalytical X'pert Pro diffractometer operating with a Cu Kα source. The high-resolution diffraction data were

collected with a diffracted-beam collimator and a proportional detector, scanning from 2 to 30^{o} two theta with a step size of 0.05^{o}.

3-1-4 Transmission Electron Microscopy (TEM)

Approximately 5 mg of SWNT samples were first dispersed in 10mL deionized water. The resulting dispersion was sonicated for 10 minutes. Around 5 drops of the sonicated SWNT dispersion were added on 300-mesh copper grids coated with Formvar layers. Transmission electron microscopy (TEM) images were recorded on a Hitachi HF2000 field emission gun TEM operated at 200 kV.

3-1-5 Thermogravimetric analysis (TGA)

The experiment was performed with a Netzsch STA409 instrument. Approximately 20 mg powder sample was heated under nitrogen diluted air from 25 to 900^{o}C with a ramp rate of 10^{o}C/min.

3-1-6 Nitrogen Physisorption

Nitrogen physisorption measurements were carried out on a Micromeritics Tristar at 77 K. The sample was placed in an analysis tube and degassed under 15 mTorr at 200^{o}C for 12 hours before the physisorption measurement.

3-1-7 Water adsorption

Water adsorption measurements were performed on IGAsorp (Hiden Analytical, Warrington, UK) at 25^{o}C. The sample was outgassed at 200^{o}C for 8 hours prior to recording the isotherm.

3-2 Porosity, structure, and organic loading

The nitrogen physisorption isotherms (Figure 3.1) of the as-made and the three modified SWNT samples all show the characteristics of IUPAC type I isotherms,

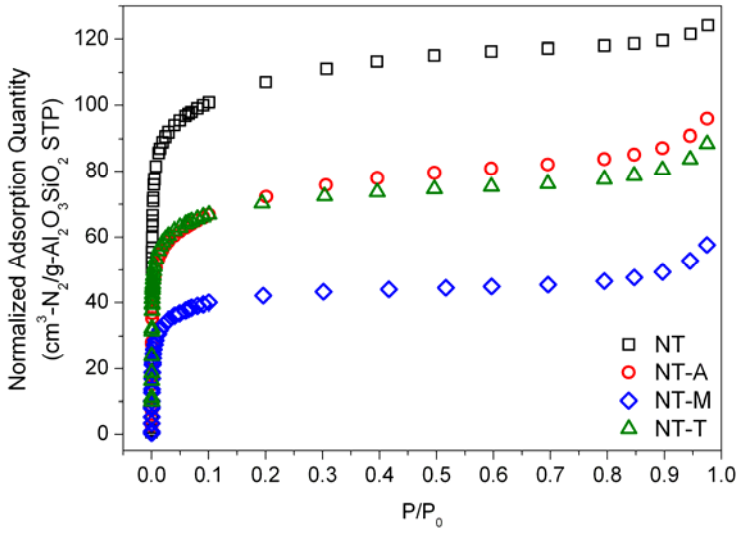

Figure 3-1. Nitrogen physisorption isotherms of as-synthesized and modified SWNTs, where NT denotes the bare SWNT, NT-A denotes SWNT treated by acetyl chloride, NT-M denotes SWNT treated by methyltrimethoxysilane, and NT-T denotes SWNT treated by trichlorosilane.

suggesting that the pore channels of the modified SWNT samples are microporous, as expected. More detailed information can then be extracted by employing the BET[82] model and t-plot method to these isotherm data. The BET model yields the total surface area (S_{BET}), contributed by both interior and outer surfaces of the SWNT. On the other hand, the t-plot[83] method is well-known for differentiating mesoporosity from microporosity present in the same sample.[84-86] Specifically, the linear fitting of the isotherms with H-J correlations[87,88] allows us to estimate the external surface area (S_{ext}) contributed by the outer surface of SWNT, and the micropore volume (V_{mp}) due to the pore volume in the SWNT channels. The values of S_{BET}, V_{mp}, and S_{ext} are summarized in Table 3.1. For the as-synthesized SWNT, S_{BET} is about 42 times larger than S_{ext}, suggesting there is significantly larger "accessible" surface area at the interior of SWNT in comparison to the outer surface.

Table 3.1. SWNT sample porosity derived from nitrogen physisorption data

sample	BET method	t-plot method	
	S_{BET} (m^2/g-$Al_2O_3SiO_2$)	V_{mp} (cm^3/g-$Al_2O_3SiO_2$)	S_{ext} (m^2/g-$Al_2O_3SiO_2$)
NT	418	0.17	10.1
NT-A	256	0.11	15.9
NT-M	153	0.06	11.3
NT-T	260	0.11	14.0

The relatively small accessible external surface area of SWNT is likely due to the packing of single SWNTs into bundles. After treatment with the three different reagents, all the samples show substantial decreases in both V_{mp} and the "internal" surface area S_{BET}-S_{ext}, thereby providing direct evidence that most of the surface modification reaction takes place at the interior of the SWNTs and that the introduced organic entities are immobilized in the SWNT channels. However, the amount of decrease in S_{BET}-S_{ext} and V_{mp} for the three modified SWNT samples is strongly related to the molecular size of the reagent and the fractional silanol substitution at the SWNT's inner surface (which can also be considered the loading of the reagent). A quantitative analysis of the fractional silanol substitution is discussed later in this report.

A deviation of S_{ext} from bare to modified SWNTs is also observed, due to the variation in SWNT bundling characteristics between samples. In particular, the S_{ext} for as-synthesized SWNT from five batches shows an average of 12.2 with a standard deviation of 4.5 m^2/g-$Al_2O_3SiO_2$. On the other hand, V_{mp} and S_{BET} of the as-made SWNT from five batches show averages of 0.168 cm^3/g-$Al_2O_3SiO_2$ and 417 m^2/g-$Al_2O_3SiO_2$ with relatively small standard deviations of 0.008 cm^3/g-$Al_2O_3SiO_2$ and 18 m^2/g-$Al_2O_3SiO_2$, respectively. Hence, the differences of S_{ext} between bare and modified SWNTs listed in Table 3-1 are within the statistical variation, whereas the deviations of V_{mp} and S_{BET}-S_{ext} from bare to modified SWNTs are statistically meaningful. As a

consequence, the analysis from nitrogen physisorption measurements reveals that the modified SWNT samples possess significantly lower pore volumes and total surface areas (dominated by the inner surface area of nanotubular channels) than the bare SWNTs, whereas no statistically significant deviation in the external surface areas is observed, hence clearly suggesting that the surface modification takes place in the interior of the SWNT.

While nitrogen physisorption analysis elucidates the porosity and surface area of the as-made and modified SWNTs, X-ray diffraction (Figure 3.2) gives information on the morphology and bundling of the SWNTs. XRD patterns of nanotubar materials has been theoretically and experimentally studied in detail in Chapter 2.

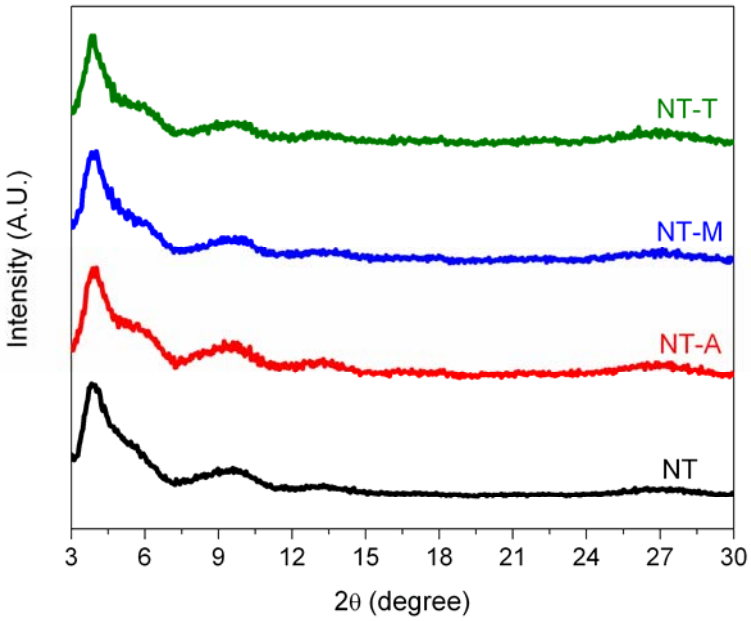

Figure 3.2. XRD patterns of as-synthesized and modified SWNTs.

It is clear that the diffraction patterns of nanotubes forming small bundles are not dominated by Bragg diffraction but by X-ray scattering, as opposed to ordered porous materials with one-dimensional channels such as one-dimensional zeolites, MCM-41, or

SBA-15. Previous XRD studies on single-walled carbon nanotubes have elucidated the diffraction pattern for sample of isolated nanotubes.[79,89,90] The bundling of nanotubes leads to additional characteristic "shoulder-like" peaks. Comparison of experimental and simulated XRD patterns have provided definitive answers regarding the bundling of carbon SWNTs. Similarly, the XRD simulation study in Chapter 2 on the present aluminosilicate SWNTs showed that the patterns shown in Figure 3.2 unequivocally represent the structure of SWNTs organized in bundles. The as-synthesized SWNT sample shows high purity, as reflected in the sharply-defined SWNT characteristic peaks (between 3-19^{o}). Similarly, the three modified-SWNT samples show well-defined XRD patterns nearly identical to that of the bare SWNT, with no evidence of structure amorphization or alteration. The nanotubular structure and the SWNT bundling characteristics therefore remain unchanged after the surface modification.

While XRD reveals the nanotubar structure and high bulk purity of the bare and modified SWNTs, TEM images provide localized visual information on the samples and confirms the XRD results. The TEM image from the as-synthesized SWNT sample clearly shows bundles of aligned nanotubes with a *ca.* 2 nm line-to-line distance representing the outer diameter of SWNT. After treatment with the organic reagents, the channels of the modified SWNT samples remain intact for NT-A and NT-M samples. Although the SWNTs form dense bundles on the TEM grid after evaporation of the solvent, one can also occasionally observe isolated nanotubes (NT-T sample).

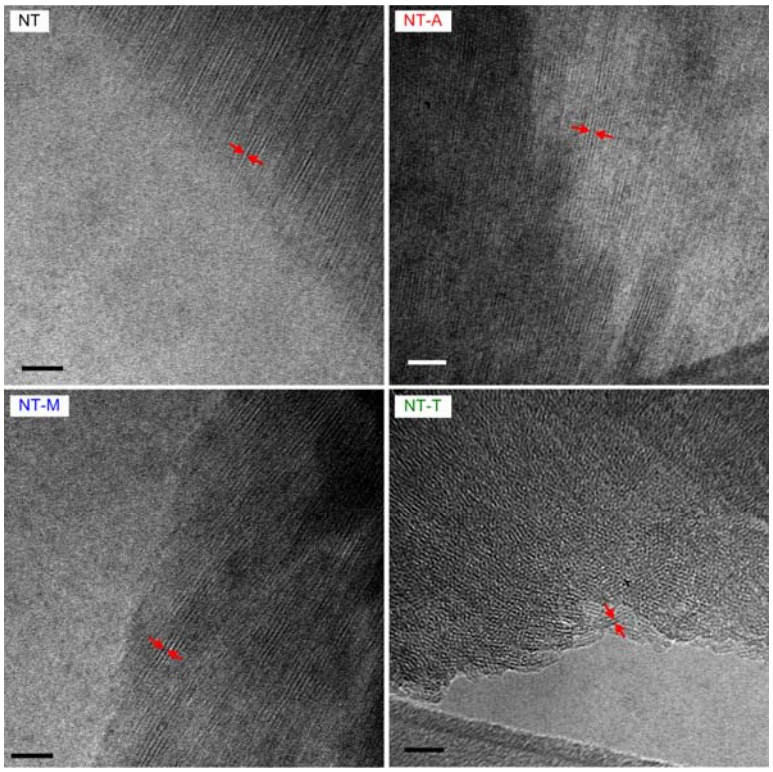

Figure 3.3. TEM images of as-synthesized and modified SWNT bundles. The scale bars (in black or white) represent 20 nm. The pairs of red arrows represent individual SWNTs, with approximately 2 nm diameter.

Thermogravimetric analysis was employed to investigate the mass losses associated with heating the SWNTs in diluted air, including losses associated with physisorbed water, surface hydroxyl groups, and grafted organic groups. The first-derivative TGA curves are summarized in Figure 3.4. For the bare SWNT, two pronounced peaks, one ranging from 25-250^{o}C and the other from 250-450^{o}C, are observed. They are assigned to the loss of physisorbed water and hydroxyl groups respectively, following the observation in Chapter 2. An additional peak in the 450-600^{o}C region is observed in all three modified SWNTs, and is assigned to the loss of the introduced organic entities. Furthermore, considering the low boiling points of the reagents used

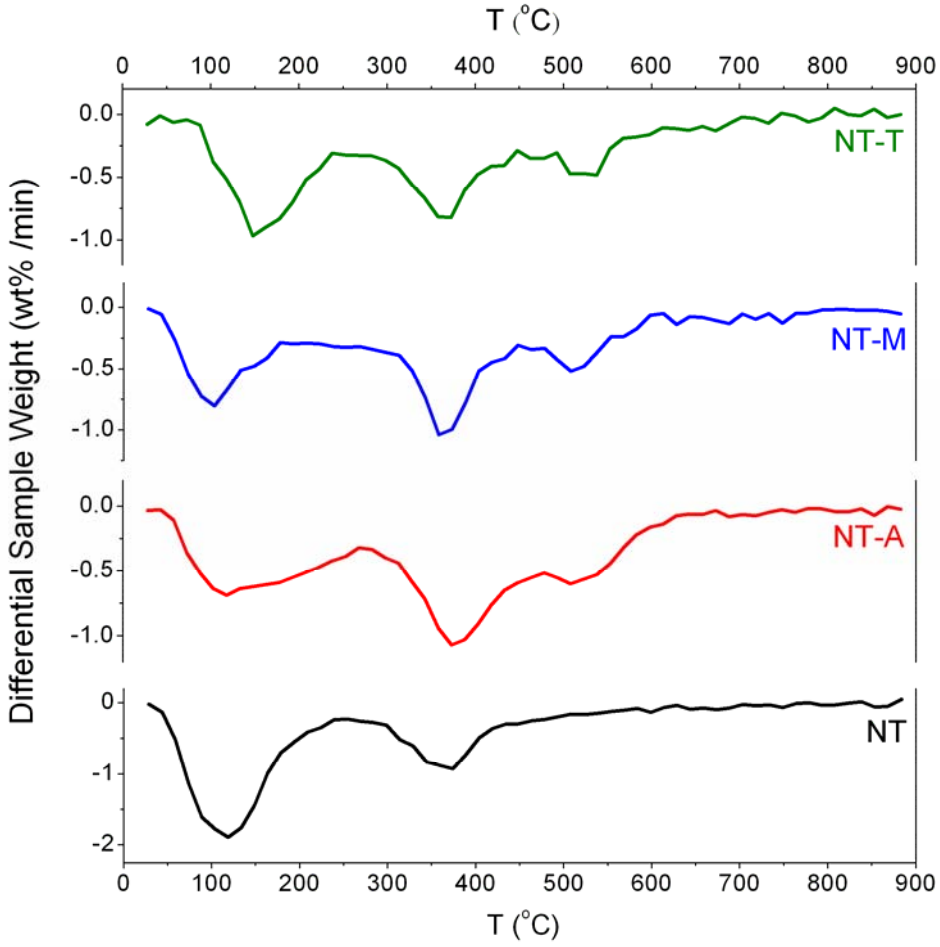

Figure 3.4. Differential TGA curves of as-synthesized and modified SWNTs.

(52°C for acetyl chloride, 102°C for methyltrimethoxysilane, and 32°C for trichlorosilane), the relatively high temperature (450-600°C) at which the organic groups are lost implies that they are be covalently bonded to the surface, and not physisorbed on the inner surfaces of the SWNTs.

The mass loadings of physisorbed water, hydroxyl groups, and organic groups in the bare and modified SWNTs, all normalized by the mass of dry aluminosilicate ($Al_2O_3SiO_2$) at the end of TGA measurement (900°C), are summarized in Table 3.2. For the three modified SWNT samples, decreases of the physisorbed water loading in comparison to the as-made SWNT suggest that all the surface modifications yield a lower hydrophilicity in the SWNT. A more detailed hydrophilicity analysis, based on water adsorption measurements, is presented below. Apart from the decrease of physisorbed water loading, a decrease of the hydroxyl group loading accompanying the organic group loading is also observed in the three modified samples. This clearly shows that the surface silanols in SWNT are partially substituted by the surface modification reagents.

Table 3.2. Normalized weight of water/hydroxyl groups/organic groups in as-synthesised and modified SWNT samples determined by TGA

	normalized mass		
sample	physisorbed water (g-H_2O/g-$Al_2O_3SiO_2$ %)	hydroxyl group (g-OH/g-$Al_2O_3SiO_2$)	organic group (g-organic/g- $Al_2O_3SiO_2$ %)
NT	30.9	21.3	--
NT-A	15.3	19.4	12.6
NT-M	12.5	14.5	9.2
NT-T	13.3	13.6	8.2

3-3 Surface reaction schemes

Based upon the results reported above, it is likely that the reagents (acetyl chloride, methyltrimethoxysilane, and trichlorosilane) react with surface silanols in the SWNT interior and are therefore immobilized on the surface. Therefore, I propose reaction schemes for the treatment of the SWNT with different reagents (Scheme 3.1) in analogy to the reported surface modifications of silicate materials by acid halides,[91] methoxysilanes,[47,92] and chlorosilanes,[93-96] respectively. The surface products associated with the proposed reaction schemes are then assessed by ^{29}Si and ^{13}C solid-state NMR.

Scheme 3.1: Reactions at SWNT interior by various reagents: acetyl chloride, methyltrimethoxysilane, and trichlorosilane, denoted by NT-AcCl, NT-MTMS, and NT-TClS respectively.

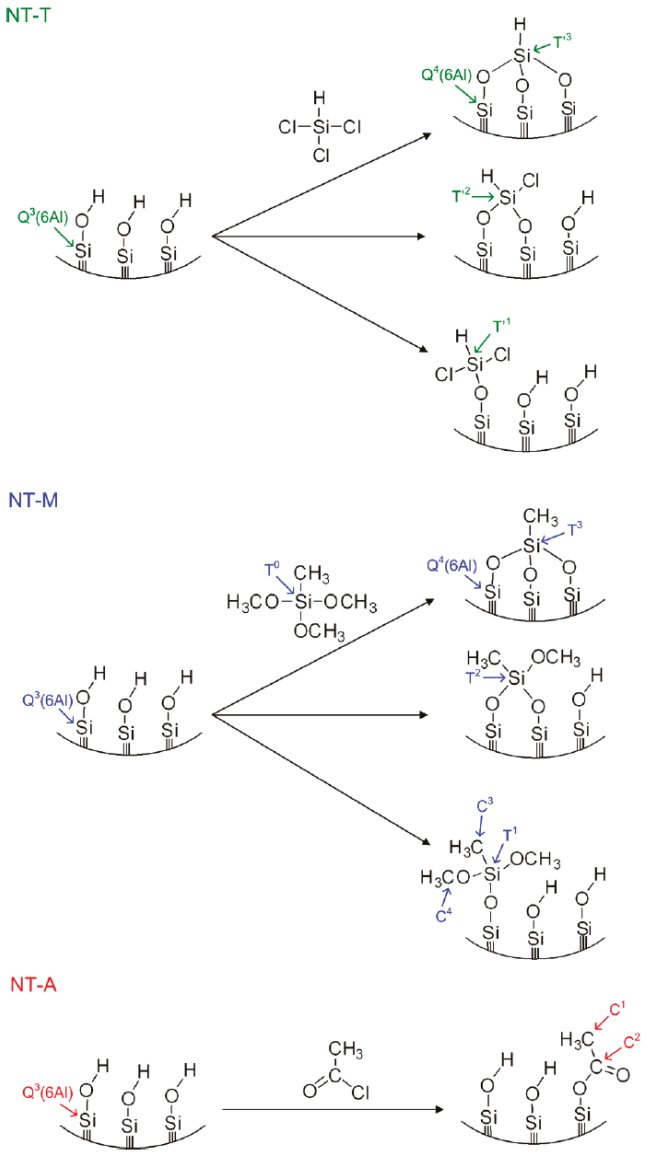

The ^{29}Si CP-MAS NMR spectra (Figure 3.5a and 3.5b) provide the molecular-level characterization of the silicon environment in the bare and modified SWNTs. For as-synthesized SWNTs, the most pronounced peak is at -79 ppm and is assigned to the unique Q^3(6Al) silicon framework[59,97] which is not commonly found in other aluminosilicate frameworks. The small and relatively broad peak at -90 ppm is assigned to Q^4(6Al) and considered the contribution from defect sites involving a small number of condensed silanols present in as-made SWNT samples. The ^{29}Si CP-MAS spectrum from the as-prepared SWNT sample implies the high purity of the sample. For modified SWNT samples, slight increases of the Q^4(6Al)/Q^3(6Al) ratio is likely due to the heat-treatment at 250^{o}C prior to the modification reaction as well as the immobilization of introduced silanes on the SWNT inner silicate surface, specifically for NT-M and NT-T. Moreover, the grafted acetyl group is likely to have negligible effect on Q^4(6Al)/Q^3(6Al) ratio since the study in Chapter 2 suggests that the silicon chemical shifts of the Si-O-C and Si-O-H environments are not significantly different.

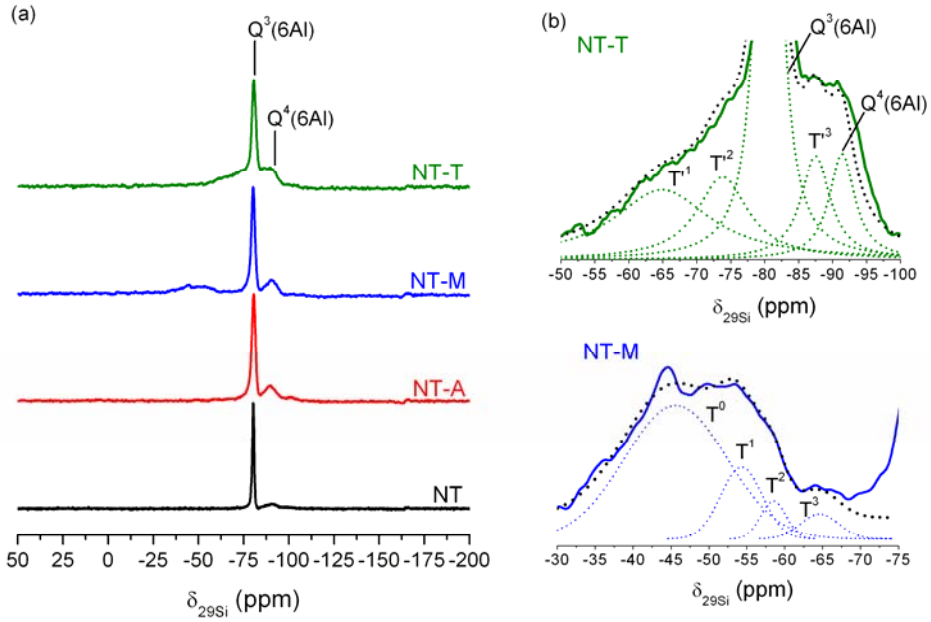

Figure 3.5. (a) ^{29}Si CP/MAS NMR spectra of SWNT samples. (b) A detailed view of ^{29}Si CP/MAS NMR spectra for NT-M and NT-T.

For NT-M, there are several additional peaks besides the Q^3(6Al) and Q^4(6Al) in the spectrum shown in Figure 3-5b.These peaks are assigned to T^0 (-45 ppm), T^1 (-53 ppm), T^2 (-59 ppm), and T^3 (-63 ppm) respectively, and these assignments are in good agreement with previous reports. Furthermore, the agreement of the chemical shifts of the T^1, T^2, and T^3 species with those reported for silane modifications on porous silicas also suggests that the reaction takes place on the SWNT inner surface (composed of Q^3 silicon). In contrast, a reaction on the SWNT outer surface (composed of octahedrally coordinated aluminum) would significantly alter the silicon chemical shifts of T^1, T^2, and T^3 species due to the formation of Si-O-Al linkages.[65,98,99] On the other hand, I also assigned the peaks in the ^{29}Si CP/MAS spectrum (Figure 3.5b) for T' groups present in the NT-T sample: T'^3 at -87ppm, T'^2 at -73.8 ppm, and T'^1 at -64.9ppm based up on the previous report from J.C. Clark and C.E. Barnes wherein they have suggested T'^3 are in the range of -70 to -85ppm, T'^2 of -50 to -68ppm, and T'^1 of -30 to -40ppm.[100] However, regarding the disagreements in peak assignments, I performed a control experiment by modifying a well-known mesoporous silicate material, SBA-15, with trichlorosilane. The ^{29}Si CP-MAS NMR for this controlled sample (SBA-15 treated by trichlorosilane) yields good consistency in chemical shifts of T' groups with T' groups from NT-T sample. Furthermore, it should be cautioned that the relative peak areas in the CP-MAS spectra do not provide reliable quantitative information on the molar ratio of different T groups. A quantitative analysis can be performed using ^{29}Si direct polarization (DP) spectra and is discussed below.

While ^{29}Si CP/MAS NMR probes the silicon coordination, ^{13}C CP-MAS NMR (Figure 3.6) is an excellent probe of the immobilized organic entities. For the NT-A sample, there are two peaks clearly assigned to C^1 (the methyl group at 22.9 ppm) and C^2 (the carbonyl group at 180.8 ppm), thereby strongly supporting the proposed scheme for acetyl chloride immobilized on the SWNT inner surface. On the other hand, the two

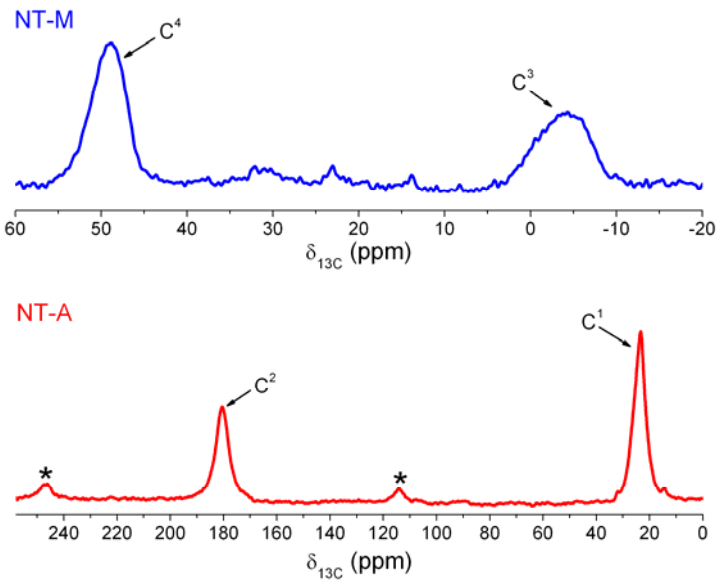

Figure 3.6 ^{13}C CP/MAS NMR spectra of NT-A and NT-M.

peaks observed in the spectrum of NT-M are assigned to the C^3 (the methyl group at -4.5 ppm) and C^4 (the methoxy group at 48.8ppm), in good agreement with the proposed scheme for modification by methyltrimethoxysilane. ^{27}Al NMR (Figure 3.7) spectroscopy was then used to investigate the possible alteration of the SWNT outer surface during surface modification. The peak at 4 ppm for as-made SWNT is assigned to octahedral aluminum.[101,102] The ^{27}Al spectra remain unchanged, and no additional peaks are observed in the three modified samples. This implies that the nanotube wall remains intact during surface modification, since previous studies suggest that any partial degradation of the outer wall of nanotube is accompanied by the appearance of tetrahedral or penta-coordinated aluminum. No significant shift of the octahedral aluminum peak is seen, suggesting that the silane reagents do not modify the SWNT outer surface.

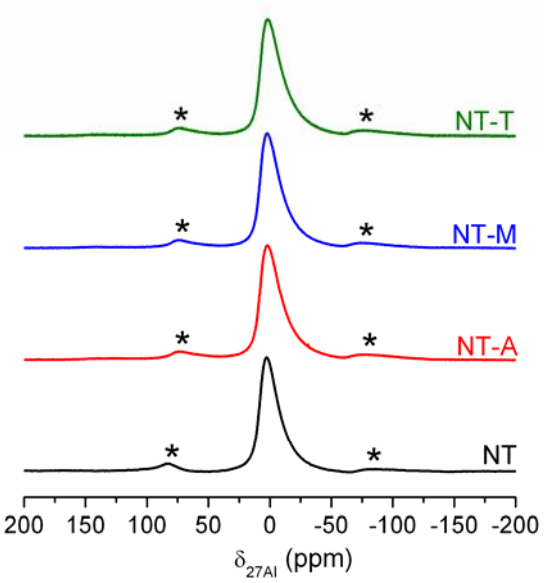

Figure 3.7 ^{27}Al NMR spectra of as-synthesized and modified SWNT samples.

3-4 Water adsorption

The water adsorption isotherms measured at 25°C are summarized in Figure 3.8, with the adsorption quantity normalized by the amount of dry aluminosilicate ($Al_2O_3SiO_2$) as obtained from the TGA results (Table 3.2). After surface modification by the three reagents, the water uptake capacity of the SWNTs decreases substantially to about 60-75% of the bare SWNT capacity, suggesting that the modified samples become more hydrophobic. However, a decrease of water capacity in the modified SWNT can be also be rationalized by a lower pore volume (verified by nitrogen physisorption) as well as the variation of surface hydrophilicity after modifications. A mechanistic model is necessary in order to gain physical insight on the water adsorption isotherms in SWNTs.

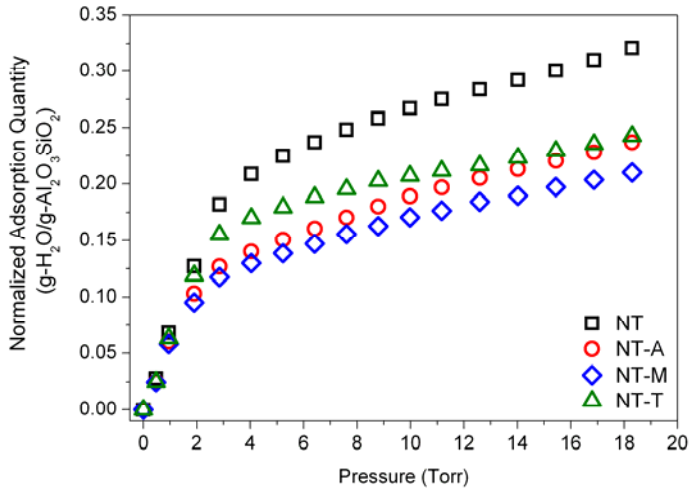

Figure 3.8 Water adsorption isotherms at 25°C of as-synthesized and modified SWNT samples.

Based upon Grand Canonical Monte Carlo (GCMC) simulation results (Figure 3.9a) of water adsorption in bare SWNT (carried out in a manner identical to the study in Chapter 2), it is clear that the water molecules can form multiple layers inside the SWNT, beginning from a monolayer at low chemical potential. Based on the work in Chapter 2, it is clear that the first layer of water molecules is primarily formed by hydrogen bonding

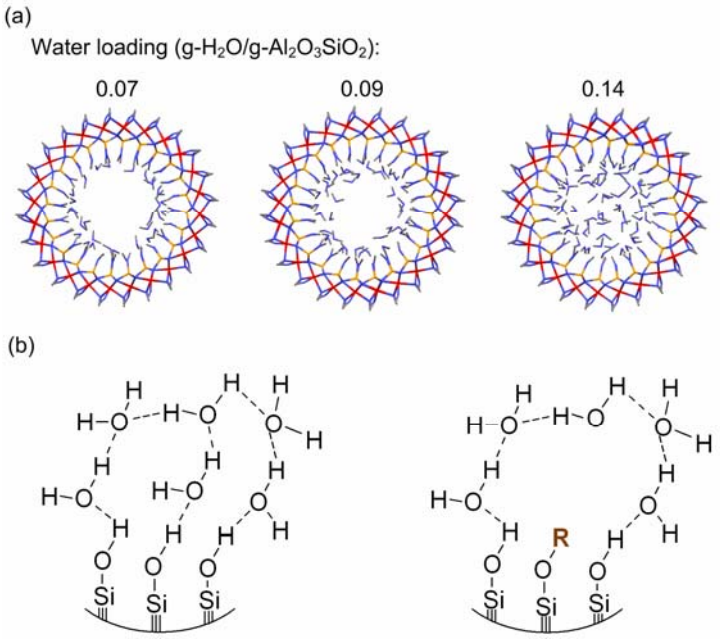

Figure 3.9 (a) Simulated bare SWNT-water models with different water loading obtained by grand canonical Monte Carlo (GCMC) simulations. (b) Proposed water adsorption mechanisms in the channels of bare and modified SWNTs.

between water molecules and surface silanol groups, whereas the subsequently adsorbed water layers form by hydrogen bonding between water molecules. Therefore, I propose a model for water adsorption in modified SWNTs as illustrated in Figure 3.9b. The proposed mechanism includes two phenomena: (1) in the formation of the first adsorbed water layer, with the water molecules only hydrogen-bonding on the sites at which the surface silanols have not been substituted by organic groups; and (2) a subsequent water layer forms adjacent to the first water layer by hydrogen bonding between two adjacent water molecules. The BET model,[82] which captures multi-layer adsorption phenomena, can be used to model the water adsorption mechanism in the SWNT:

$$\frac{P/P_0}{n\left(1-P/P_0\right)}=\frac{\left(C-1\right)}{n_m C}\left(P/P_0\right)+\frac{1}{n_m C} \qquad (3.1)$$

where P is the pressure of water vapor, P_0 is the saturated water vapor pressure at a given temperature, n is the adsorption quantity (g-water/g-$Al_2O_3SiO_2$), n_m is the monolayer coverage (g-water/g-$Al_2O_3SiO_2$), and C is the ratio of the equilibrium constants for the monolayer and subsequent multilayer adsorption. Usually, the constant C is of several orders of magnitude larger than unity for N_2 adsorption at 77K as well as in the water adsorption fitting results. Hence equation (3.1) can be simplified to:

$$\frac{P/P_0}{n\left(1-P/P_0\right)} = \frac{1}{n_m}\left(P/P_0\right) + \frac{1}{n_m C} \qquad (3.2)$$

Based on Equation 3-2, a plot of $\frac{P/P_0}{n\left(1-P/P_0\right)}$ vs. $\left(P/P_0\right)$ is the well-known BET plot for multilayer adsorption phenomena and is applicable in the moderate relative pressure region. The applicable pressure region for the BET plot is well-defined for nitrogen physisorption at 77K ($0.05< P/P_0 <0.35$ for mesoporous materials[74,82] and $P/P_0 <0.05$ for microporous materials).[103] However, several few reports have suggested that the BET plot for water adsorption can be applied in the relative pressure range of $0.05< P/P_0 <0.5$.[104-106] I chose data in the range $0.1< P/P_0 <0.35$, wherein the four BET plots show high linearity, to fit Equation 3.2 (Figure 3.10). The fitted linear correlations all have positive intercepts, implying that it is feasible to apply the BET model in the assumed pressure region.[103] The fitted slope of the BET equation gives the monolayer water coverage n_m, and these values are summarized in Table 3.3.

Table 3.3 Monolayer coverage fitted from water adsorption BET plots

sample	n_m ($g\text{-}H_2O/g\text{-}Al_2O_3SiO_2$)
NT	0.174
NT-A	0.118
NT-M	0.107
NT-T	0.131

A decrease of n_m between bare and modified SWNTs clearly suggests that a certain fraction of silanols in the SWNT interior are substituted during surface modification and are hence unavailable for monolayer adsorption of water. Furthermore, the introduced reagents create hydrophobic regions in the SWNT. These two factors are responsible for a lower water uptake capacity of the modified SWNTs in both the intermediate and high pressure regions. In contrast, the low pressure region shows negligible differences, since the Henry's constant for initial water adsorption on available silanol sites remains essentially unaffected.

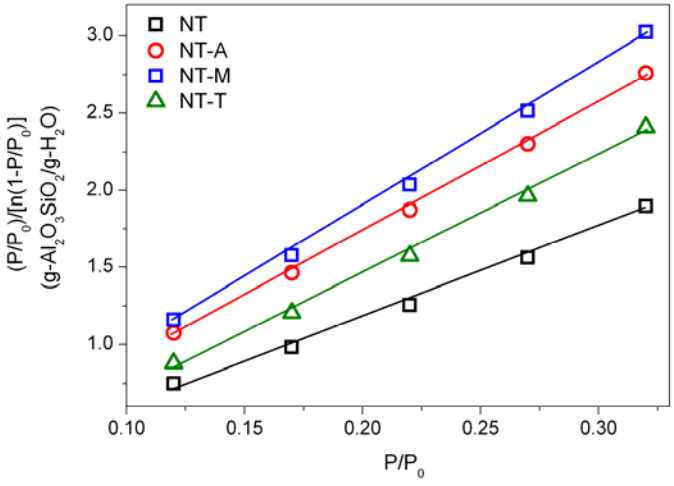

Figure 3.10 BET plots derived from water adsorption isotherms for as-synthesized and modified SWNT samples.

3-5 Fractional silanol substitution

In this section, I estimate the fractional surface silanol substitution after interior modifications by three introduced reagents, from the results of the different characterization techniques including nitrogen physisorption, TGA, ^{29}Si NMR, and water adsorption,. The fractional silanol substitution is physically equivalent to the surface coverage of the introduced organic entities on the inner wall of the SWNT. The results are summarized in Table 3.4 and the methodology is described as follows. The estimate of fractional silanol substitution from the nitrogen physisorption data is based upon the assumption that the lower micropore volume of modified SWNTs is due to the introduced organic entities in SWNT channels. Two approaches are then possible to interpret the micropore volume decreases in terms of the surface coverage of organic groups. The first approach assumes that the molar density of the organic groups embedded inside the SWNT channels is unchanged from its value in a pure liquid phase at 25^{o}C. The mass of the organic groups in the SWNT can then be calculated. This quantity can finally be converted into the molar loading (mol organic group/g-$Al_2O_3SiO_2$) using an average molecular weight for the different immobilized types of groups. In the second approach, one can estimate the sizes of the organic groups grafted in the modified SWNTs and directly interpret the pore volume decrease for modified SWNTs in terms of the surface coverage. The surface coverage can also be derived from TGA data. I can utilize the organic loading from TGA data (Table 3.2) to approximate the SWNT inner surface coverage. This approach converts the gravimetric data into a molar loading by using an average molecular weight derived from the NMR results (similar to the approach used for the nitrogen physisorption data in the case of NT-M and NT-T). Finally, the decrease of monolayer water coverage (summarized in Table 3.4) in modified SWNTs can be considered equivalent to the decrease of interior surface silanol loading due to the modifications, and hence allows calculation of the organic loading. Table 4 shows the results of the estimates from the four different methods. It is clear that 25-35% of the

interior silanols have been substituted for NT-A, 24-38% for NT-M, and 25-30% for NT-T.

Table 3.4 Fractional silanol substitution in bare and modified SWNTs

sample	fractional silanol substitution (# of silanols being substituted in modified SWNT/ # of silanols in bare SWNT)			
	TGA	N_2 physisorption (liquid density)	N_2 physisorption (molecular size)	Water adsorption
NT-A	0.35	0.25	0.34	0.32
NT-M	0.33	0.24	0.37	0.38
NT-T	0.26	0.28	0.30	0.25

3-6 Summary

I have developed a general method for functionalizing the inner surface of single-walled aluminosilicate nanotube materials with organic reagents (as illustrated in Figure 3.11), and presented the first unambiguous and comprehensive characterization to reveal the occurrence, extent, and structural details of the inner-surface functionalization in such modified SWNTs. Furthermore, a comprehensive investigation of the resulting solids using nitrogen physisorption, powder X-ray diffraction (XRD), transmission electron microscopy (TEM), thermogravimetric analysis (TGA), ^{29}Si and ^{13}C solid-state NMR and water adsorption provides a detailed understanding of the porosity, structure, and surface chemistry of the functionalized nanotubes. In particular, SWNTs modified with the three reagents preserve their nanotube structure, and the variation in size and type of reagents allows for the control of the pore volume of the SWNT. I have also demonstrated that different types of organic groups, including alkyl, alkoxy, or carbonyl groups, can be immobilized at the SWNT inner surface. Water adsorption in the SWNTs is interpreted by the BET model to elucidate the adsorption mechanism in both bare and modified SWNTs. As an example of the potential applications, I show that the functionalization approach enables us to control the surface hydrophilicity as well as the water uptake of the SWNT. Finally, estimates of fractional surface silanol substitution for the three

modified SWNTs are achieved via different characterization techniques, and consistent results are obtained.

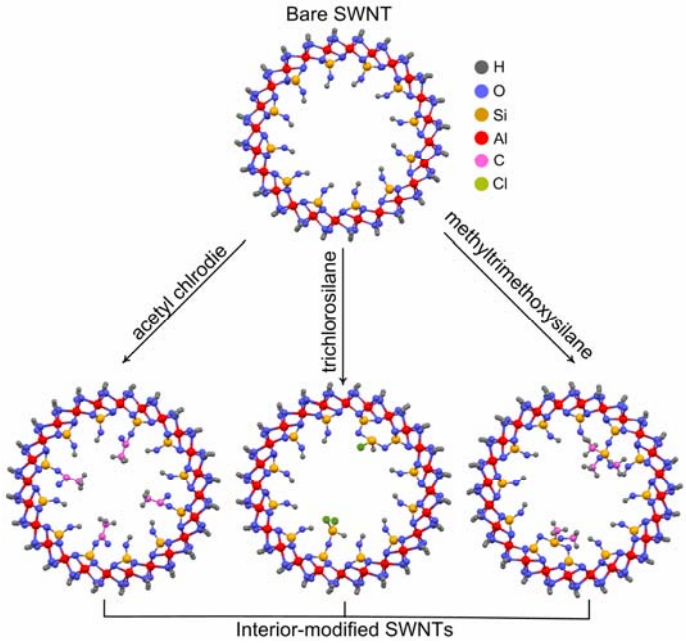

Figure 3.11 Illustration of SWNT modified by various reagents.

CHAPTER 4

DIRECT INTERIOR FUNCTIONALIZATION OF SINGLE-WALLED ALUMINOSILICATE NANOTUBES

In this chapter, I describe the formation, characterization, and application of interior-amine-functionalized aluminosilicate SWNTs, referred to as ANTs, prepared through a direct synthesis route. The direct route is desired since it circumvents several problems associated with the post-synthesis route, e.g. drying of the nanotube dispersion to produce a nanotube powder, and complete redispersion of the powder in solvents after the post-synthesis treatment. The structure, morphology, framework, and surface chemistry of these new direct-functionalized nanotubes are investigated by a range of solid-state characterization techniques, including transmission electron microscopy (TEM), X-ray diffraction (XRD), nitrogen physisorption, elemental analysis, vibrational spectroscopy, and solid-state NMR. The functionality of the nanoconfined immobilized primary amine groups at the interior of SWNTs is carefully assessed by CO_2 temperature programmed desorption (CO_2 TPD), and CO_2 adsorption. This study is the first demonstration of creating interior functionality of single-walled nanotube materials through a one-step synthesis. The reported functional SWNT synthesis methodology could open a new class of functional nanotube design and applications.

4-1 Experimental details

4-1-1 Preparation of Aluminosilicate and Amino-aluminosilicate nanotubes (NT and ANT)

Tetraethyl orthosilicate (TEOS) and aminomethyltriethoxysilane (AMTES) was mixed with aluminum-tri-*sec*-butoxide in a glove box filled with nitrogen. The mixture,

with a molar ratio TEOS:AMTES:Al:$HClO_4$=(1-x):x:2:1, was added into a Teflon jar with an aqueous 38 mM perchloric acid solution. Bare aluminosilicate nanotubes, referred to as NT in this chapter, were obtained when x=0. Amino-aluminosilicate nanotubes, referred to as ANT, were synthesized when x=0.2. The aqueous mixture was under vigorous stirring at room temperature in ambient conditions for 24 hrs. The solution was then diluted with DI water by a factor of 3.8 and was stirred at 95^{o}C for 4 days. Once the temperature was brought to 95^{o}C, the solution turned from cloudy to clear in about one hour. After the solution was cooled to room temperature, a 30 wt% ammonia solution was added dropwise until gelation of the suspended nanotubes occurred. The gel was isolated by centrifugation at 7000 rpm for 10 min. The supernatant was discarded and a few drops of 10 N hydrochloric acid were added to the gel, thereby re-dispersing the nanotubes. The resulting gel was purified by dialysis against DI water for 3 days using a membrane with a molecular weight cutoff of 15 kDa. The purified gel was dried at 60 ^{o}C and then ground to obtain a powder sample of NT or ANT. Approximately one gram of NT/ANT powder sample is obtained by a one liter synthesis batch.

4-1-2 Transmission Electron Microscopy (TEM)

Approximately 5 mg of SWNT samples were first dispersed in deionized water. The resulting dispersion was sonicated for 10 minutes. Around 5 drops of the sonicated SWNT dispersion were added on 300-mesh copper grids coated with Formvar layers. Transmission electron microscopy (TEM) images were recorded on a Hitachi HF2000 field emission gun TEM operated at 200 kV.

4-1-3 X-ray diffraction (XRD) Measurements and Simulations

XRD scans in Bragg-Brentano geometry were performed on a PAnalytical X'pert Pro MPD diffractometer operating with a Cu Kα source. Diffraction data were collected with a collimator and Miniprop detector, in the range of 3-30^{o} 2θ and a step size of 0.05^{o}.

Grazing-angle XRD scans were performed on PAnalytical X'pert Pro MRD diffractometer operating with a Cu Kα source. The Reflex module of the Materials Studio 3.2 molecular simulation package (Accelrys, Inc.) was used, and the details of such simulations have been reported in the works in Chapter 2.

4-1-4 Nitrogen Physisorption

Nitrogen physisorption measurements were carried out on a Micromeritics Tristar II at 77 K. The sample was placed in an analysis tube and degassed under 15 mTorr at 200 ^{o}C for 12 h before the physisorption measurement.

4-1-5 Solid-State NMR

The NT or ANT sample was first packed into a 7 mm rotor. ^{13}C, ^{27}Al, and ^{29}Si MAS NMR experiments were carried out on a Bruker DSX 300 spectrometer at frequencies of 75.5, 78.1, and 59.6 MHz respectively. For ^{13}C cross-polarization (CP) MAS NMRstudies, the sample was spun at 5 kHz, and a single pulse of $\pi/2$ and repetition time of 4 s was used. The sample was spun at 5-6 kHz for ^{27}Al MAS NMR tests, for which a single pulse of $\pi/6$ and a repetition time of 0.1 s was used. For ^{29}Si MAS NMR, direct polarization (DP) tests were performed with repetition times of 10 s at $\pi/2$ single pulse and 5 kHz spinning rate. The chemical shifts of ^{13}C, ^{27}Al, and ^{29}Si were referenced to adamantane, aluminum trichloride, and 3-(trimethylsilyl)-1-propanesulfonic acid sodium salt, respectively.

4-1-6 FT-Raman Spectroscopy

FT-Raman spectra were obtained on a Bruker Vertex 80v spectrometer equipped with dual FT-IR and FT-Raman benches and a CaF_2 beamsplitter.

4-1-7 CO_2 temperature programmed desorption (TPD)

The CO_2 TPD measurements were carried out on a Micromeritics AutoChem II 2920. The NT/ANT samples were outgases at 200 ^oC under a helium flow for 6 h prior to the measurements. The samples were then cooled to 50 ^oC and exposed to pure CO_2 for 2 h. The TPD measurements were performed via increasing the temperature with a ramp rate of 5 ^oC/min under a helium flow. The desorbed species were monitored by a thermal conductive detector.

4-1-8 CO_2 and CH_4 adsorption

The CO_2 and CH_4 adsorption measurements were carried out on a home-made quartz crystal microbalance (QCM) apparatus in a pressure and temperature control chamber. The NT or ANT gel samples were applied dropwise on a quartz crystal resonator with deposited gold electrodes. The samples were outgassed at 200 ^oC for 12 h and then exposed to the CO_2 or CH_4 gas at a range of pressures at 30^oC for recording the adsorption isotherms. The frequency of the quartz crystal resonators with NT/ANT samples were recorded at a given CO_2 or CH_4 pressure and then converted to the sample mass. The adsorption quantity at a given pressure and temperature could thus be obtained.

4-2 Structure, Crystallinity, and Porosity

The morphology of NT and ANT was evaluated by transmission electron microscopy (TEM). The TEM images of both samples are shown in Figure 4.1. The ANT sample (Figure 4.1 a and b) show almost identical rod-like structure and similar dimensions (lengths and diameters) to the NT sample. TEM images provide visual evidence suggesting that the morphology and dimensions of aluminosilicate nanotubes stay unchanged with a 20% AMTES substitution for TEOS in synthesis. Additionally, the images indicate that the products in both NT and ANT samples are nanotubes.

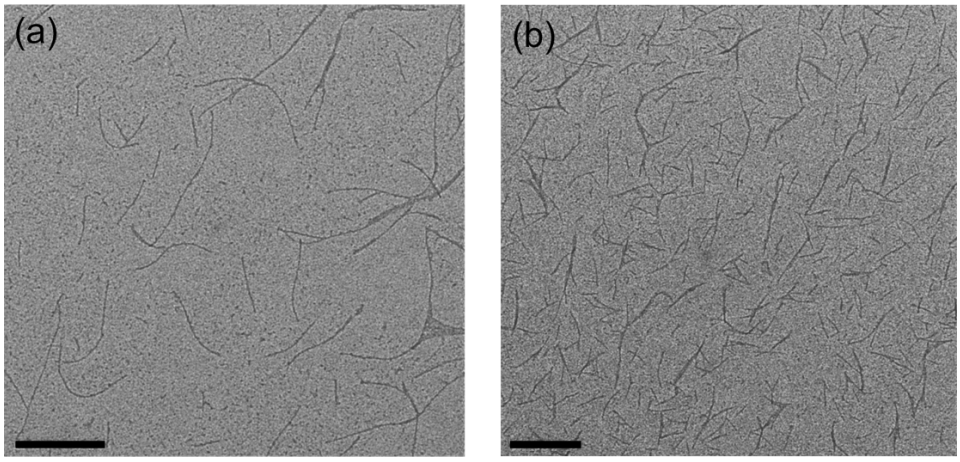

Figure 4.1 TEM images of (a) NT and (b) ANT.

X-ray diffraction (XRD) can be used to further confirm the nanotubular structure of the functionalized nanotube sample (ANT). Figure 4.2a summarizes the simulated and experimental XRD patterns of ANT and NT. the XRD patterns of nanotubular materials are strongly related to nanotube bundling characteristics. Specifically, the powder XRD simulations suggest that the nanotubes with outer diameters of 2.3 nm cause a "shoulder" at 5-6^{o} 2θ in the XRD patterns with the formation of small bundles with three or four nanotubes in the samples. Since both NT and ANT samples have nearly identical XRD patterns with "shoulders" 5-6^{o} 2θ, it implies that both nanotubular materials have very similar outer diameters and packing characteristics.

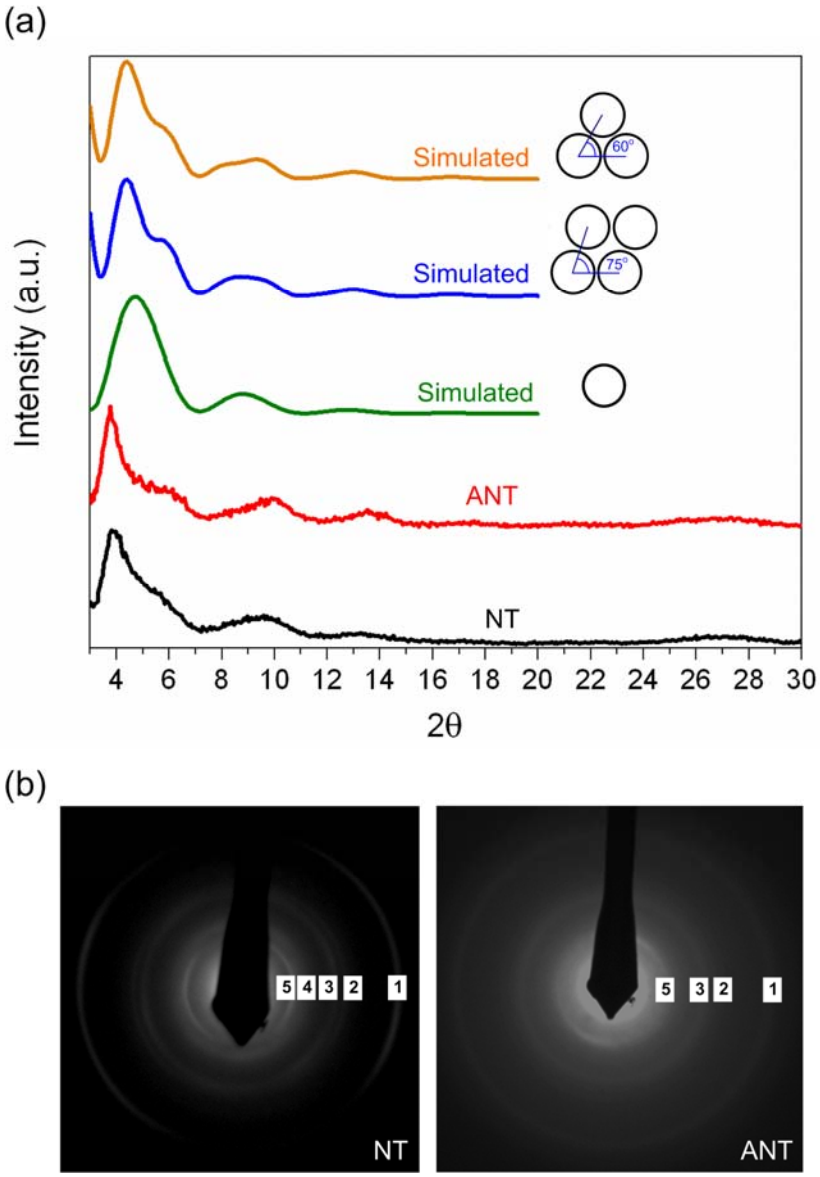

Figure 4.2 (a) Simulated powder X-ray diffraction patterns of nanotubes with various packing characteristics (top three spectra) and experimental powder X-ray diffraction patterns of NT and ANT (bottom two spectra). (b) Electron diffraction patterns of NT and ANT.

While XRD provides an unambiguous evidence of the presence of the nanotubular structure for NT and ANT, electron diffraction (ED) can probe the crystallinity along the long-axis of nanotubular materials. The experimental ED patterns are summarized in Figure 4.2b; and the Miller index and corresponding *d*-spacings for the five most prominent rings in the ED patterns for NT and ANT are tabulated in Table 4.1. ANT shows three peaks indexed (006), (004) and (002), which are also observed in NT and are from the crystallinity along the long-axis of the system.[42] This suggests that ANT maintains the same atomic level periodicity along the z-direction with NT, regardless of a 20% AMTES substitution for TEOS in the synthesis. However, the absence of peak (071), which is found in NT, for ANT is likely due to the partial incorporation of the organosilanes (AMTES) suppressing the symmetry of the system.

Table 4.1. *d*-Spacings of Rings Appearing in the ED Patterns of NT and ANT

	NT		**ANT**	
Reflection	*d*-spacing (Å)	*hkl*	*d*-spacing (Å)	*hkl*
1	1.4	006	1.4	006
2	2.1	004	2.1	004
3	2.2	063	2.2	063
4	3.2	071	--	--
5	4.3	002	4.3	002

Nitrogen physisorption is an excellent tool to investigate the porosity of the prepared nanotube samples. The physisorption isotherms of NT and ANT (Figure 4.3) show IUPAC type I characteristics,[74] suggesting they are both microporous materials. The lower adsorption capacity of ANT indicates the presence of the aminomethyl groups, from partially substituted AMTES, immobilized at the interior of ANT. In particular, the

larger size of aminomethyl (from AMTES) than hydroxyl (from TEOS) groups can reasonably cause the reduction of adsorption capacity from NT (100% TEOS) to ANT (80% TEOS, 20% AMTES). Given the volumes of the hydroxyl and the aminomethyl groups (16.9 and 38.1 $Å^3$), the fractional organic substitution ratio of ANT can be quantified by comparing the micropore volume of NT and ANT. The derived fractional organic substitution for ANT is 0.25, which is close to the substitution ratio of AMTES for TEOS (0.2) in ANT synthesis. However, the slight overestimation of the fractional organic substitution from the nitrogen physisorption analysis is likely due to the "corrugated" interior surface of the ANT caused by a combination of both hydroxyl and the aminomethyl groups. The irregularity of the inner surfaces of microporous materials could thus cause an underestimation of the pore volume for ANT, which leads to an overestimation of the actual fractional organic substitution ratio.

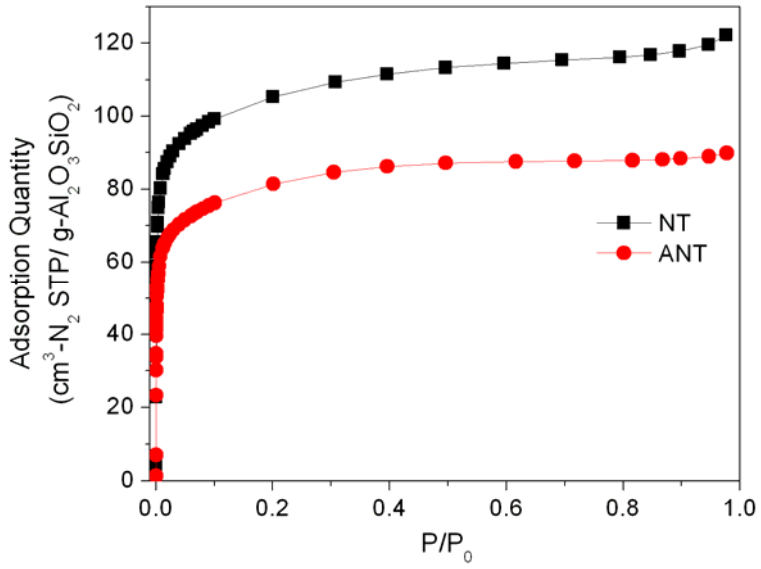

Figure 4.3 Nitrogen physisorption isotherms of NT and ANT.

4-3 Surface Chemistry and Coordination Environment

FT-Raman spectroscopy was employed for investigating the surface functional groups of NT and ANT. The FT-Raman spectra for NT and ANT samples are shown in

Figure 4.4. The additional peaks (1298, 1450, 1506, and 2950 cm^{-1}) from the ANT sample, in comparison to the NT sample, can be assigned to C-N stretching, C-H deformation, C-N deformation, C-H stretching vibration respectively.[107] These observed vibrational modes demonstrate the presence of the aminomethyl group in the ANT sample.

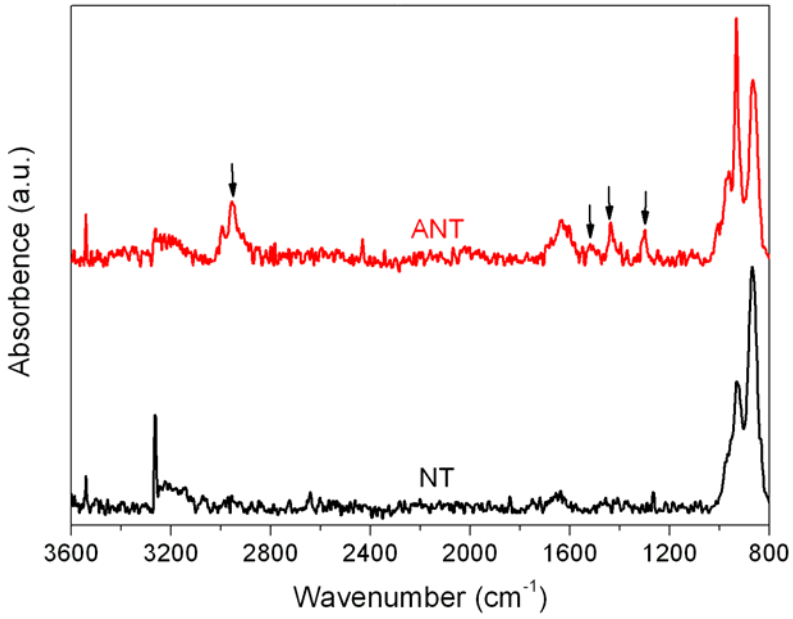

Figure 4.4 FT-Raman spectra for NT and ANT. The arrows point out peaks assigned to CN and CH deformation/stretching vibrations for the ANT sample.

To establish that nanotubes containing aminomethyl groups on the interior walls have been obtained, the surface functional groups and silicon/aluminum coordination environments in the ANTs can be further evaluated by ^{13}C, ^{29}Si, and ^{27}Al solid-state NMR spectroscopy (Figure 4.5).

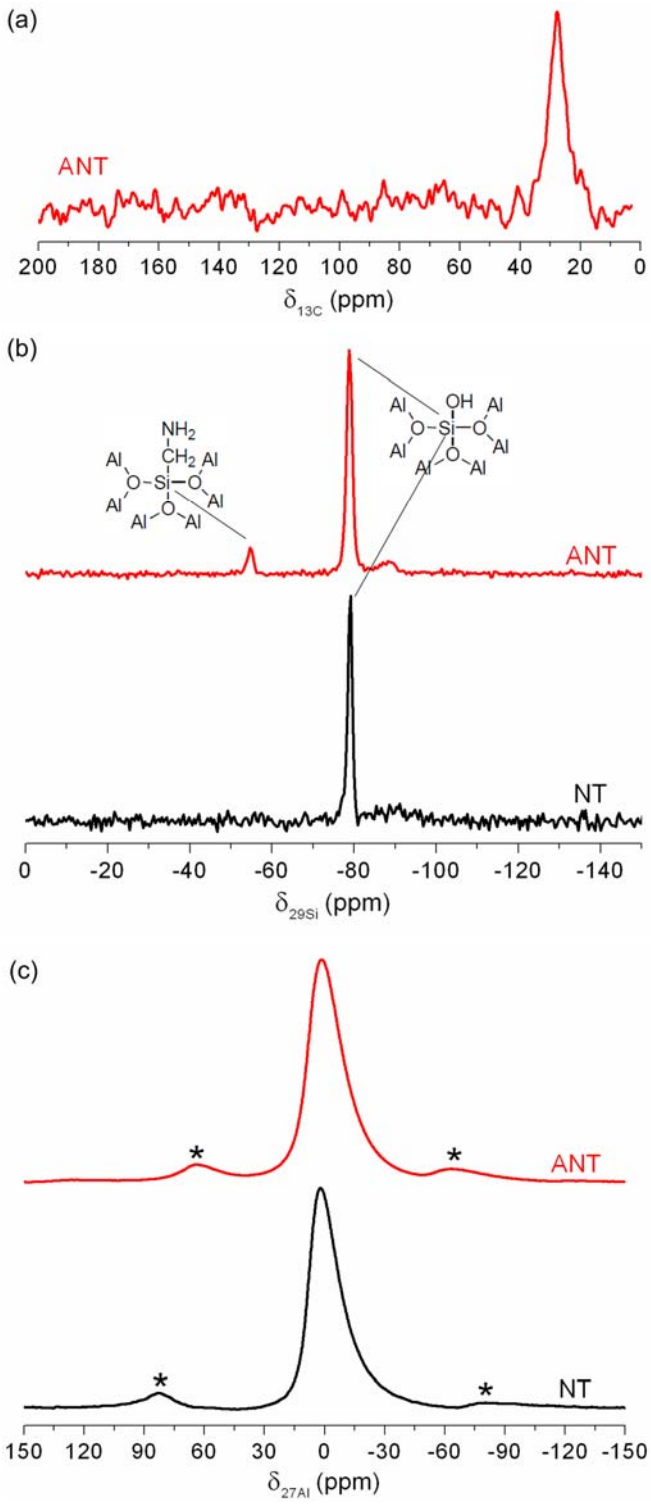

Figure 4.5 (a) ^{13}C CP-MAS (b) ^{29}Si DP and (c) ^{27}Al NMR spectra for NT and ANT samples.

In ^{13}C cross polarization magic angle spinning (CP-MAS) NMR spectrum of ANT (Figure 4.5a), a single peak at 28 ppm, owing to the carbon atom from the aminomethyl group, supports the presence of the aminomethyl moiety. This is in good agreement with the observations from FT-Raman characterization. Furthermore, the absence of additional signals in this spectrum indicates a depletion of ethoxy groups from the starting reagent, AMTES, for ANT synthesis. The depletion of ethoxy groups of the starting silane AMTES suggests that the silicon atom from AMTES either forms a T^3(3Si) framework by polymerization through many AMTES molecules or forms a T^3(6Al) framework, where on silicon atoms is connecting to six aluminum atoms with three three-coordinated oxygens.[97,108]

^{29}Si direct polarization (DP) NMR was employed for determining the silicon frameworks from for ANT (Figure 4.5b). For both NT and ANT samples, the peak at -79 ppm is known as the Q^3(6Al) framework,[59,97] which comes from the common silicon source, TEOS, for both samples. The peak at -57 ppm, observed only in the spectrum of ANT but not of NT, is likely from the additional silicon source (AMTES) for ANT synthesis. According to the aforementioned discussion regarding the absence of the ethoxy groups from AMTES, the peak at -57 ppm could be assigned to either T^3(3Si) or T^3(6Al) silicon. To determine the peak assignment between these two possiblities, a control experiment was thereby performed via immobilization of AMTES on porous silica support (SBA-15), which resulted in a combination of T^1(1Si), T^2(2Si), and T^3(3Si) silicons. When characterizing the silicon frameworks for the control sample, the ^{29}Si chemical shift of the T^3(3Si) silicon was found at -72 ppm, which is not close to -57ppm. Hence, the peak at -57 ppm for ANT is very likely due to the T^3(6Al) silicon connecting to the aminomethyl group, originated from the aminosilane AMTES for ANT synthesis. Furthermore, the DP NMR spectrum can be used for quantifying the ratio between different frameworks. For the ANT sample, the silicon fraction of T^3(6Al) in the sample

is 0.17, which is close to the silane fraction of AMTES in the ANT synthesis solution. In the ^{27}Al spectra (Figure 4.5c), the NT and ANT samples are nearly identical. The peak at -4 ppm is due to the octahedral aluminum framework in the aluminosilicate nanotube system.

Although the discussion on ^{29}Si chemical shifts present above suggests that the peak at -57ppm in ANT could be reasonably assigned to $T^3(6Al)$, which comes from silicon atoms from AMTES connecting with six aluminum atoms. To further confirm the connectivity between silicon (from both TEOS and AMTES as silicon sources) and aluminum atoms in the ANT sample, ^{29}Si-^{27}Al transfer of populations in double resonance (TRAPDOR) experiments were employed. The TRAPDOR technique directly probes the dipolar coupling between a spin = 1/2 nucleus (^{29}Si) and a spin > 1/2 nucleus (^{27}Al) and thereby could characterize the connectivity of these two nuclei.[109,110] The spectra obtained from TRAPOR experiments for the ANT sample and a control sample composed of a physical mixture of mesoporous silica (SBA-15) and α-alumina are shown in Figure 4.6.

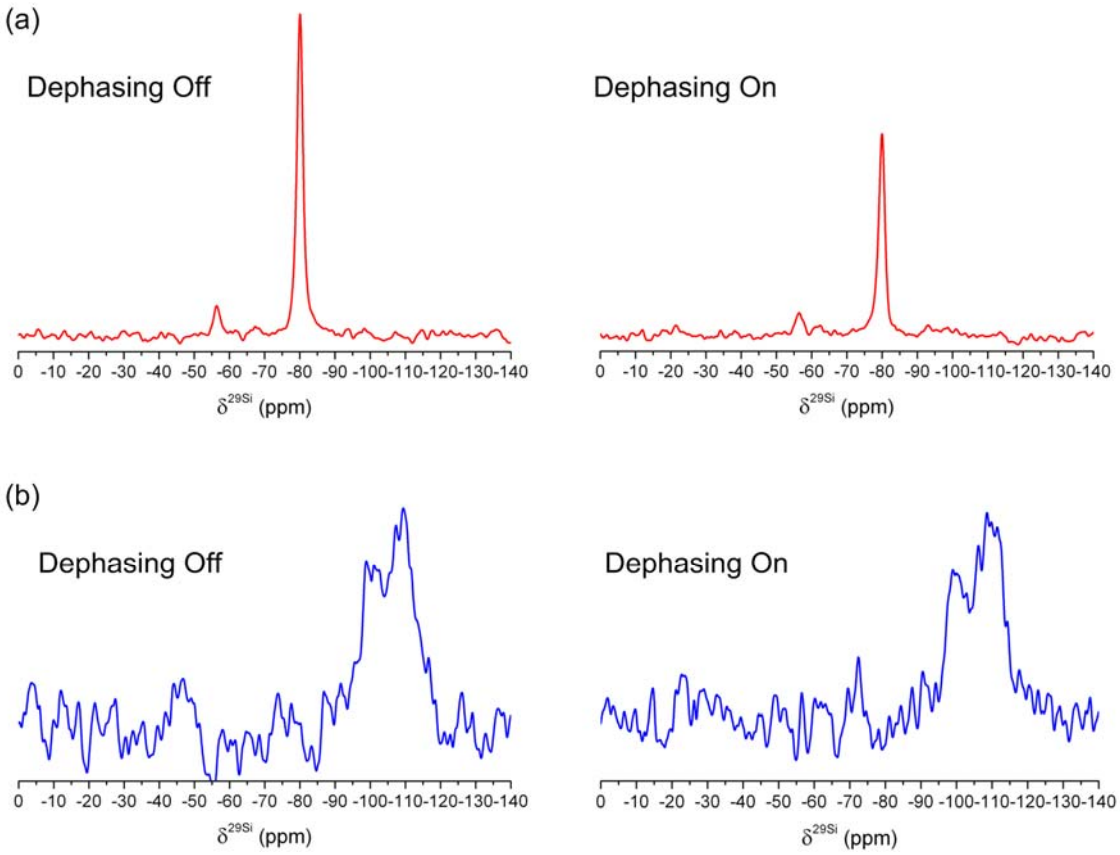

Figure 4.6 TRAPDOR results for (a) ANT and (b) a physical mixture of SBA-15 and α-alumina

In the presence of a dephasing signal from ^{27}Al, the peak intensities in ^{29}Si spectra will be reduced when the samples possess atomic level connectivity between silicon and aluminum atoms.[109,110] On the other hand, the peak intensities in ^{29}Si spectra will remain unchanged with a ^{27}Al dephasing signal for samples without silicon-aluminum connectivity. Quantitative peak intensity estimations are summarized in Table 4.2.

Table 4.2 Quantitative Analysis of TRAPDOR Experiments for ANT and Control Samples.

	ANT		Control Sample
Si Framework	Q^3(6Al)	T^3(6Al)	Q^1(1Si), Q^2(2Si), and Q^3(3Si)
Integration Range	-70 to -90 ppm	-54 to -60 ppm	-80 to -120 ppm
Intensity Ratio*	0.63	0.81	1.01

*The intensity ratio is the ratio between the ^{29}Si NMR peak intensities with and without a ^{27}Al dephasing signal.

According to the quantitative analysis from TRAPDOR experiments, significant intensity reductions in the presence of a ^{27}Al dephasing signal for the silicon frameworks (Q^3(6Al) and T^3(6Al)) in ANT are observed, whereas no intensity decrease is found for the control sample. This provides an unambiguous evidence of the Si-Al connectivity for both Q^3(6Al) and T^3(6Al) silicon in ANT samples. In other words, both starting silicon reagents (TEOS and AMTES) are built in the aluminosilicate nanotube frameworks through connections with aluminum atoms in the final product, as opposed to forming a separate phase. The TRAPDOR results, on the other hand, also strongly supports the assignment of the -57ppm peak to T^3(6Al) silicon framework.

According to the FT-Raman and detailed solid-state NMR analyses, I propose a molecular structural model for the as-made ANT (Figure 4.7). The ANT model composes

two distinct frameworks, Q^3(6Al) and T^3(6Al), with a ratio of 5:1, and aminomethyl groups immobilized at the interior surfaces, which could provide a base functionality for various applications.

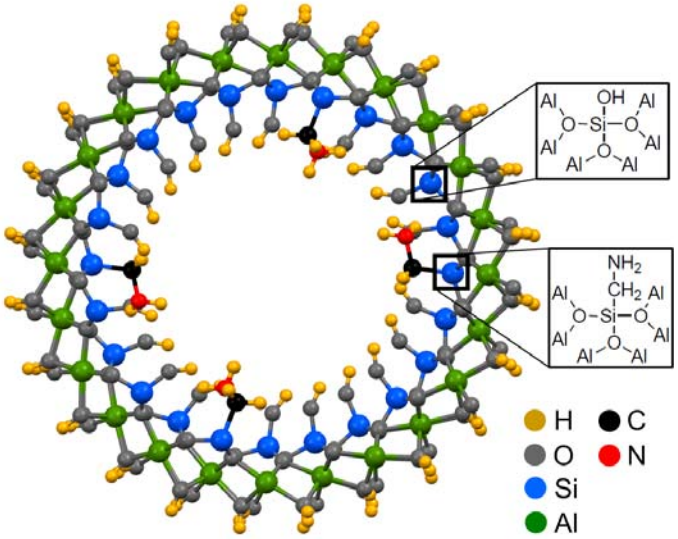

Figure 4.7 Proposed structure of as-made ANT.

4-4 Adsorption properties of functionalized nanotubes

The primary amine group is known for its ability for binding CO_2. I applied CO_2 temperature programmed desorption (TPD) for assessing how the amine groups immobilized at the nanotube inner surfaces impact their interaction with CO_2 (Figure 4.8).

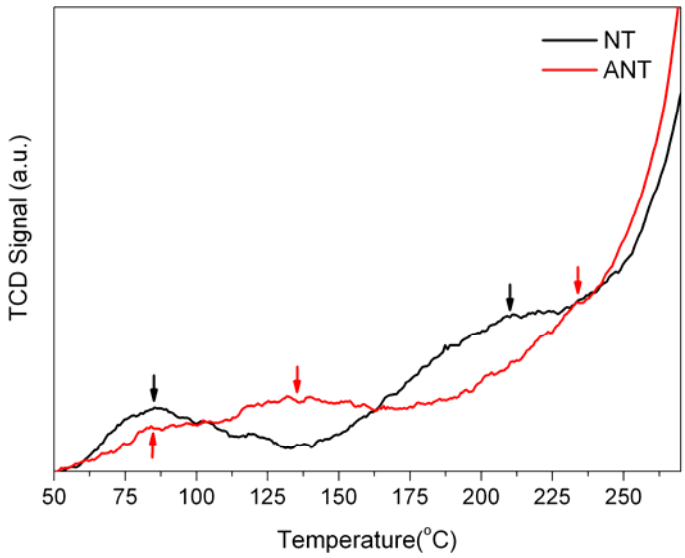

Figure 4.8 Temperature programmed desorption of CO_2 for NT and ANT samples monitored by thermal conductivity detector (TCD). The arrows point out where CO_2 desorption is observed.

According the CO_2 TPD results, the observed CO_2 desorption for ANT shifts towards higher temperatures in comparison to NT. It could be owing to a stronger interaction between CO_2 and primary amine groups than CO_2 and silanol groups.

Gas adsorption isotherms can provide more physical insight of the adsorption properties of the bare and interior-functionalized nanotube materials. The CO_2/CH_4

adsorption measurements performed on the quartz crystal microbalance (QCM) for NT and ANT samples are summarized in Figure 4.9.

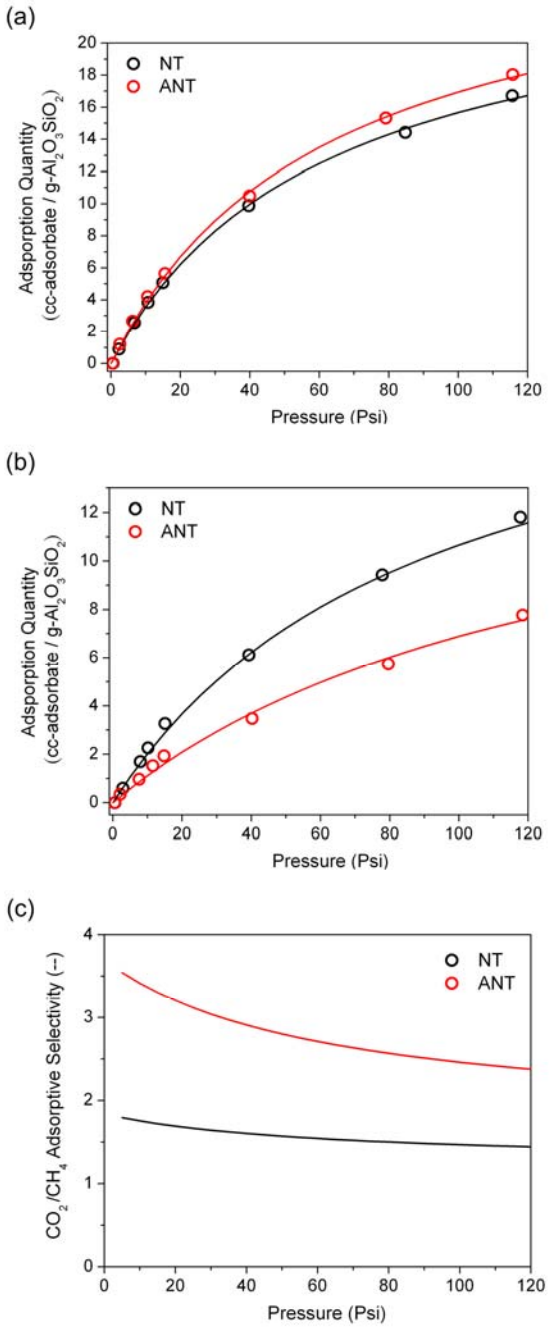

Figure 4.9 The adsorption isotherms of (a) CO_2 and (b) CH_4, and (c) the adsorptive selectivity of NTs and ANTs. The open symbols represent the raw data and the solid curves represent the fit of the results *via* the Langmuir model.

In general, a similar CO_2 capacity, a lower CH_4 capacity, and a higher CO_2/CH_4 selectivity are found for the ANT sample. To gain more physical insight of the adsorption behavior for the interior-functionalized nanotube materials, the measured adsorption isotherms were analyzed by the Langmuir equation:

$$C = \frac{C_m \cdot K \cdot P}{1 + K \cdot P} \qquad (4.1)$$

where C is the measured adsorption quantity, P is the pressure, and K is the Langmuir constant. The isotherm reduces to a linear relationship between C and P at low pressure regime. The parameters in the Langmuir equation obtained from fitting the raw data are presented in Table 4.3.

Table 4.3 Parameters in the Langmuir equation for CO_2/CH_4 adsorption in the NT/ANT samples

	CO_2		CH_4	
	NT	ANT	NT	ANT
K (1/psi)	0.016	0.016	0.011	0.007
C_m (cc-adsorbate / g-$Al_2O_3SiO_2$)	25.3	27.5	20.4	16.2

In the CH_4 adsorption, the parameters responsible for the adsorption at low pressure regime (K) and at the high pressure regime (C_m) both show a significant decrease with the amine-functionalization. The decrease of K can be attributed to the immobilization of amine groups, which substitute the hydroxyl groups and possess lower CH_4 affinity than hydroxyl groups. A lower C_m observed in the ANT sample is likely owing to its lower pore volume, which reduces the CH_4 capacity in the high pressure regime. Similar adsorption behavior on functionalized microporous materials was reported previously.[111]

In CO_2 adsorption, the Henry's constant *K* does not change with amine functionalization. Although the primary amine groups are known for their high CO_2 affinity, they might be "deactivated" by the possible bound perchlorate ions from the perchloric acid used for the nanotube synthesis. Hence, the only "active sites" for CO_2 adsorption in ANT sample are the hydroxyl groups just like in the NT sample. However, a slightly larger C_m is observed for the ANT than NT. It could be because the high pressure CO_2 can weaken the bond between the primary amines, presented in the ANT, and the perchlorate ions; and the amine groups start being active for binding CO_2. Although not presented in this thesis, further studies for testing the hypothesis of amine groups in ANT being bound to perchlorate ions are undergoing.

4-5 Summary

An approach for functionalizing the inner surface of single-walled aluminosilicate nanotubes with a one-step synthesis has been elucidated. A comprehensive investigation of the resulting solids using nitrogen physisorption, powder X-ray diffraction (XRD), transmission electron microscopy (TEM), ^{29}Si and ^{13}C solid-state NMR, and CO_2 temperature programmed desorption provides a detailed understanding of the porosity, structure, and surface chemistry of the functionalized nanotubes. As an example of the potential applications, I showed that the functionalization approach allows for control the CO_2/CH_4 selectivity of the SWNT, which could be applied to CO_2 removal from natural gas.

CHAPTER 5

MODELING MOLECULAR TRANSPORT IN COMPOSITE MEMBRANES WITH TUBULAR FILLERS

The preceding Chapters 2-4 have described new advances in the synthetic and functionalization chemistry of single-walled metal oxide nanotubes for use in molecular transport applications, whereas the following Chapters 6-7 describe the fabrication of novel membranes using these materials. To create a reliable theoretical framework governing the mass transport properties of such membranes, in this chapter I develop the theory of mass transport in membranes containing nanotubular fillers. Polymer/zeolite composite membranes for molecular separations have been studied for more than two decades. The well-known Maxwell model[34,112,113] provides a description of their performance in terms of the permeability and volume fractions of each phase (the polymer and the filler):

$$\frac{P_{eff}}{P_m} = \frac{P_f + (n-1)P_m - (n-1)(P_m - P_f)\Phi_f}{P_f + (n-1)P_m + (P_m - P_f)\Phi_f} \qquad (5.1)$$

where P_{eff} is the effective permeability of the composite membrane, P_m is the permeability of the polymer matrix, P_f is the permeability of the filler, Φ_f is the volume fraction of the filler (varies from 0 to 1), and n is the shape factor of the filler. When considering near-spherical fillers, such as typical zeolite crystals, the shape factor n is taken as n = 3. Equation (5.1) is then known as the "original Maxwell model", and has been widely used to predict the permeability of polymer/zeolite composite membranes. On the other hand, n = 6 for cylindrical fillers in a matrix, such as nanorods in a fluid. In this case, Equation (5.1) is also known as the Hamilton-Crosser model.[114,115] Although the Maxwell model inclusive of a shape factor can model permeation in composite

membranes containing cylindrical fillers, the assumption that the fillers have isotropic permeability renders it inapplicable to nanotubes, wherein molecular transport is confined to the axial direction of the nanotubes. Furthermore, the Maxwell model for non-spherical fillers assumes that the fillers are randomly oriented in the matrix, whereas previous studies have suggested that nanotubes can be well-aligned in a liquid-phase dispersion or a solid-phase matrix.[15,16,116] Hence, inclusion of the one-dimensional transport phenomena through nanotubes, and the orientation of the tubular fillers in the matrix, are both critical for a reasonable estimation of effective permeability in nanotube-containing composite membranes. An analytical model incorporating these factors would be useful in the design and evaluation of nanotube-containing membranes for separations applications.

In this chapter, I present an analytical model to estimate permeation in composite membranes with tubular fillers. Several limiting cases of the model are assessed. This model was then used to investigate the permeation performance of composite membranes as a function of parameters including the filler volume fraction, orientation, and aspect ratio, as well as the relative permeabilities of the nanotubes and the matrix material. Furthermore, the effects of defects such as voids at the filler/matrix interfaces (due to poor compatibility between the two phases)[117-119] and pinholes that sometimes form under non-ideal membrane fabrication conditions (for example, fast evaporation of the solvent, or the size of the fillers being close to the membrane thickness),[120] are included. The performance of ideal (defect-free) and non-ideal (defective) composite membranes with tubular fillers in binary mixture separation is investigated using the model. Finally, I assess the potential performance enhancement of a state-of-the-art polymeric membrane by tubular and spherical fillers, and an advanced configuration of composite membrane with tubular fillers is discussed.

5-1 Model derivation

5-1-1 Transport resistances

Membrane permeation can be considered as being driven by the pressure differential between the feed and the permeate side of a membrane. The molecular flux (number of molecules transported across the membrane per unit time per unit membrane surface area) can be estimated by a simple permeance equation[25,121,122] that depicts the linear dependence between the flux (J) and the partial pressure differential of a certain species (Δp):

$$J = \frac{P_{eff}}{t}\Delta p \qquad (5.2)$$

where t is the thickness of the membrane, and P_{eff} is the effective permeability which is the product of diffusivity (kinetic effect) and solubility coefficient (thermodynamic effect) of the molecular species in the membrane material. One can also consider t/P_{eff} as the resistance of the membrane.

During mass transport in a composite membrane with tubular fillers, each potential molecular path (involving a different number of tubular fillers) has a different transport resistance (Figure 5.1a). The resistance of the path without any tubular filler can be expressed as t_0/P_m, where t_0 the product of the membrane thickness (t) and the tortuosity, τ, caused by the detour taken by molecules that strike the impermeable part (*i.e.* the side wall) of the tubular filler. However, because the outer diameter of the tubular filler (< 20 nm) is often much smaller than the membrane thickness (> 1 μm), the detour is seen to be quite minor for moderate or low volume fractions of the fillers. In other words, τ can be taken as close to unity for these cases, in contrast to the greater tortuosity caused by other filler shapes (e.g. The total resistance of a path containing a certain number of fillers (n_f) can be modeled as two resistances in series: the matrix

($t_{m,nf}/P_m$) and the tubular fillers ($t_{f,nf}/P_m$), where $t_{m,nf}$ and $t_{f,nf}$ are the path lengths of the molecule through the matrix and the filler respectively, for the pathway containing n_f fillers. To estimate the total membrane resistance from all the possible resistances-in-parallel, the volume fraction of each distinct path (*i.e.* containing different number of tubular fillers and different path lengths) must be known. Unfortunately, it is difficult to measure these individual volume fractions experimentally or estimate them theoretically. Hence, an analytical result cannot easily be derived from this model.

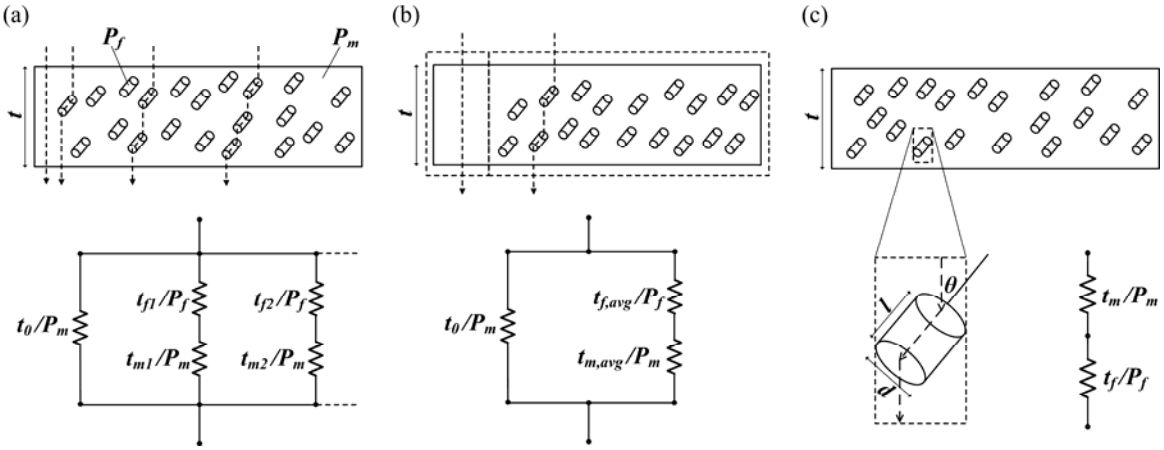

Figure 5.1 (a) An illustration of various molecular permeation paths through a composite membrane containing tubular fillers; and the total resistances-in-parallel attributed to each possible permeation pathway. (b) Molecular permeation through two artificial membrane domains: one without, and one with, tubular fillers; and the transport resistances of the two domains in parallel. (c) The specifications of a tubular filler, and the total resistance contributed by the resistance of the matrix and fillers in series.

To deduce an analytical estimate of the effective permeability of a composite membrane with tubular fillers, the above model is simplified to that of a membrane composed of two types of resistances in parallel: one without fillers and one with fillers (Figure 5.1b). For the resistance of the molecular path containing fillers, one can consider an "average" path with an average number of fillers. Hence the resistance of the domain

containing fillers can be expressed by two resistances in series: one from the matrix ($t_{m,avg}/P_m$) and one from the tubular fillers ($t_{f,avg}/P_m$), where $t_{m,avg}$ and $t_{f,avg}$ are the path length of a molecule passing through the matrix and the filler respectively, for an average number of fillers. However, it is challenging to determine the filler volume fraction in the domain with the average number of fillers (since it would be larger than the bulk volume fraction of fillers); as well as the volume ratio between the domains with, and without, fillers. Hence, this two-domain model also does not lead to an analytical expression unless further simplified (below). Nevertheless, three cases are examined in which the permeability of the filler (for the desired molecular species) is much larger than, much smaller than, or similar to, the permeability of the matrix. When the filler permeability is much larger than that of the matrix, the resistance of the domain with fillers would be considerably smaller than the resistance of the domain without fillers. The overall resistance would be dominated by the domain with fillers and the permeability can be estimated by the two types of the resistances in that domain. In this case, the model of Figure 5-1b can be simplified into that of Figure 5.1c. Furthermore, in the case that the filler permeability is much smaller than that of the matrix, the resistance of the domain with fillers can be expected to be much larger than that of the domain without fillers. Hence, the effective permeability would be either close to the permeability of the matrix (for low volume fraction of the fillers) or significantly lower than the permeability of the matrix (for high volume fraction of the fillers, due to the high tortuosity caused by the large amount of low-permeability fillers). Finally, for the case where the filler permeability is of the same order of magnitude as the matrix permeability, the effective permeability for the composite membrane would be close to the permeability of the matrix. Of these three cases, it is observed that only the case of filler permeability much larger than the matrix permeability can have a positive impact on the effective permeability. Considering the fact that fillers are presumably incorporated to enhance the

permeability of the membrane towards the desirable molecular species, it is appropriate to focus on this case (Figure 5.1c).

5-1-2 Resistance-in-series model for a fixed tubular filler orientation

Permeation through a composite membrane with tubular fillers oriented in a fixed direction is considered first (Figure 5.1c), wherein the matrix and the filler are described by the permeabilities P_m and P_f, respectively. The tubular filler is described by an outer diameter d, length l, and an orientation described by an angle θ (varying from 0 to $\pi/2$) with respect to the axis parallel to the bulk-phase transport direction. The 3-D orientation of the tubular filler is most rigorously described by two independent parameters, but only one degree of freedom (θ) is necessary to describe permeation through a membrane since the fillers can be reasonably projected on a 2-D plane that provides an equivalent permeation pathway for a given membrane permeation process. The total resistance of this composite membrane is derived by considering the path of a single molecule traversing the membrane from the feed side to the permeate side. For the case of a "thick composite membrane" (*i.e.* the thickness of the membrane is much larger than the largest dimension of the filler), the path of a single molecule traverses both the matrix and the filler phases. Therefore, the total resistance is expressed as a series combination of the resistance from the matrix and the resistance from the filler in series (Figure 5.1c). The permeance equation becomes:

$$J = \frac{\Delta p}{\frac{t_m}{P_m} + \frac{t_f}{P_f}} \qquad (5.3)$$

where t_m and t_f are the total "transport lengths" of the molecule through the matrix and the filler respectively. Furthermore, t_f can be expressed in terms of the filler dimensions and the average number of fillers (n_f) in the path from the feed to the permeate side: $t_f = l.n_f$.

On the other hand, t_m can be considered as a "reduced" membrane thickness due to the incorporation of fillers, and can be written as:

$$t_m = t - n_f \cdot l \cdot \cos\theta \qquad (5.4)$$

The projected 1-D length in the membrane transport direction for a single tubular filler, according to Figure 1c, is $l\cos\theta+d\sin\theta$. The number of fillers in the molecular path, n_f, can be related to the total membrane thickness, the projected length of a single tubular filler, and the filler volume fraction, Φ_f:

$$n_f = \frac{t}{l \cdot \cos\theta + d \cdot \sin\theta}\Phi_f \qquad (5.5)$$

Combining Equations 5.3 to 5.5, the flux through a composite membrane with tubular fillers is written as:

$$J = \frac{\Delta p}{t\left(\frac{1}{P_m}\left(1 - \frac{l \cdot \cos\theta}{l \cdot \cos\theta + d \cdot \sin\theta}\Phi_f\right) + \frac{1}{P_f}\left(\frac{l}{l \cdot \cos\theta + d \cdot \sin\theta}\right)\Phi_f\right)} \qquad (5.6)$$

Comparing Equations 5.2 and 5.6, the permeability enhancement factor (P_{eff}/P_m) is defined, which describes the change in permeability of the nanotube-containing membrane over the pure matrix material:

$$\frac{P_{eff}}{P_m} = \left(\left(1 - \frac{\cos\theta}{\cos\theta + \frac{1}{\alpha}\cdot\sin\theta}\Phi_f\right) + \frac{P_m}{P_f}\left(\frac{1}{\cos\theta + \frac{1}{\alpha}\cdot\sin\theta}\right)\Phi_f\right)^{-1} \qquad (5.7)$$

where $\alpha = l/d$ is the aspect ratio of the tubular fillers. Equation 5.7 summarizes the model (referred to as the "KJN model" in this paper) for permeation in a composite membrane

with tubular fillers of a fixed orientation. According to the model, P_{eff}/P_m is a function of the filler volume fraction (Φ_f), orientation (θ), aspect ratio (α), and the permeability ratio of the filler and the matrix (P_f/P_m). Since the permeability is a product of the diffusivity and the solubility coefficient, the permeability ratio used in this work includes the relative kinetics of molecules transporting through the interface between the matrix and the filler phase, as well as the solubility equilibrium at the matrix-filler interfaces.

5-1-3 Transport in composite membranes with a distribution of tubular filler orientations

Although a few experimental studies suggest that tubular fillers can be aligned in a specific direction in composite membranes, the conventional solvent-evaporation

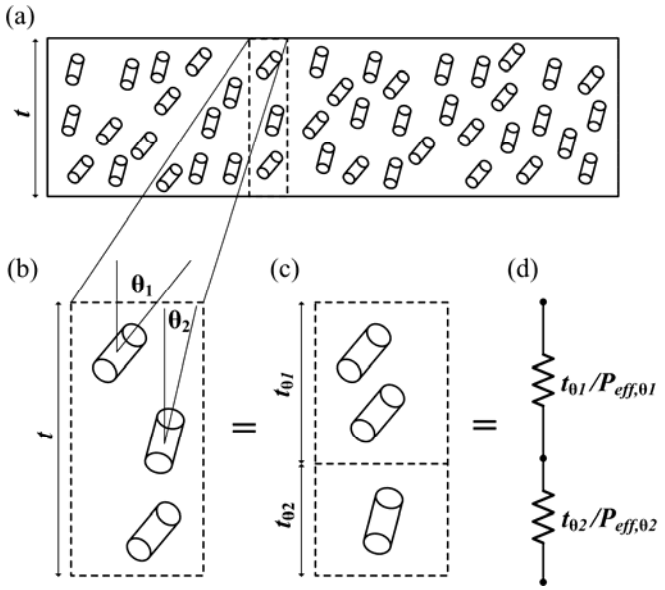

Figure 5.2 (a) An illustration of a composite membrane with fillers of two different orientations. (b) A slice of this composite membrane. (c) An artificial slice" which provides equivalent permeation performance to the "real slice", and can be segregated into two domains with different orientations. (d) The total resistance of this slice comes from the resistance of each domain in series.

fabrication method yields membranes with tubular fillers that are randomly oriented.[123-125] Equation 5.7 should hence be extended to include the distribution of filler orientations. Consider first a membrane with fillers of two orientations, θ_1 and θ_2 (Figure 5.2a). It is first assumed that the fillers with different orientations are uniformly dispersed in the matrix. Based upon the assumption of uniform dispersion, every "artificial slice" (of thickness t, cut along the molecular transport direction, and no wider than the dimensions of one filler, as shown in Figure 5.2b) has an identical effective permeability. Hence, only the unit slice shown in Figure 5.2b need be taken into account. It is then assumed that within the unit slice, different permutations of fillers along the molecular path will provide an identical permeation performance. Hence, one can group fillers with the orientation of θ_1 on the top of the slice, and fillers with the orientation of θ_2 on the bottom (Figure 5.2c). These two domains occupy a thickness of $t_{\theta 1}$ and $t_{\theta 2}$, and are assigned effective permeabilities $P_{eff,\theta 1}$ and $P_{eff,\theta 2}$, respectively. The total resistance of the unit slice can be considered as a series combination of resistances (Figure 5.2d), and the flux through the unit slice is:

$$J = \frac{\Delta p}{\frac{t_{\theta 1}}{P_{eff,\theta 1}} + \frac{t_{\theta 2}}{P_{eff,\theta 2}}} \qquad (5.8)$$

The thickness of each domain is proportional to the fraction of the filler with a given orientation ($f(\theta_i)$) amongst all the fillers present in the whole membrane:

$$\frac{t_{\theta 1}}{f(\theta_1)} = \frac{t_{\theta 2}}{f(\theta_2)} \qquad (5.9)$$

The summation of $f(\theta_1)$ and $f(\theta_2)$ must be unity, and the summation of the domain thicknesses must equal the membrane thickness t. Therefore Equation 5.9 can be rewritten as:

$$J = \frac{\Delta p}{t\left(\frac{f(\theta_1)}{P_{eff,\theta 1}} + \frac{f(\theta_2)}{P_{eff,\theta 2}}\right)} \qquad (5.10)$$

The effective permeability of the membrane is hence given by:

$$\frac{1}{P_{eff}} = \frac{f(\theta_1)}{P_{eff,\theta 1}} + \frac{f(\theta_2)}{P_{eff,\theta 2}} \qquad (5.11)$$

The effective permeability of each domain with a fixed filler orientation, i.e., $P_{eff,\theta 1}$ and $P_{eff,\theta 2}$, can be calculated by Equation 5.7, where the filler volume fraction in each domain is the same as the filler volume fraction in the bulk phase (*i.e.* $\Phi_{f,\theta 1} = \Phi_{f,\theta 2} = \Phi_f$) regardless of the orientation and the the thickness for each domain described in Equation 5.10. An arbitrary distribution of filler orientations can now be generalized and Equation 5.12 can be extended into the following form:

$$\frac{1}{P_{eff}} = \int_{\theta=0}^{\theta=\pi/2} \frac{g(\theta)}{P_{eff,\theta}} d\theta \qquad (5.12)$$

where $g(\theta)$ is the normalized orientation distribution function of the filler with a tilt angle θ in relation to direction of membrane transport. The continuous function $g(\theta)$ has dimensions of $1/\theta$. Therefore, the permeability enhancement factor (P_{eff}/P_m) predicted by the KJN model is:

$$\frac{P_{eff}}{P_m} = \left[\int_{\theta=0}^{\theta=\pi/2} \frac{P_m}{P_{eff,\theta}} g(\theta) d\theta \right]^{-1} \qquad (5.13)$$

where $P_m / P_{eff,\theta}$ is again given by Equation (5.8). The integral of $g(\theta)$ from 0 to $\pi/2$ with respect to θ should equal to unity. Hence, the distribution function, $g(\theta)$, of a membrane with a completely random distribution of orientations of tubular fillers can be considered a constant equal to $2/\pi$. Hence the permeability enhancement factor becomes:

$$\frac{P_{eff}}{P_m} = \frac{\pi}{2} \cdot \left[\int_{0}^{\pi/2} \frac{P_m}{P_{eff,\theta}} d\theta \right]^{-1} \qquad (5.14)$$

5-1-4 Defects in composite membranes

The model developed in Sections 5-1-1 to 5-1-3 describes perfect membranes with no defects, whereas different types of defects are often formed during composite membrane fabrication. Specifically, as summarized in Figure 5.3a, the incompatibility between the filler and the matrix can create a void space surrounding the fillers. Additionally, the membrane may contain pinholes extending from the feed to the permeate side of the membrane. Such defects can significantly affect the membrane performance. Hence, it is critical to include them in permeation models and quantitatively assess their impact. When interfacial voids and pinholes are present, two more permeation paths are introduced. Firstly, a molecule at the filler/matrix interface can either diffuse through the tubular channel, or diffuse through the surrounding void space without entering the filler (since the side-wall of the tubular channel is insulated from the adjacent void space). Secondly, a pinhole can be modeled as an isolated channel with a relatively high permeability that allows molecules to bypass the membrane. A membrane with these two types of defects can be modeled as containing three pieces of side-by-side layers (Figure 5.3b). These include: *(i)* a defect-free membrane with tubular fillers, *(ii)* a membrane composed of matrix and voids, and *(iii)* a pinhole. Applying the resistances-in-parallel concept (Figure 5.3c), the effective permeability of a defective composite membrane (P_{eff}) is a linear combination of the permeability of each piece, weighed by its volume fraction:

$$P_{eff} = \frac{\Phi_f}{\Phi_f + \Phi_v + \Phi_p} P_{eff,f} + \frac{\Phi_v}{\Phi_f + \Phi_v + \Phi_p} P_{eff,v} + \frac{\Phi_p}{\Phi_f + \Phi_v + \Phi_p} P_p \qquad (5.15)$$

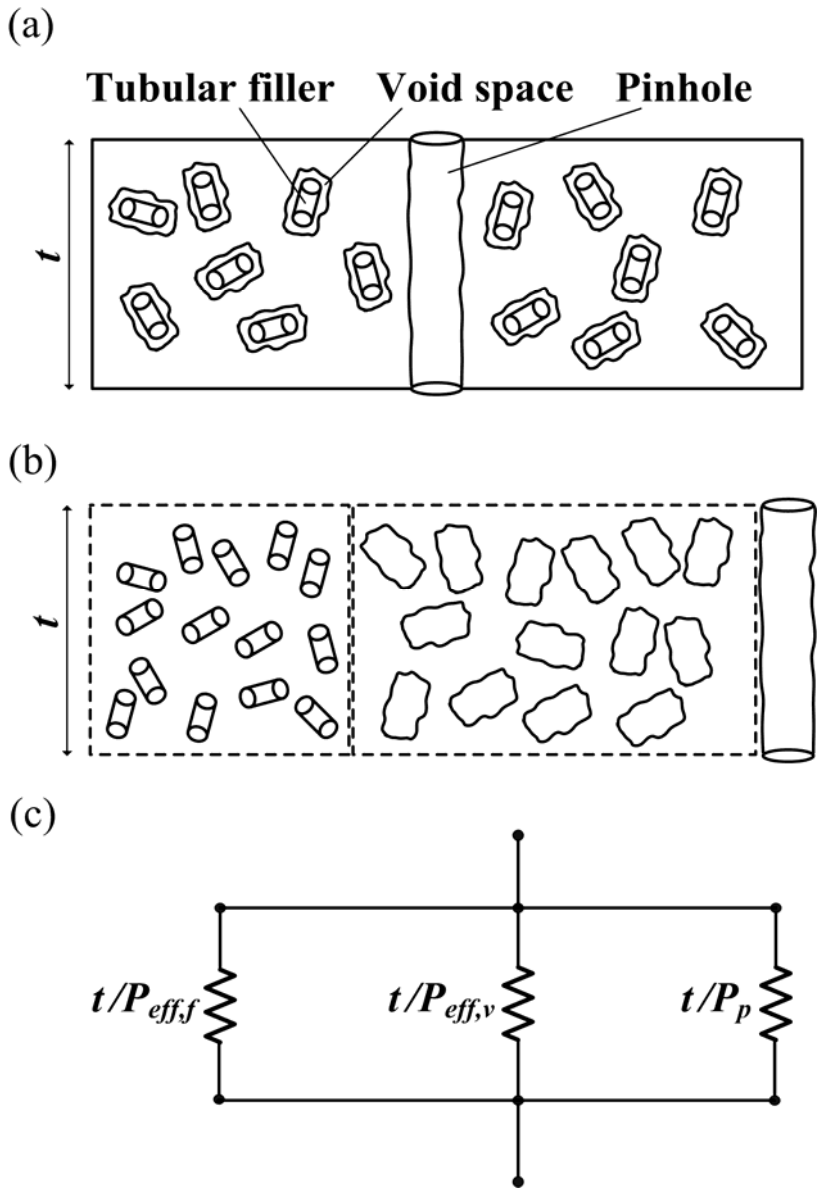

Figure 5.3 (a) An illustration of a non-ideal composite membrane with tubular fillers, void spaces, and pinholes. (b) An "artificial membrane" which provides equivalent permeation performance to the "real membrane" and can be segregated into three domains side by side: a defect-free composite membrane, a composite membrane with void space, and pinholes. (c) The total resistance of the "artificial membrane" can be considered as a combination of resistances from three domains in parallel.

where $P_{eff,f}$ and $P_{eff,v}$ are the effective permeabilities of the regions of the membrane composed of filler/matrix and void/matrix respectively; P_p is the permeability of the pinhole; and Φ_f, Φ_v, and Φ_p are the volume fractions of the imaginary pieces composed of filler/matrix, void/matrix, and pinhole respectively. The volume fraction is constrained by conservation of volume:

$$\Phi_f + \Phi_v + \Phi_p + \Phi_m = 1 \qquad (5.16)$$

where Φ_m is the overall volume fraction of the matrix material in the composite membrane. To apply Equation 5.15, Equation 5.13 can be utilized to estimate the effective permeability of the layer of an ideal composite membrane with tubular fillers ($P_{eff,f}$). The effective permeability ($P_{eff,v}$) of the piece containing the matrix and void spaces can be predicted by the Hamilton-Crosser model,[114] assuming that the void space is cylindrical in shape and the diffusion in the void space is isotropic:

$$\frac{P_{eff,v}}{P_m} = \frac{P_v + 5P_m - 5\left(P_m - P_v\right)\Phi_v}{P_v + 5P_m + \left(P_m - P_v\right)\Phi_v} \qquad (5.17)$$

Here P_v is the permeability in the void space. A previous study has suggested that the permeation mechanism in the void can be considered as Knudsen diffusion;[113] and that the solubility coefficient S can be estimated by the ideal gas law ($S_{IG} = 1/RT$). It is reasonable to assume that the pinholes follow the same permeation mechanism as the void spaces. As a result, the permeabilities of the void space (P_v) and of the pinhole (P_p) can be written as:

$$P_v = P_p = S_{IG} \cdot D_{Kn} = \frac{1}{RT} \cdot \sqrt{\frac{32r^2RT}{9\pi M}} \qquad (5.18)$$

where D_{Kn} is the Knudsen diffusivity, r is the average diameter of the pinhole or void space, and M is the molecular weight of the transported molecule.

5-2 Limiting cases of the model

5-2-1 Membranes without fillers or matrix

For the membrane comprised of only the matrix material or the fillers, $\Phi_f = 0$ or 1. Therefore Equation 5.6 reduces to that expected for single-phase membranes. For the membrane composed only of fillers ($\Phi_f = 1$) with an undesired orientation ($\theta = \pi/2$), Equation 5.6 becomes:

$$J = \frac{\Delta p}{\frac{1}{P_m} \cdot t + \frac{1}{P_f} \cdot \alpha \cdot t} \qquad (5.19)$$

The permeability of the matrix (P_m) is still present in the permeance equation because the gas molecules have to "hop between" the tubular fillers along the membrane transport direction in order to be able to pass through the membrane. However, since there is no matrix material really present in this system, one can assume that the inter-tubular "hops" from the tip of one nanotube to the other occur very fast relative to permeation through the fillers, i.e., the permeability of the hypothetical connecting "matrix" $P_m \rightarrow \infty$. Hence, one obtains:

$$J = \frac{P_f}{\alpha \cdot t} \Delta p \qquad (5.20)$$

where the effective permeability now becomes the permeability of the filler (P_f), and the characteristic length becomes the membrane thickness (t) multiplied by the aspect ratio of the tubular filler (α). When the tubular filler is entirely oriented in the undesired transverse direction, α is the "tortuosity" factor that increases the path length from the feed to the permeate side, thereby reducing the flux.

5-2-2 Composite membranes with fillers aligned in the desired orientation

For a membrane with fillers aligned in the desired orientation ($\theta = 0$), Equation 5.6 becomes:

$$J = \frac{\Delta p}{t\left(\frac{1}{P_m}\left(1-\Phi_f\right)+\frac{1}{P_f}\Phi_f\right)} \qquad (5.21)$$

In this case, the flux is independent of the aspect ratio of the filler (α). Fillers with the same permeability and volume fraction would hence provide the same flux regardless of filler geometry. This result may be modified if the surface resistances at the pore entrance/exit are significant in relation to the resistance for transport through the nanotube.

5-3 Predictions of separation properties

5-3-1 Relative permeability effects

The relative permeability (P_f/P_m) effect on the permeability enhancement factor of composite membranes (P_{eff}/P_m) is shown for $P_f/P_m > 1$ and $P_f/P_m \leq 1$ (Figure 5.4a and 5.4b). The tubular fillers are assumed to have $\alpha = 50$ and a random orientation. Equation 5.14 was numerically integrated to obtain the permeability. For $P_f/P_m > 1$, a monotonic increase of P_{eff}/P_m with filler volume fraction (Φ_f) is observed. However, the increase of P_{eff}/P_m becomes insignificant as $P_f/P_m > 100$. In other words, a tubular filler with a permeability much higher than the matrix does not provide a further permeability enhancement since the overall transport rate is now strongly limited by the resistance of the matrix. On the other hand, for $P_f/P_m < 1$, a monotonic decrease of P_{eff}/P_m is observed when increasing the filler volume fraction (Φ_f). A decrease of P_{eff}/P_m is also observed for the case when $P_f/P_m = 1$. This is due to the random orientation of the tubular fillers, which

creates tortuosity in the permeation path. One must be cautioned that when the permeability of the filler is much smaller than that of the matrix, the present resistance-in-series model may no longer be valid since the majority of the molecules may take the faster route through the matrix, which forms the continuous phase in the membrane. Such a concern can be taken into account with the inclusion of a parallel resistance for the continuous phase of the matrix, as addressed in Section 5-1-1. For applications of the composite membranes, a filler of higher permeability than the matrix will typically be used to improve the permeability of the membrane.

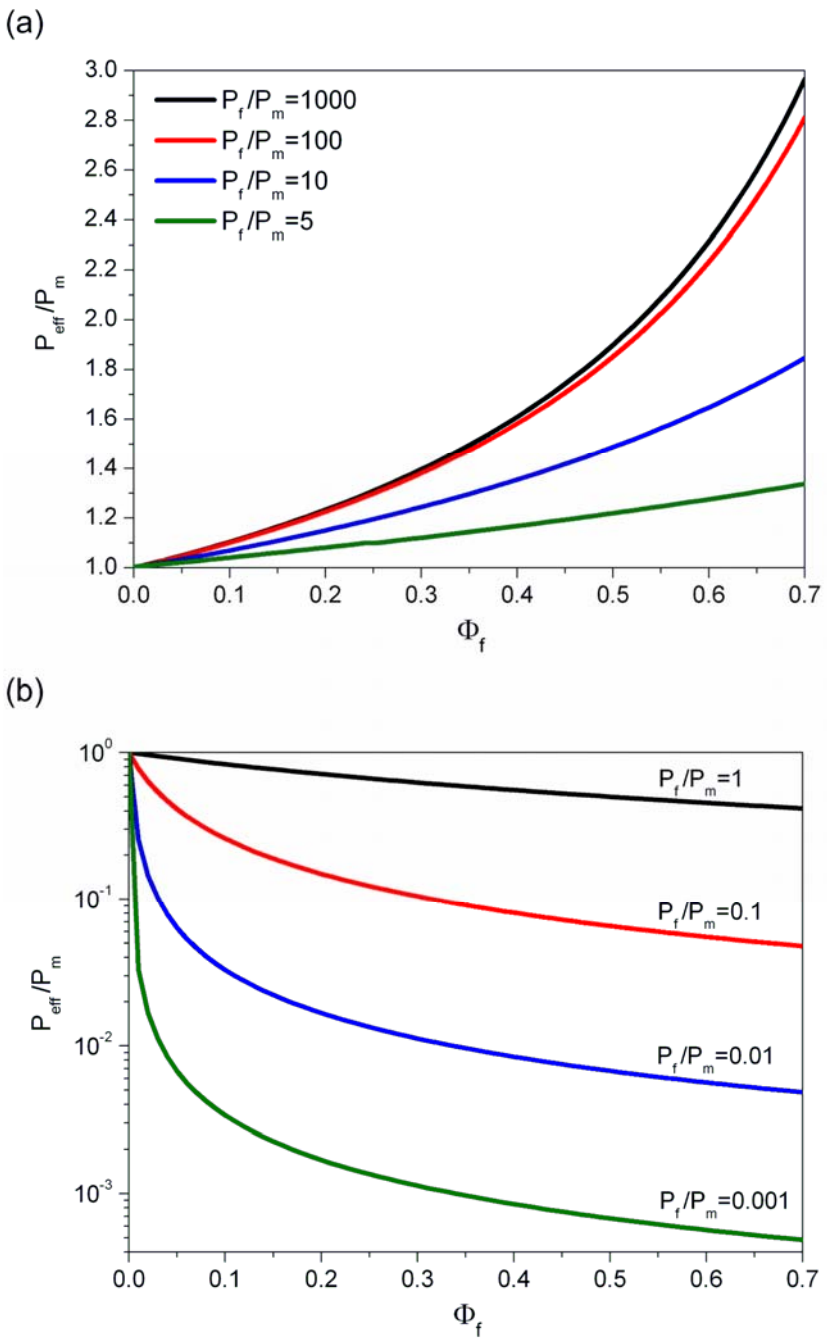

Figure 5.4 Effect of relative permeability (P_f/P_m) on the membrane permeability enhancement factor at different filler volume fractions, when (a) $P_f/P_m > 1$ and (b) $P_f/P_m \leq 1$.

5-3-2 Filler orientation effects

The effect of the filler orientation (θ) is summarized in Figures 5.5a and 5.5b, for P_f/P_m values of 1000 and 10 respectively, and α = 50. For P_f/P_m =1000, P_{eff}/P_m is insensitive to the filler orientation over most orientations, and only creates a significant drop in when the completely undesired orientation ($\theta = \pi/2$) is approached. On the other hand, when the filler permeability is closer to that of the matrix (P_f/P_m =10), the enhancement factor becomes more sensitive to the filler orientation. Based upon the KJN model predictions, it is suggested that the alignment of the tubular fillers in the most desired orientation (θ=0) provides no significant improvement in performance than the randomly oriented configuration. However, the undesired orientation ($\theta = \pi/2$) should be avoided during composite membrane fabricaton. It is also seen that the sensitivity of the permeability enhancement factor (P_{eff}/P_m) to the filler orientation becomes higher when the permeability of the filler is somewhat similar to that of the matrix.

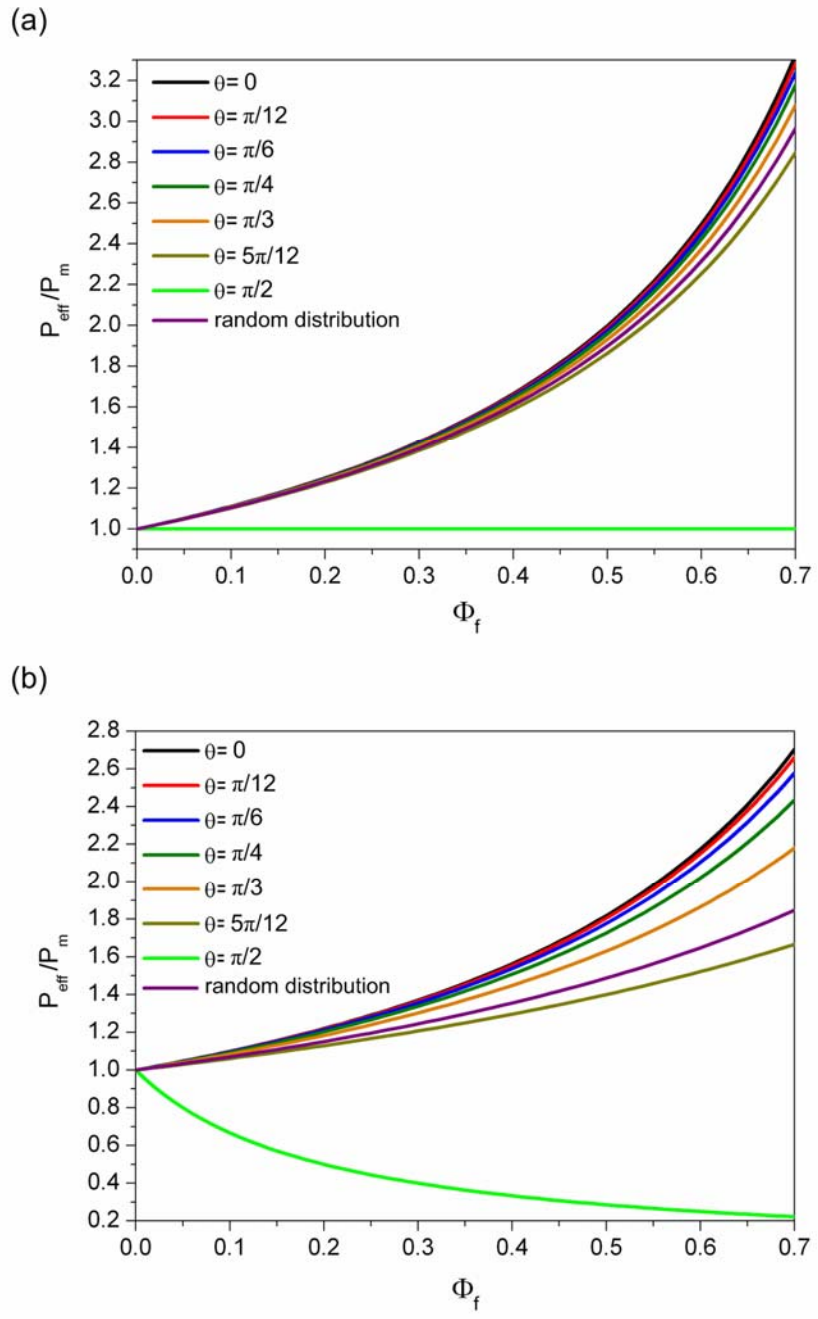

Figure 5.5. Effect of filler orientation effect on permeability enhancement factor at different filler volume fractions, when (a) P_f/P_m =1000 and (b) P_f/P_m =10.

5-3-3 Aspect ratio effects

The effect of the filler aspect ratio (α) when P_f/P_m =1000 is summarized in Figures 5.6a to 5.6c for fillers that at at θ=0^o, randomly oriented, and at θ= π/2, respectively. For the case of fillers aligned in the direction of membrane transport (θ=0), the permeability enhancement is independent of the aspect ratio. As shown in Section 5-2-2, only the filler volume fraction (Φ_f) and the relative permeability (P_f/P_m) affect the effective permeability in this case. On the other hand, randomly oriented fillers with higher aspect ratios (i.e. the longer tubes) enhance the permeability more substantially, since the molecules remain in the more permeable phase for a longer time. However, when the filler is undesirably oriented at $\theta = \pi/2$, fillers with a higher aspect ratio create a longer detour and result in a lower effective permeability. The KJN model may not apply to the case when the fillers are oriented at $\theta = \pi/2$ because a gas molecule would be unlikely to enter the tubular fillers when they are undesirably oriented. For such a case, the transport through the matrix may dominate the effective permeability, and thus the relative permeability (P_f/P_m) would be close to unity.

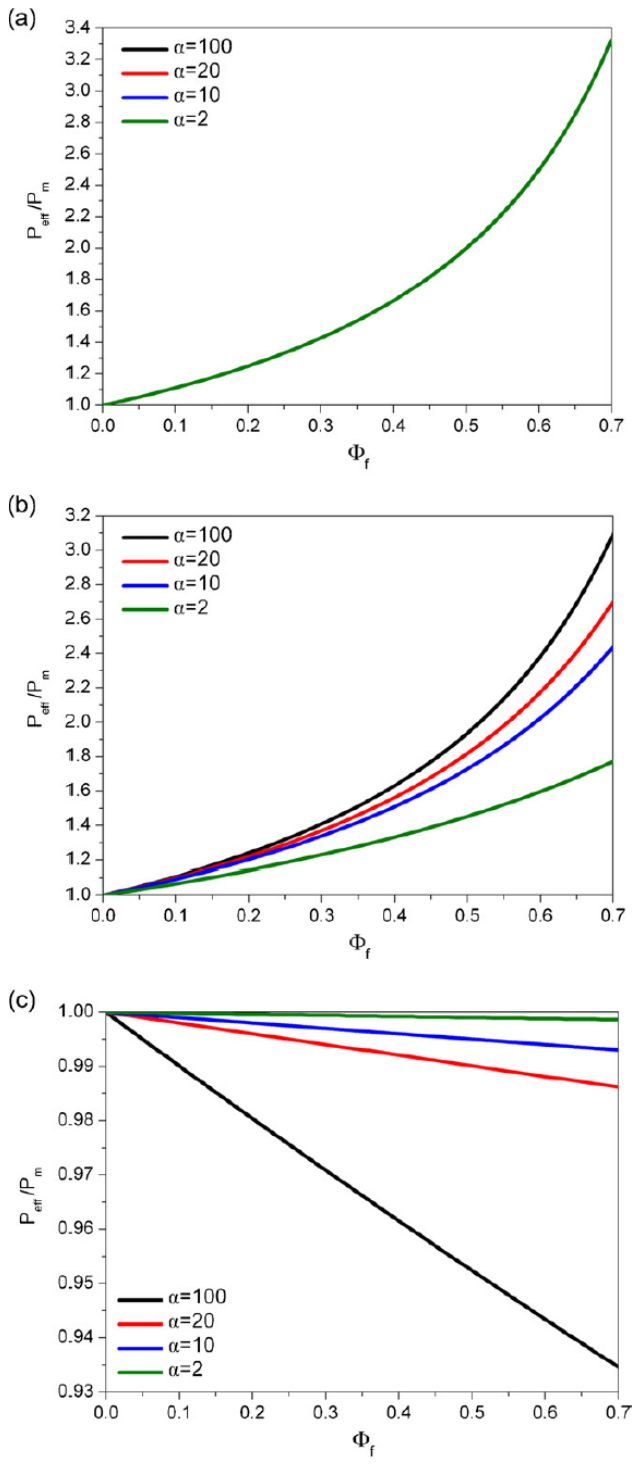

Figure 5.6. Effect of filler aspect ratio on permeability enhancement factor at different filler volume fractions, when fillers are oriented (a) at θ=0, (b) randomly, and (c) at θ=π/2.

5-3-4 Comparisons with current models

The permeability enhancement factor (P_{eff}/P_m) of the KJN model - which is based upon a one-dimensional resistance-in-series transport model of molecules in composite membranes with tubular fillers - is compared with current models for isotropic spherical fillers (Maxwell) and for isotropic tubular fillers (Hamilton-Crosser). The comparisons are made at different values of P_f/P_m for all models; for the KJN model, an aspect ratio of 50 and a random orientation of fillers are considered. The comparison between the KJN model and the isotropic Maxwell model is summarized in Figure 5.7a. At any given relative permeability and filler volume fraction, the enhancement factor estimated by the Maxwell model is consistently higher than that predicted by KJN model. For example, with P_f/P_m =1000 and Φ_f =0.7 the difference of P_{eff}/P_m between the Maxwell and KJN models is as much as a factor of 2.7. The difference of the enhancement factor between KJN and Hamilton-Crosser models is even larger, and is up to a factor of 5 for P_f/P_m =1000 and Φ_f =0.7 (Figure 5.7b). These differences are due to the fundamental dissimilarity of permeation paths in tubular fillers and isotropic fillers. Typical isotropic fillers such as zeolites or metal organic frameworks (MOFs) with three-dimensional interconnected channels allow molecular transport between the filler and the matrix at any point of the interface of the two materials, whereas for tubular fillers the transport between the filler and the matrix can only take place at the tips of the filler. The "accessible surface area" of the fillers, which strongly correlates to their capability of enhancing the permeability for the matrix, can be quantitatively assessed. For the same volume fraction of spherical and tubular fillers, it can easily be shown that the ratio of their total accessible surface areas ($R_{s/t}$) is:

$$R_{s/t} = 3\left(l/D\right) \qquad (5.22)$$

where D is the diameter of a spherical filler. In general, considering the same size of a spherical and a tubular filler (l=D) the isotropic spherical filler has higher accessible surface area in comparison to tubular fillers by a factor of 3 based upon Equation 5.22. The previously discussed fact that a tubular filler has an intrinsically smaller surface area than a spherical filler also supports the observations in Figure 8a, wherein the isotropic spherical filler outperforms the tubular filler in the sense of enhancing the permeability of the matrix. However, the predictions in Figure 5.7a are based on KJN and Maxwell models for tubular and isotropic spherical fillers respectively, and neither of them includes the absolute value of particle size (which can potentially play a role in the effective permeability according to aforementioned discussion). Hence a detailed numerical model, which is beyond the scope of the present paper, will be needed in order to capture the effect of filler particle size.

At this stage, a question naturally arises whether the Maxwell-type models can be re-derived to describe permeation in composite membranes containing tubular fillers. It is seen that while the KJN model passes all of these tests, the Maxwell-type model fails when considering filler orientations that are far from the ideal (θ = 0) orientation. Furthermore, it is more difficult to include the filler orientation in the Maxwell-type model. It can be concluded that the KJN model provides more accurate physical insights and broader applicability, and is a more appropriate model for permeation in membranes with tubular fillers.

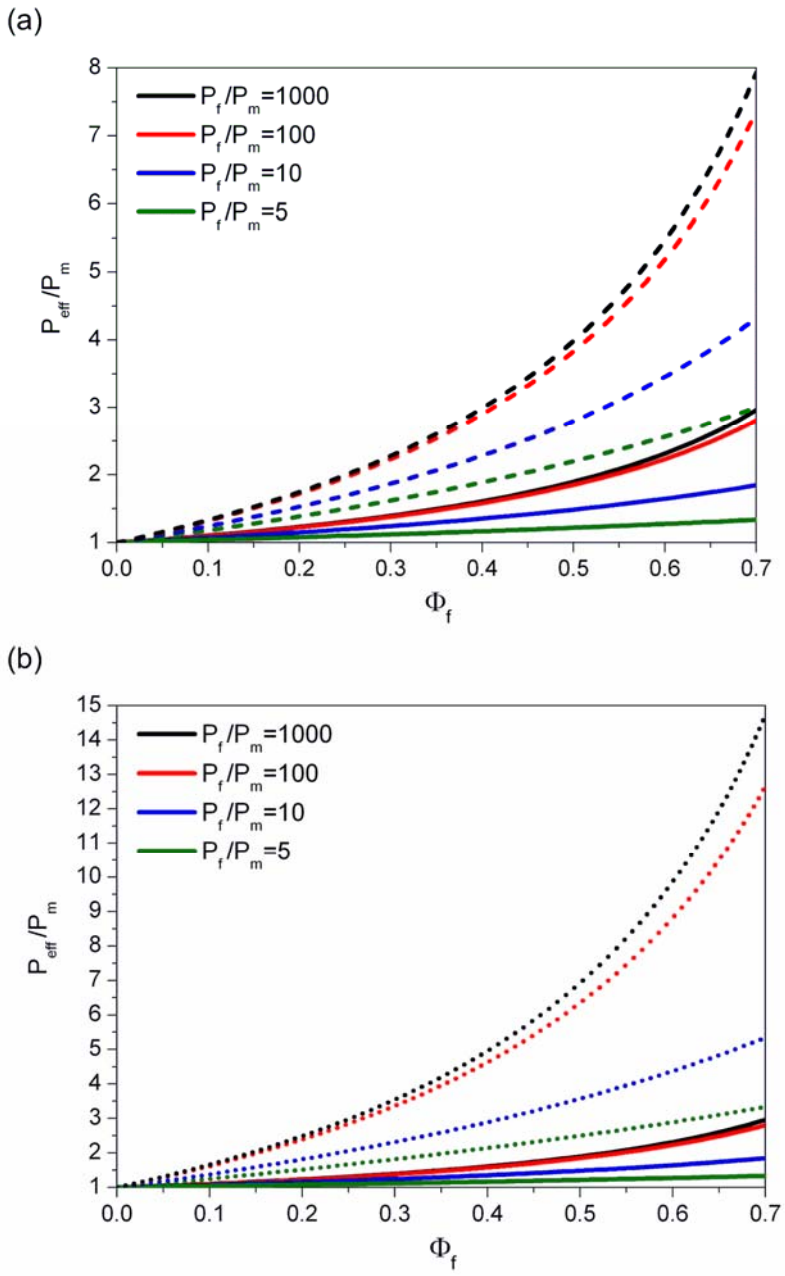

Figure 5.7. Comparisons of present KJN model (solid curves) with (a) Maxwell model (dashed curves) and (b) Hamilton-Crosser model (dotted curves).

5-3-5 Separation factor of binary mixtures

After studying how the incorporation of tubular fillers in composite membranes impacts the effective permeability, the performance of composite membranes with tubular fillers is now explored in binary mixture separations. In addition to the permeability, the selectivity of the membrane ($S_{i/j}$, defined as the ratio of permeabilities of two different types of molecules *i* and *j*) is of high importance. The industrially important separation of carbon dioxide from methane is taken as an example. Two matrix materials are considered: 3,3',4,4'-benzophenonetetracarboxylicdianhydride-4,4'-oxydianilin (BTDA-p,p'ODA), a highly-selective polymer with low permeability;[126] and poly(1-trimethylsilyl-1-propyne) (PTMSP), a low-selectivity polymer with high permeability.[127] For the BTDA matrix, a hypothetical, highly CO_2-permeable ($P_{f,CO2}/P_{m,CO2} >> 1$) tubular filler with no CO_2/CH_4 selectivity is chosen in order to enhance the permeability of the membrane. On the other hand, for the PTMSP matrix, a hypothetical highly CO_2-selective filler is embedded to enhance the selectivity. In both cases, the fillers have $\alpha = 50$ and are randomly oriented. The transport parameters of both the polymers and the hypothetical tubular fillers are summarized in Table 5.1.

Table 5.1. Permeation properties of polymeric membranes, hypothetical tubular fillers, and two types of membrane defects.

Material or Defect	Permeation Property		
	P_{CO2} (Barrer)	P_{CH4} (Barrer)	$S_{CO2/CH4}$ (--)
BDB-p,p'ODA	0.625	0.011	57
PTMSP	18,000	4,190	4.3
Hypothetical low-selectivity tubular filler	--	--	1.0
Hypothetical low-selectivity tubular filler	--	--	30
Void space with average diameter of 5nm	15,200	25,200	0.6
Pinhole with average diameter of 50nm	152,000	252,000	0.6

As shown in Figure 5.8a, for the BTDA matrix with high selectivity ($S_{CO2/CH4}$=57) but low permeability ($P_{m,CO2}$=0.625 Barrer), the incorporation of a highly permeable tubular filler increases the effective permeability of the membrane. Consistent with the results in Section 5-3-1, a higher volume fraction of the filler improves the effective permeability, which however begins to plateau when $P_{f,CO2}/P_{m,CO2}$ >100. At the same time, the membrane selectivity is not dramatically lowered. When the permeability of the filler is close to that of the matrix ($P_{f,CO2}/P_{m,CO2}$ <100), there is an observable drop in selectivity compared to the pure polymeric membrane, since the filler is non-selective ($S_{CO2/CH4}$=1). However, when the filler is much more permeable than the matrix ($P_{f,CO2}/P_{m,CO2}$ >100), the selectivity is dominated by the low-permeability matrix and is maintained at the level of the pure polymer ($S_{CO2/CH4}$=60). Generally, when the filler is less selective than the matrix, a highly permeable filler always benefits the membrane permeability and does not appreciably lower the selectivity. For the matrix with high permeability ($P_{m,CO2}$=18,000 Barrer) but low selectivity ($S_{CO2/CH4}$=4.8), one can reasonably expect an enhancement of overall selectivity by using a highly selective filler ($S_{CO2/CH4}$=30). However, as

summarized in Figure 5.8b, a significant improvement of selectivity is only observed when the selective filler has a lower permeability than the matrix ($P_{f,CO2}/P_{m,CO2}$ <1). At the same time, the enhancement of selectivity sacrifices the effective permeability, resulting in $P_{eff,CO2}/P_{m,CO2}$ <1. However, the model prediction may not be valid when $P_{f,CO2}/P_{m,CO2}$ is much smaller than unity, since gas molecules would mainly transport through the continuous-phase matrix without entering into the relatively impermeable fillers. On the other hand, when the permeability of the selective filler is much larger than that of the matrix ($P_{f,CO2}/P_{m,CO2}$>10), the selectivity shows no improvement. However, for the case of $P_{f,CO2}/P_{m,CO2}$ > 10, the incorporation of filler shows no enhancement in selectivity but an improvement in permeability is observed. In general, when the filler is more selective than the matrix, there is a trade-off between the improvement of selectivity and permeability. A filler that is more selective than the matrix can only improve either the selectivity or the permeability, depending on the relative permeability ($P_{f,CO2}/P_{m,CO2}$). A similar trade-off has also been discovered for composite membranes with isotropic spherical fillers.[128,129]

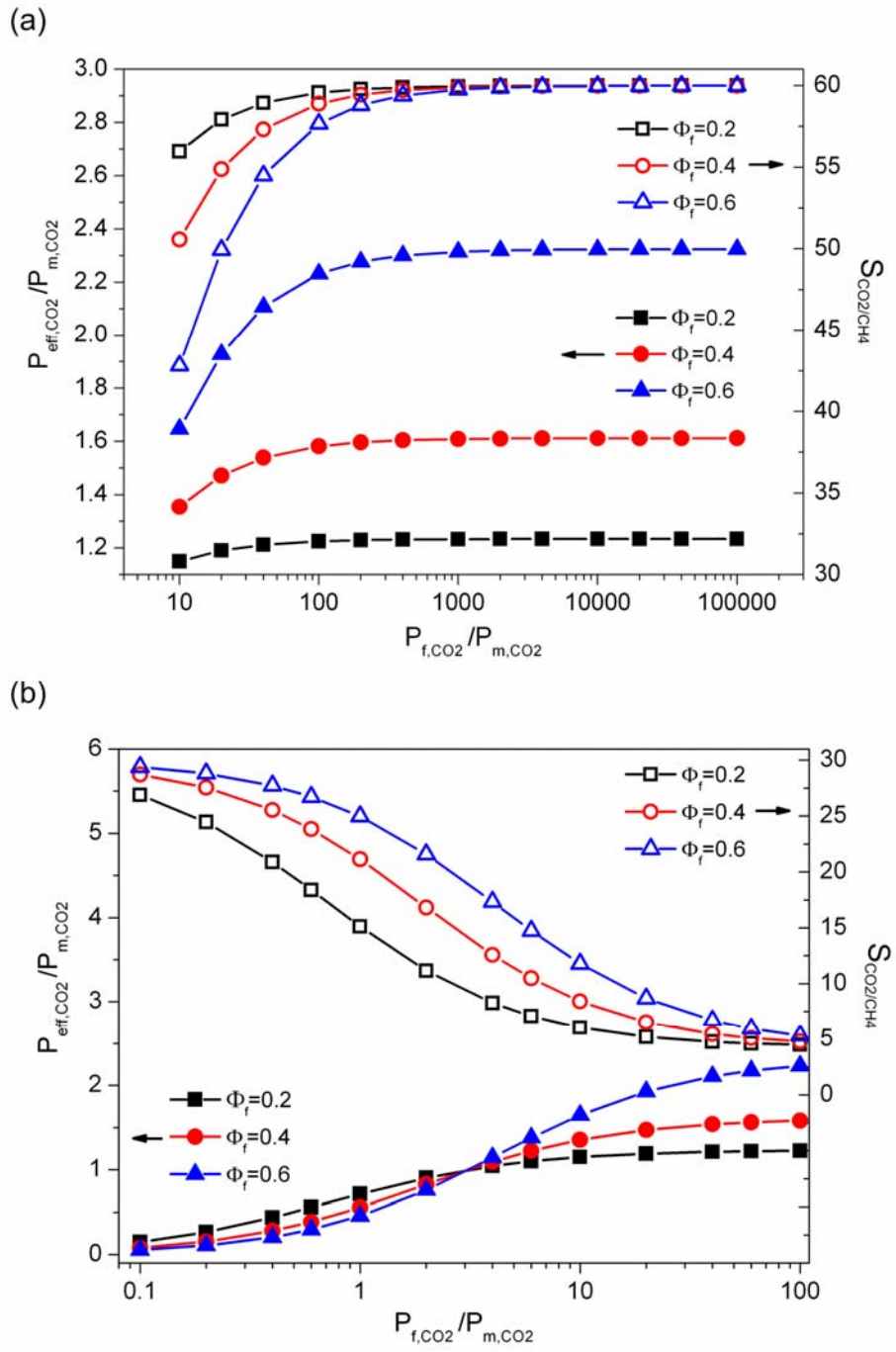

Figure 5.8. Permeability and selectivity of composite membranes with tubular fillers when **(a)** low-selectivity fillers are embedded in a highly selective polymeric matrix, and **(b)** high-selectivity fillers are embedded in a low-selectivity polymer matrix.

5-3-6 Effects of interfacial voids and pinholes

Examples in the previous section are used as a basis for assessing the impact of defects such as interfacial void spaces and pinholes on the membrane performance. To represent typical defects of this nature, average channel sizes of 5 nm and 50 nm are assumed for the interfacial voids and pinholes, respectively. The permeability of the void space and the pinhole at 25^{o}C can be estimated by Equation 5.18, and the results are summarized in Table 5.1. The effect of nanoscale voids surrounding the tubular fillers is summarized in Figure 5.9. In the case of Figure 5.9a, a non-selective tubular filler ($S_{CO2/CH4}$=1) is incorporated to enhance the permeability of the highly-selective ($S_{CO2/CH4}$=57) but low-permeability ($P_{m,CO2}$=0.625 Barrer) matrix. The presence of voids significantly increases the membrane permeability for any given $P_{f,CO2}/P_{m,CO2}$. This is due to several factors, including the high permeability of the void space and its isotropic nature (which intrinsically provides higher permeability than a tubular filler). Furthermore, the presence of voids at low $P_{f,CO2}/P_{m,CO2}$ also improves the selectivity. When the permeability of the tubular filler is close to that of the low-permeability matrix, the highly permeable void space dominates the molecular transport in the region around the filler. The composite membrane now resembles a combination of only the matrix and the void space, which has roughly a five orders-of-magnitude higher permeability than the matrix. Hence, the selectivity is now close to the matrix selectivity of 57, depending on the volume fraction of the void space. On the other hand, the presence of voids in the case of a highly selective tubular fillers ($S_{CO2/CH4}$=30) incorporated in a low-selectivity ($S_{CO2/CH4}$=4.8) but highly permeable matrix ($P_{m,CO2}$=1.80×10^{4} barrer), monotonically improves the effective permeability for reasons similar to those discussed in the previous case. However, the void space significantly lowers the selectivity in comparison to a defect-free composite membrane, by allowing molecules to bypass the highly selective tubular filler. An interesting phenomenon in Figure 5.9b is the maximum in the membrane selectivity with respect to the relative permeability $P_{f,CO2}/P_{m,CO2}$. At low

$P_{f,CO2}/P_{m,CO2}$, the highly permeable void space dominates the molecular transport rate in the region of the void space/filler. The selectivity of the composite membrane is then dominated by the matrix. On the other hand, at high $P_{f,CO2}/P_{m,CO2}$, the permeability of the tubular filler is higher than that of the void space. Hence, the filler dominates the transport in the region of the void space/filler, since the mass transport in the void space around the filler can be modeled by the resistances of the void space and the filler in parallel (Figure 5.3). Similar to the findings of Section 5-3-5, the overall selectivity of the composite membrane is now determined by the relatively low-permeability matrix. In general, interfacial voids can enhance both selectivity and permeability when fillers are incorporated to enhance permeability of a highly-selective matrix; but their presence does not benefit the case wherein fillers are embedded to improve the selectivity of a highly permeable matrix.

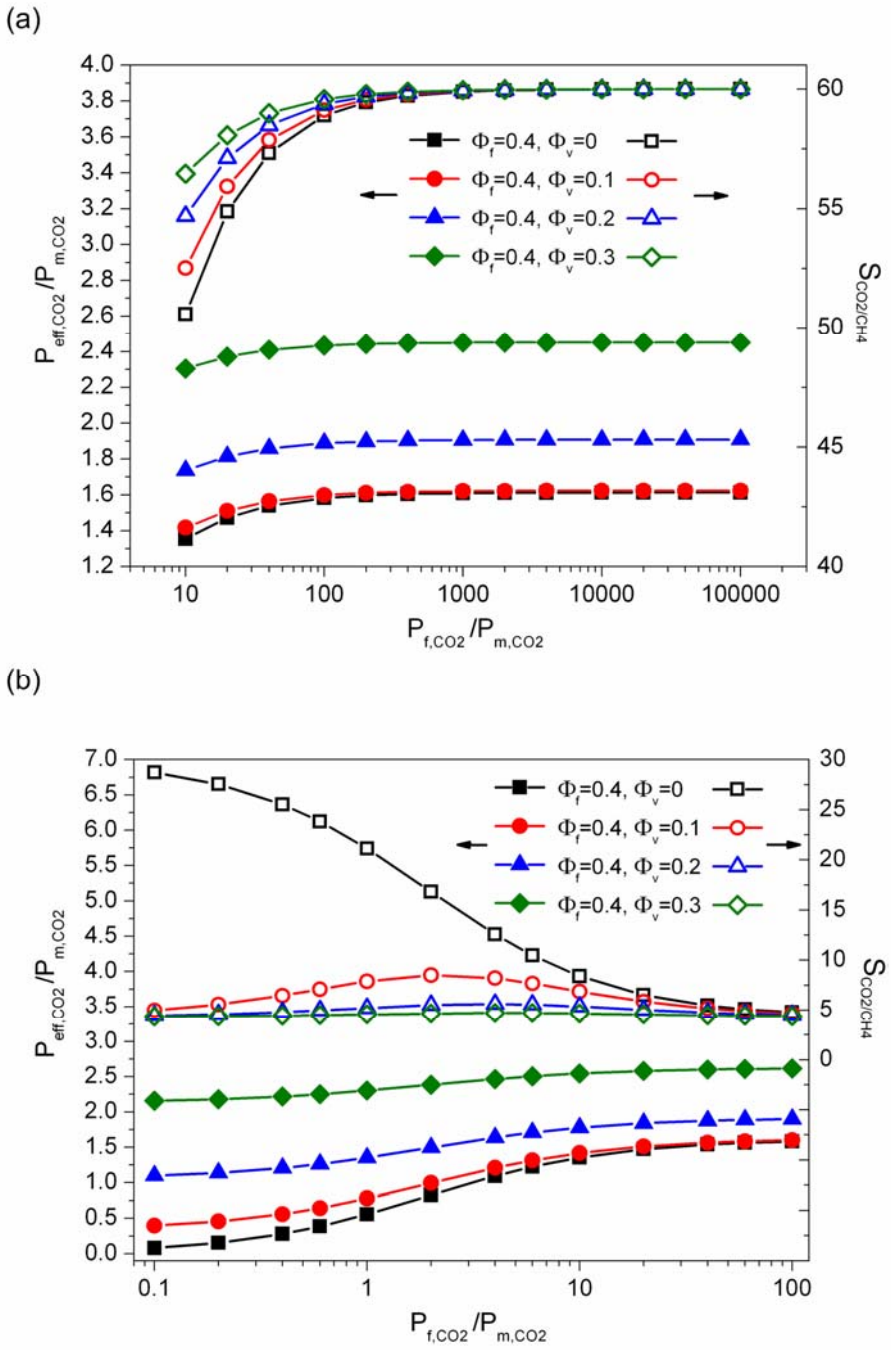

Figure 5.9. Effects of interfacial void spaces on permeability and selectivity of composite membranes containing tubular fillers, when (a) low-selectivity fillers are embedded in a high-selectivity polymeric matrix, and (b) high-selectivity fillers are embedded in a low-selectivity polymeric matrix.

The effect of pinholes on the membrane performance is evaluated in Figure 5.10. In analogy to the void spaces, the case of highly permeable but non-selective ($S_{CO2/CH4}$=1) fillers incorporated to improve the permeability of a highly selective ($S_{CO2/CH4}$=57) but low-permeability ($P_{m,CO2}$=0.625 Barrer) matrix is considered in Figure 5.10a. Even a trace volume of pinholes causes a dramatic increase of permeability, and also greatly reduces the high selectivity that would normally be derived from the matrix, lowering it to that of the pinhole ($S_{CO2/CH4}$=0.6). These phenomena clearly occur because the pinhole provides a low-selectivity but high-permeability channel for molecules to bypass the membrane from the feed side to the permeate side. In comparison, the void spaces only allow molecules to bypass the filler but not the matrix, since the voids are embedded in the matrix as a discrete phase. For the case of highly selective fillers ($S_{CO2/CH4}$=30) embedded in a permeable but low-selectivity matrix, the presence of pinholes monotonically increases the effective permeability as the volume fraction of the pinhole increases (Figure 5.10b). However, even a trace volume of pinholes (Φ_p=10^{-2}) leads to a complete loss of selectivity of the membrane, and hence pinholes should obviously be avoided during membrane fabrication. There also exists a maximum in selectivity with respect to $P_{f,CO2}/P_{m,CO2}$, for reasons similar to the case of voids.

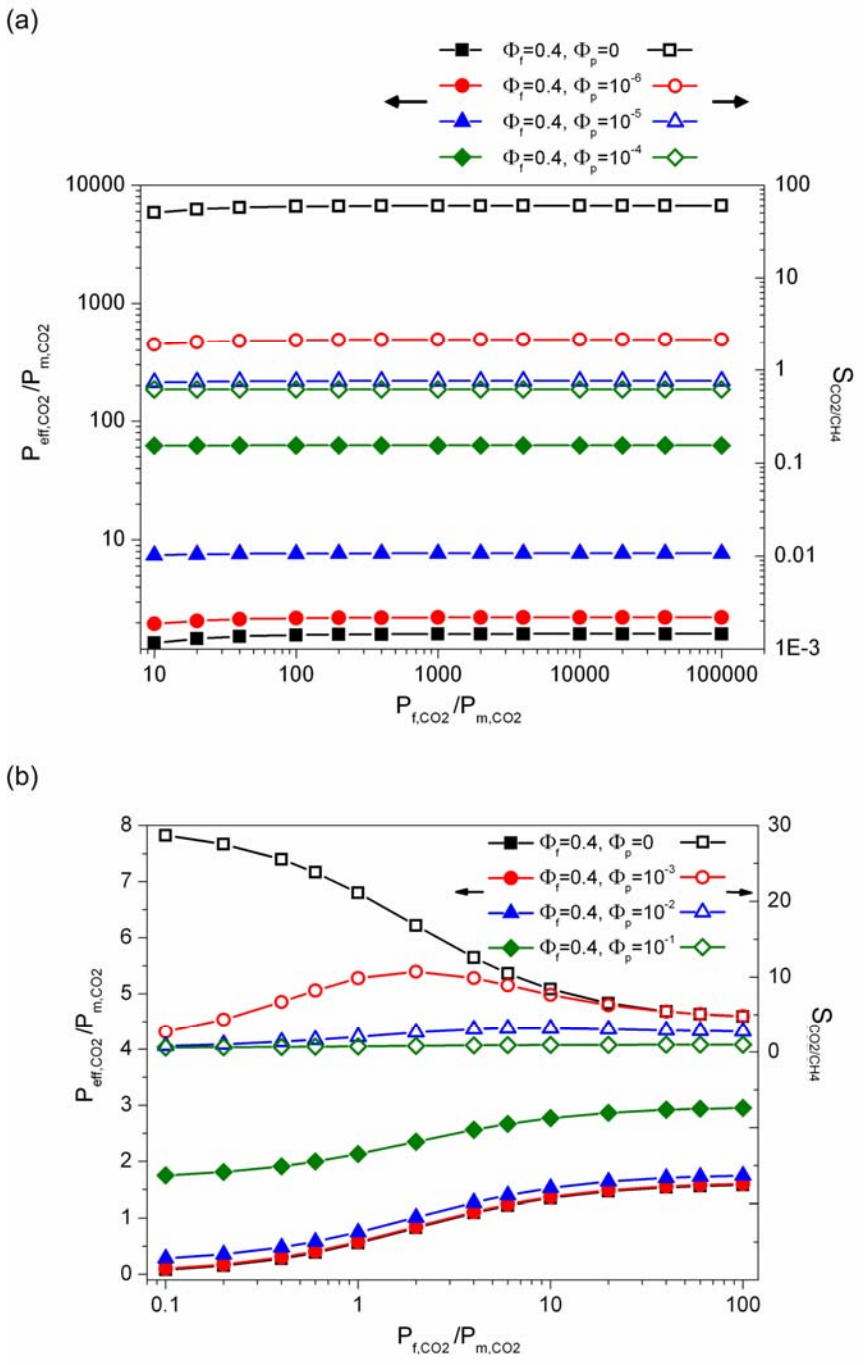

Figure 5.10 Effects of pinholes on permeability and selectivity of composite membranes with tubular fillers when (a) a high-selectivity polymeric matrix containing low-selectivity fillers, and (b) a low-selectivity polymeric matrix containing high-selectivity fillers.

5-3-7 Filler effects on cellulose acetate membranes for CO_2/CH_4 separation

Cellulose acetate is one of the state-of-the-art polymers for natural gas separation, due to its good selectivity ($S_{CO2/CH4}$ up to 25) and robustness.[130,131] However, the efficiency of current cellulose acetate-based natural gas separation membranes is limited by its low permeability ($P_{m,CO2}$=3 Barrer). Figures 5.11a to 5.11c summarize the tubular filler effect for different filler permeabilities, selectivities, and volume fractions. For a non-selective filler ($S_{CO2/CH4}$=1) (Figure 5.11a) of much higher permeability than the matrix (e.g., $P_{f,CO2}$ > 300 Barrer), the effective permeability of the resulting composite membrane is more enhanced and the high selectivity from the matrix is being preserved, in comparison to fillers with low permeability ($P_{f,CO2}$ < 30 Barrer). On the other hand, when a somewhat selective tubular filler is used ($S_{CO2/CH4}$=10) (Figure 5.11b), the composite membrane selectivity becomes closer to that of the pure cellulose acetate membrane if the filler permeability is low ($P_{f,CO2}$ < 30 Barrer). If highly selective tubular fillers (e.g., $S_{CO2/CH4}$ =50) (Figure 5.11c) are prepared and embedded into the cellulose acetate matrix, the enhancement of the selectivity is only observed when the permeability of the fillers is close to the matrix permeability, i.e., the two phases are "well matched". No significant selectivity improvement is observed when the permeability of the tubular fillers is much higher than that of the matrix, and this observation supports the discussion in Section 5-3-5. Comparisons of spherical isotropic fillers, whose effective permeabilities are estimated by the Maxwell model, with the same intrinsic permeability and selectivity are summarized in Figures 5.11d to 5.11f. When the filler selectivity is lower than that of the matrix (Figures 5.11d and 5.11e), spherical fillers can better enhance the permeability but lead to a greater loss in selectivity, in comparison to tubular fillers. On the other hand, when the fillers have higher selectivity (Figure 5.11f) than the matrix, spherical fillers show a more significant enhancement of both permeability and selectivity than tubular fillers. This observation agrees with the results of Section 5-3-4,

in that isotropic fillers can more efficiently improve the effective permeability of composite membranes than anisotropic tubular fillers.

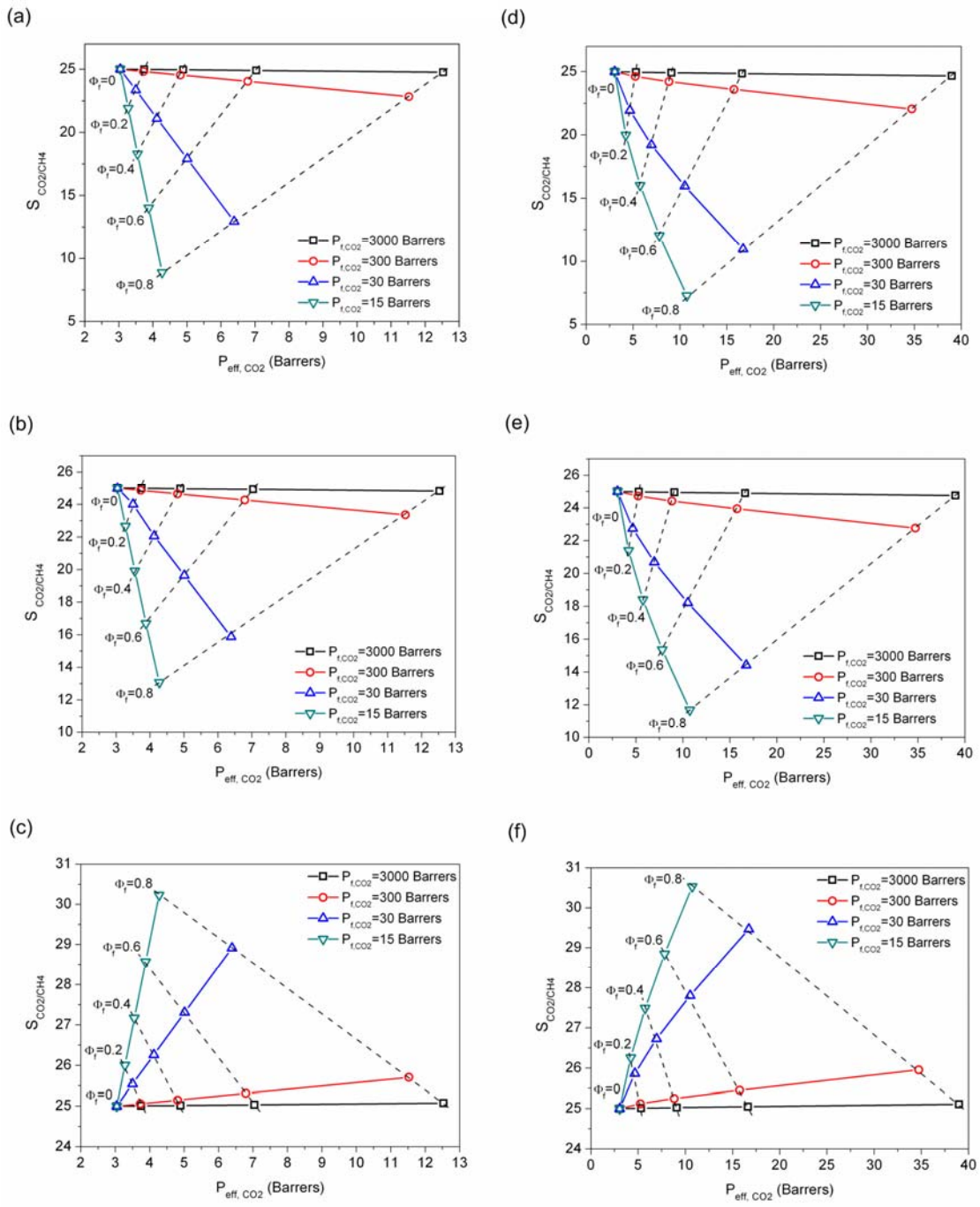

Figure 5.11. Effects of fillers on permeability and selectivity of composite membranes with Cellulose Acetate as a matrix. (a)-(c) show predictions of the KJN model for tubular fillers with selectivities of 1, 10, and 50 respectively; whereas (d)-(f) show predictions of the Maxwell model with filler selectivity of 1, 10, and 50 respectively.

5-3-8 Advanced configuration of composite membranes with tubular fillers

In Sections 5-3-4 and 5-3-7, it was demonstrated that spherical isotropic fillers generally enhance the permeability of composite membranes to a greater extent than tubular fillers. However, the focus was on membranes whose thickness is much larger than the individual filler length. The fillers do not provide "direct" channels for molecules from the feed to the permeate side, and the effective permeability is thus limited by the matrix. Hence, although previous studies have shown that nanotubes possess superior transport properties, they cannot be exploited fully by conventional composite membranes. On the other hand, a composite membrane has been conceived in which all the fillers span the membrane thickness and serve as direct channels from the feed to permeate side for molecules. Such a membrane may be quite thin (<1 μm). Transport in this membrane can be modeled by two resistances in parallel, and the effective permeability can be written as:

$$P_{eff} = \left(1 - \Phi_f\right) P_m + \Phi_f P_f \qquad (5.23)$$

The permeability and selectivity of "conventional" and "advanced" composite membranes with tubular fillers are compared in Figures 5.12a and 5.12b, with parameters from Section 5-3-7. The advanced membrane shows substantially higher permeability, since transport is no longer limited by the matrix. For tubular fillers with lower selectivity than the matrix, the advanced membrane does not preserve the high matrix selectivity (Figure 5.12a) as efficiently as the conventional membrane because the highly permeable tubular fillers dominate the mass transport in the "advanced" composite membranes. As a consequence, when the fillers have high selectivity and permeability, large performance enhancements can be realized as long as the fillers possess both good permeability and good selectivity (e.g., the red solid circle in Figure 5-.12b).

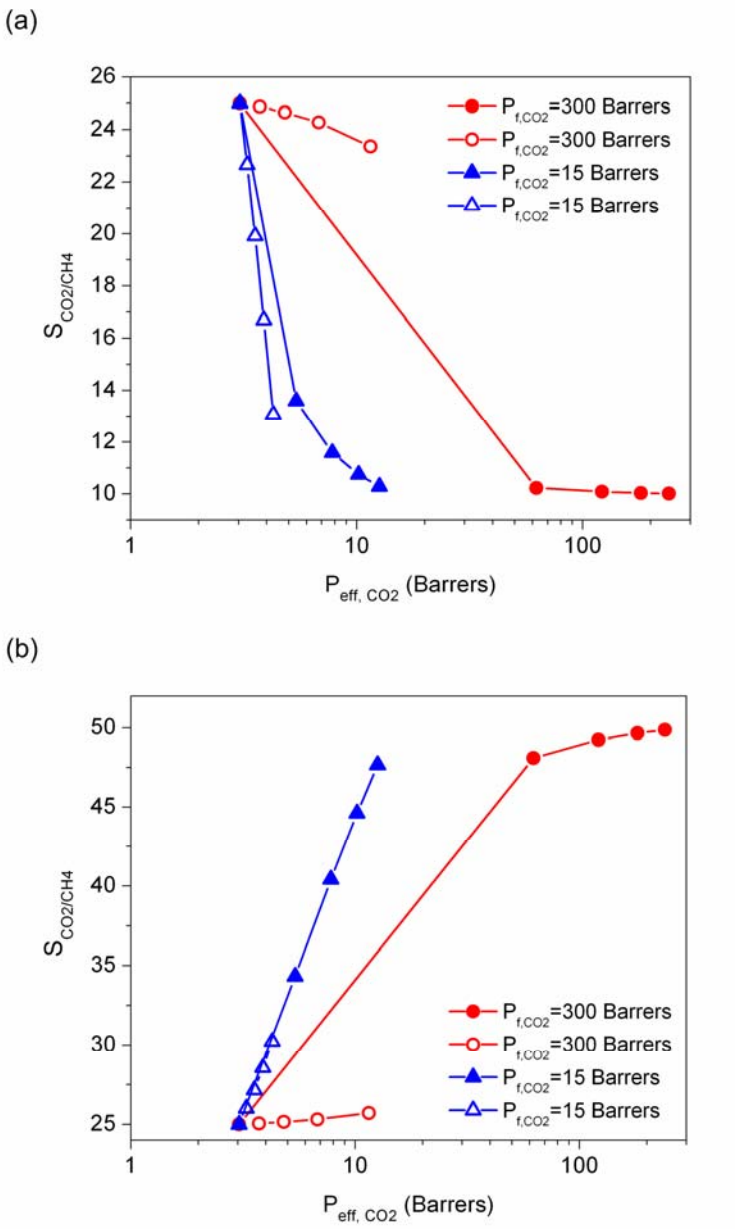

Figure 5.12. Effects of tubular fillers on the permeability and selectivity of cellulose acetate, for filler selectivities of (a) 10 and (b) 50. The open symbols represent the conventional composite membranes, and the solid symbols represent thin membranes with tubular fillers spanning the thickness. In these plots, the filler volume fraction (Φ_f) *is the independent variable.* For each curve, the five data points (from left to right) represent Φ_f=0, 0.2, 0.4, 0.6, 0.8, respectively.

5-4 Summary

An analytical model has been developed for describing molecular transport in composite membranes with tubular fillers. It includes the key microstructural parameters, namely the filler volume fraction (Φ_f), filler aspect ratio (α), an arbitrary filler orientation distribution function ($f(\theta)$), the permeability ratio of the filler and the matrix (P_f/P_m), and the presence of voids and pinholes. The model is first validated for several limiting cases, and then used to predict the permeability and selectivity of several composite membranes containing tubular fillers with a range of properties and embedded in different polymers. A number of general conclusions can be drawn from the predictions. First, a high filler volume fraction (Φ_f) always benefits the membrane permeability. Second, a relative permeability (P_f/P_m) larger than unity can improve membrane permeability, but little further enhancement occurs after P_f/P_m >100. Third, a composite membrane with randomly oriented fillers provides practically equal performance to membrane in which the fillers are aligned in the desired orientation (θ=0). However, a membrane with fillers aligned at the undesired orientation (θ=π/2) has a dramatically lower permeability. Fourth, the aspect ratio (α) does not impact the permeability of a membrane with fillers aligned at the desired orientation. For a membrane with randomly oriented fillers, a high aspect ratio is preferred since it provides a higher effective permeability. Fifth, the current models for isotropic fillers (Maxwell and Hamilton-Crosser) strongly deviate from the predictions of the present KJN model, since they do not account for the highly anisotropic transport in the tubular filler.

The performance of membranes containing tubular fillers in mixture separations was explored, and several conclusions were reached. Non-selective but highly permeable fillers in a selective but low-permeability matrix can enhance membrane permeability and maintain selectivity. Highly selective fillers in a permeable but low-selectivity matrix can enhance selectivity only when $P_f/P_m \leq 1$, whereas a highly selective filler possessing high

permeability can only enhance the effective permeability. Additionally, void spaces or pinholes prevent selectivity improvement even when $P_f/P_m \leq 1$. The membrane performance is more sensitive to the presence of pinholes, which cause a precipitous decrease in selectivity. Furthermore, case studies were performed to understand how tubular and spherical isotropic fillers affect the performance of state-of-the-art polymeric membranes. For conventional composite membranes of much larger thickness than the filler dimensions, the tubular filler must have far superior intrinsic transport properties than spherical fillers in order to obtain the same performance enhancement. On the other hand, the fabrication of advanced composite membranes with selective tubular fillers spanning the membrane thickness is seen to be highly advantageous.

5-5 Nomenclature of Chapter 5

D	diameter of a spherical filler
D_{Kn}	Knudsen diffusivity
d	outer diameter of a tubular filler
α	aspect ratio of a tubular filler defined as l/d
$f(\theta)$	fraction of fillers oriented at θ amongst all fillers present in the same composite membrane
$g(\theta)$	orientation distribution function of fillers in a composite membrane
J	molecular flux of permeation
l	length of a tubular filler
M	molecular weight of transported species
n	shape factor in the Maxwell model
n_f	number of fillers along the molecular path in a membrane from feed to permeate side
P_{eff}	effective permeability of a membrane
$P_{eff,\,\theta}$	effective permeability of a sub-domain of a membrane composed of only fillers oriented at θ
P_{eff}/P_m	permeability enhancement factor of a composite membrane in comparison to a membrane
	only made of matrix material
P_f	permeability of a filler
P_m	permeability of a matrix
P_p	permeability of a pinhole
P_v	permeability of a void space
r	radius of spherical filler
R	gas constant

$R_{s/t}$ ratio of accessible surface area for mass transport between the spherical and tubular filler with the same volume.

S_{IG} solubility coefficient in the void space or in the pinhole based upon ideal gas law

T temperature

t thickness of a membrane

t_f the transport path length through fillers in a composite membrane, assuming an average number of the fillers for each path

$t_{f,nf}$ the transport path length through fillers in a composite membrane for n_f fillers on the path

t_m the average transport path length through the matrix in a composite membrane, assuming an average number of the fillers for each path

$t_{m,nf}$ the average transport path length through the matrix in a composite membrane for n_f fillers on the path

t_θ thickness of a sub-domain in a membrane composed of fillers oriented at tilt angle θ

Δp pressure difference on the feed and permeate side of the membrane

$S_{i/j}$ selectivity of species i over j, defined as the ratio between their permeabilities

Φ_f volume fraction of fillers in a composite membrane

Φ_m volume fraction of the matrix in a composite membrane

Φ_p volume fraction of pinholes in a composite membrane

Φ_v volume fraction of the void space surrounding the fillers in a composite

	membrane
θ	tilt angle with respect to the bulk permeation direction of a filler in a matrix

CHAPTER 6

FREE-STANDING ALUMINOSILICATE NANOTUBE/POLY(VINYL ALCOHOL) NANOCOMPOSITE MEMBRANES

In this chapter, the preparation, characterization, and permeation properties of polymer/SWNT composite membranes with high loading and near-ideal dispersion of nanotubes is reported. Specifically, the loading of well-dispersed SWNTs in poly(vinyl alcohol) (PVA) membranes is systematically increased up to 38% by volume and the properties of the nanotubes are assessed. The importance of initial dispersion of the SWNTs in a liquid medium is highlighted by comparison of membranes fabricated using SWNT gels and SWNT powders as starting materials. The microstructure of the composite membranes is assessed qualitatively and quantitatively by scanning electron microscopy (SEM), energy dispersive spectroscopy (EDS), 2D X-ray diffraction (XRD), small-angle X-ray scattering (SAXS) and solid-state NMR. Subsequently, the permeation properties of the PVA/SWNT composite membranes are studied by water/ethanol pervaporation measurements, and the results are analyzed in terms of developed models in Chapter 5 as well as with predictions from molecular simulation studies.

6-1 Experimental details

6-1-1 Preparation of aluminosilicate SWNT/PVA composite membranes with SWNT powders

The SWNT powder sample was weighed and mixed with 30 mL of PVA aqueous solution at room temperature. The total mass of SWNT and PVA was 400 mg and the mass fractions of SWNT were controlled at 0.1, 0.2, 0.3, and 0.4 respectively. The resulting PVA/SWNT mixture was gently stirred for 18 hours at room temperature. The mixture was then poured into a poly(styrene) petri dish and the membrane was cast at 60

^{o}C for 24 hours. The resulting composite membrane was removed from the petri dish and placed in a crosslinking bath containing 50 mL of water, 50 mL of acetone, 0.5 g of 98 wt% sulfuric acid, and 1.25 g of 25 wt% glutaraldehyde for 30 minutes. The crosslinked membrane was washed with ethanol and then dried at 60 ^{o}C for 24 hours. The SWNT volume fractions of the resulting membranes were determined from the mass fractions and densities of SWNTs and PVA. Membranes with SWNT volume fractions of 0.11, 0.21, 0.31, and 0.42 are referred to as pwd-1, pwd-2, pwd-3, pwd-4, respectively in the following discussion. These membranes have thicknesses in the range of 40-100 μm, as determined by a screw gauge as well as cross-sectional SEM images.

6-1-2 Preparation of aluminosilicate SWNT/PVA composite membranes with SWNT gel

SWNT gels (8 mL, 16 mL, 24 mL, and 32 mL) were mixed at room temperature with 20 mL of PVA aqueous solutions containing 360 mg, 320 mg, 280 mg, and 240 mg of PVA respectively. The PVA/SWNT composite membranes were then cast and crosslinked by the same procedures mentioned in the previous section. The SWNT mass fractions in the resulting PVA/SWNT membranes were determined by thermogravimetric analysis (Supporting Information). The SWNT volume fractions were determined as mentioned in the previous section. Membranes with SWNT volume fractions of 0.08, 0.20, 0.33, and 0.38 are referred as gel-1, gel-2, gel-3, and gel-4 respectively in the following discussion. These membranes have thicknesses in the range of 40-100 μm, as determined by a screw gauge as well as cross-sectional SEM images.

6-1-3 Scanning Electron microscopy (SEM) and energy dispersive spectroscopy (EDS)

The morphology of SWNT/PVA composite membranes was imaged with a scanning electron microscope (SEM, Hitachi S-3700N). To observe the cross-sectional morphology, the membranes were cryogenically fractured in liquid N_2. Energy dispersive spectroscopy (EDS) analysis of the cross-sections was carried out with the same instrument.

6-1-4 XRD measurements and simulations

X-ray diffraction (XRD) scans in Bragg-Brentano geometry were performed on a PAnalytical X'pert Pro MPD diffractometer operating with a Cu Kα source. Diffraction data were collected with a collimator and Miniprop detector, in the range of 3-30^o 2θ and a step size of 0.05^o. Grazing-angle XRD scans were performed on PAnalytical X'pert Pro MRD diffractometer operating with a Cu Kα source. XRD simulations were performed to investigate the extent of SWNT bundling. The Reflex module of the Materials Studio 3.2 molecular simulation package (Accelrys, Inc.) was used, and the details of such simulations have been reported in Chapter 2.

6-1-5 SAXS measurements and simulations

Small angle X-ray scattering (SAXS) on the prepared membranes were performed on the DND-CAT beamline at the Advanced Photon Source (Argonne National Laboratory). The beamline was tuned to operate at 17 keV, resulting in an X-ray wavelength of 0.73 Å. The beam at the sample position was controlled to have dimensions of a few hundred microns. The SAXS patterns of SWNT/PVA composite membranes were simulated as described in the Results and Discussion section, and key structural parameters were obtained by fitting the model predictions to the measured data.

6-1-6 Pervaporation

The composite membranes were used for pervaporation of an ethanol/water mixture. The feed solution was 80 wt% ethanol. The measurements were performed at 60

^{o}C, wth a feed and permeate pressure of 101 kPa and 0.5 kPa, respectively. Two cold traps at 77 K were used to collect the permeate. After 2 hours of permeation, the cold traps were weighed in order to obtain the total permeate mass flow rate. The total mass flux was determined by dividing the mass flow rate by the membrane area (18.8 cm^2). The permeate composition was measured by a gas chromatograph (GC). The water and ethanol molar fluxes (J) thus obtained were converted into water and ethanol permeability by the relation $J = P_{eff}(\Delta p / t)$, where P_{eff} is the effective permeability of the membrane for the transported molecules, t is the thickness of the membrane, and Δp is the vapor pressure difference of the transported molecules between the feed side and the permeate side. The membrane thicknesses were measured by a spring thickness gauge. In order to obtain Δp, the vapor pressures of water and ethanol on the feed side and on the permeate side were determined separately. The water or ethanol vapor pressures on the feed side were taken as the product of its liquid phase mole fraction, its saturated vapor pressure, and its activity coefficient for the mixture. The liquid phase mole fraction was measured by GC. The saturated vapor pressures and the activity coefficient were estimated by the Antoine equation and the UNIFAC model respectively. The water or ethanol vapor pressures on the permeate side were the product of the measured pressure on the permeate side and its mole fraction on the permeate side measured by GC.

6-1-7 Molecular adsorption and diffusion simulations

The construction and the structural optimization of SWNT atomic models are described in Chapter 2. Adsorption isotherms were calculated at 333 K for water and ethanol as single-components using the Grand Canonical Monte Carlo (GCMC) method as implemented in the MUSIC simulation code, with the molecules only allowed to be inserted within the NT pore. The CLAYFF force field for NTs, the SPC model for water, and the TraPPE force field for ethanol were used as explained in previous work. The flexibility of hydroxyl groups was considered as described previously,[46] with all atoms in

the NTs being fixed in position except for the surface hydroxyl groups. To examine the diffusion of water and ethanol in NTs, NVT molecular dynamics (MD) simulations at 333 K were performed using a Nosé-Hoover thermostat. Unlike GCMC calculations, all atoms in the NTs were allowed to move in the MD calculations. After equilibrating the system for 0.4 ns, MD simulations were run for 2 ns with a time step of 1 fs. The corrected diffusivities (D_0) thatdescribe the diffusive motion of the center-of-mass of the molecules relative to the reference frame of the adsorbent were calculated by averaging data over 30 independent trajectories for water and ethanol loadings ranging from near-zero to near-saturation loading. Transport diffusivities (D_t) that describe the macroscopic diffusive transport under the influence of a concentration gradient were then calculated from D_0 and the thermodynamic correction factor: $D_t = D_0 \partial \ln f / \partial \ln C$. Here, f is the fugacity of the bulk gas phase in equilibrium with the concentration C of the species in the adsorbed phase. The thermodynamic correction factor $\partial \ln f / \partial \ln C$ was obtained from the computed adsorption isotherms by assuming fugacity and pressure to be equal in the pressure range considered in this study. The permeability (P) at a given pressure (p) is taken as $P = D_t(C)C/p$, where C is the concentration of species in the adsorbed phase at the given pressure. The permeability information for the pressure range of the pervaporation experiments (p=101kPa for the feed side and p=0.5kPa for the permeate side) was thus obtained.

6-1-8 Solid-state NMR

^{1}H and $^{1}H \rightarrow {}^{13}C$ cross-polarization (CP) solid-state NMR measurements were performed on a Bruker DSX 400 spectrometer operating at resonance frequencies of 399.8 MHz for ^{1}H and 100.5 MHz for ^{13}C. The membranes were cut into small pieces and packed tightly into a 4 mm rotor. The rotor was spun at frequency of 10 kHz during

the measurements. A $\pi/2$ pulse and 4 s repetition time were applied for both ^{1}H and ^{13}C measurements. Chemical shifts of the ^{1}H and ^{13}C spectra were referenced to adamantane.

6-2 Uniformity of the PVA/SWNT composite membranes

Photographs of the aqueous PVA/SWNT solutions and PVA/SWNT membranes prepared by the two different starting materials (SWNT gels and SWNT powders) are summarized in Figure 6.1. The pure PVA solution and the solution used for preparing the gel-4 membrane both show high transparency in comparison to the PVA/SWNT solution used for preparing the pwd-4 membrane (Figure 6.1a). This suggests that any aggregates/bundles of nanotubes in the sample are smaller than the smallest wavelength of visible light (~ 390 nm). On the other hand, suspended particles can be visually observed in the pwd-4 solution, which implies that the SWNT particles do not completely re-disperse into individual SWNTs in a pure aqueous solution with no pH adjustment. As seen from Figure 6.1b, the membrane made from the gel-4 solution shows transparency similar to pure PVA membranes, thereby indicating no severe phase separation during membrane formation and good dispersion of the SWNTs in the solid phase. In contrast, the low transparency of the pwd-4 membrane implies the aggregation of SWNT particles in the membrane.

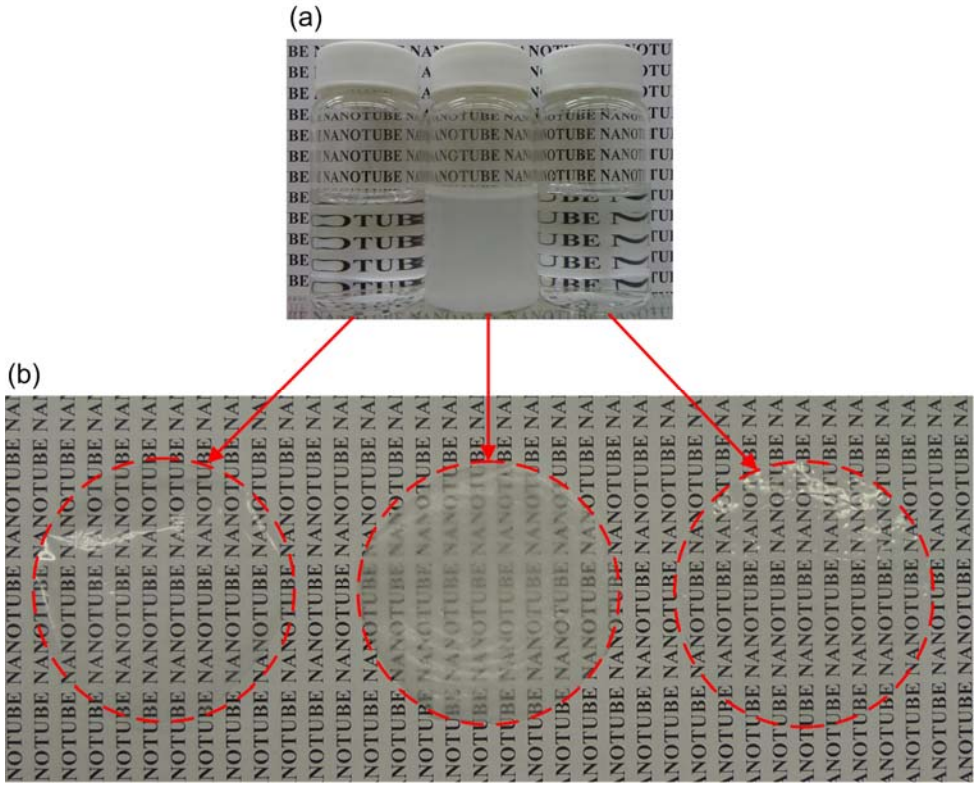

Figure 6.1 Photographs of (a) aqueous solutions (or dispersions) of pure PVA, SWNT powder, and SWNT gel from left to right; (b) a pure PVA membrane, a powder-derived ~40 vol % SWNT/PVA membrane, and a gel-derived ~40 vol % SWNT/PVA membrane, from left to right. The red circles locate the membranes of 3" diameter.

Figure 6.2 shows cross-sectional SEM images and EDS line profiles of the silicon-to-carbon intensity ratio for membranes prepared from SWNT powder (pwd-4) and SWNT gel (gel-4). Similar results are obtained for the remaining membranes in the sample set, and are shown in the Supporting Information. The pwd-4 membrane (Figure 6.2a) displays the existence of large SWNT agglomerations that have a high silicon-to-carbon intensity ratio in EDS. However, although the SWNT aggregates do not completely dissociate during membrane formation, the absence of micron-scale voids between the SWNTs and the PVA matrix suggests good adhesion properties between the two materials. This is likely due to the interaction of the hydroxyl groups of PVA with the bridging hydroxyl groups on the outer surface of the SWNTs. Membranes prepared with SWNT gels exhibit a homogeneous appearance in the cross-sectional SEM image and the EDS profile (Figure 6.2b to 6.2e), thereby suggesting that the SWNTs are uniformly dispersed. The membranes prepared using SWNT gels yield much more uniform SWNT dispersion than those prepared by SWNT powders.

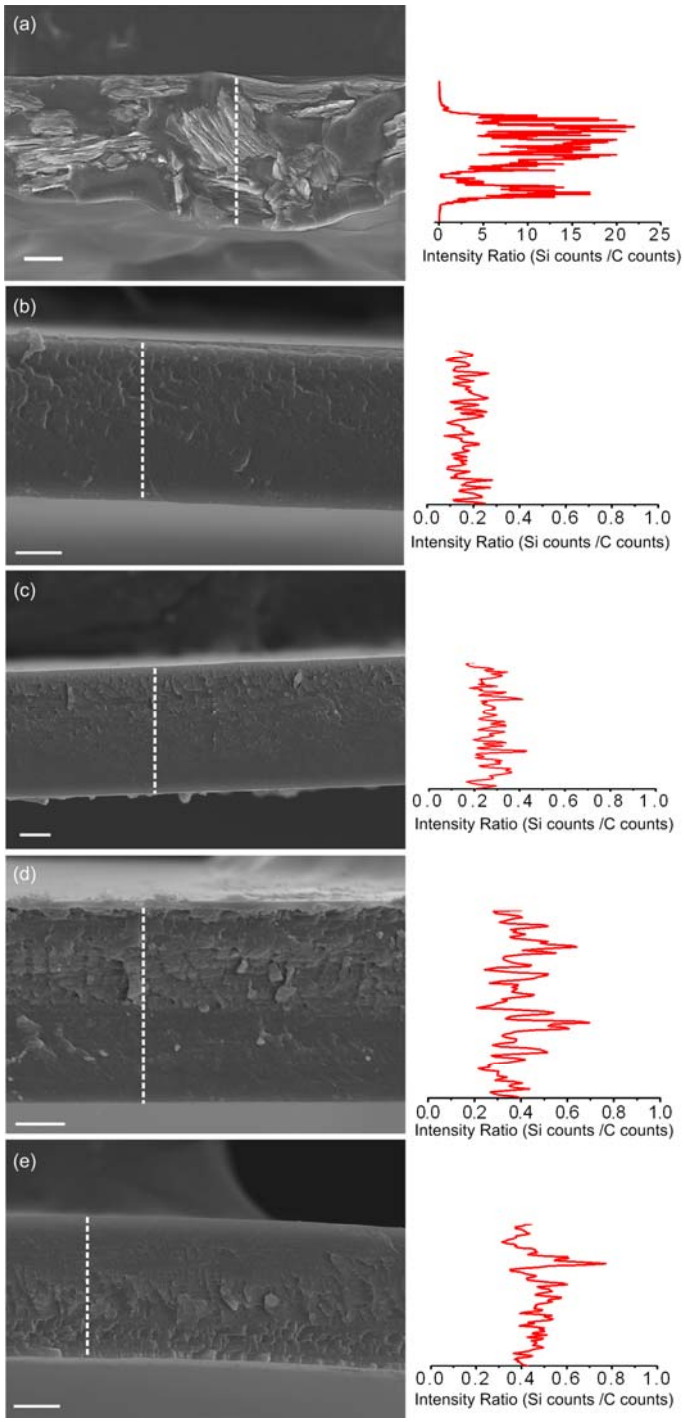

Figure 6.2 SEM images (left) and line profiles of silicon/carbon intensity from EDS patterns (right) for PVA/SWNT membranes prepared by SWNT powders or gels: (a) pwd-4 (b) gel-1 (c) gel-2 (d) gel-3 (e) gel-4. The vertical dashed lines represent the locations where EDS line profiles were measured. The scale bars represent 10 μm.

6-3 Bundling and orientation of SWNTs in composite membranes

Solid-state X-ray diffraction and scattering are excellent probes of SWNT bundling, orientation, dimensions and dispersion in a solid medium. X-ray diffraction (XRD) with respect to the Bragg angle 2θ can be used for assessing the bundling of SWNTs, and small-angle X-ray scattering (SAXS) can quantitatively elucidate the dimensions and dispersion of SWNTs in the composite membranes. The diffraction patterns of nanotubes forming small bundles are not dominated by Bragg diffraction but by X-ray scattering. In contrast to ordered porous materials such as one-dimensional zeolites, MCM-41, or SBA-15, the small bundles (e.g., bundles with fewer than 25 individual nanotubes) in nanotube materials do not provide sufficient long-range periodicity for Bragg diffraction.[79,90] Hence, an explicit atomic-scale simulation of X-ray scattering from a finite-size bundle is a more reliable tool for predicting the XRD patterns. Such simulations have been previously carried out for the aluminosilicate SWNTS and have elucidated their bundling characteristics in powder form.[97] Figure 6.3a summarizes experimental XRD patterns from SWNT powder samples and simulated patterns from different bundling arrangements. The simulated patterns clearly indicate a shoulder at 5-6^{o} 2θ as being the main difference between isolated SWNTs and bundled SWNTs. Considering the presence of this peak at 5-6^{o} 2θ in the XRD pattern of as-synthesized SWNT powder sample, it has been concluded that the SWNTs in the powder samples are not individually dispersed but instead form small 2x2 or triangular (3 SWNTs) bundles. Simulated XRD patterns of SWNTs with various bundling arrangements (3x3, 4x4, etc.) were also reported in Chapter 2.

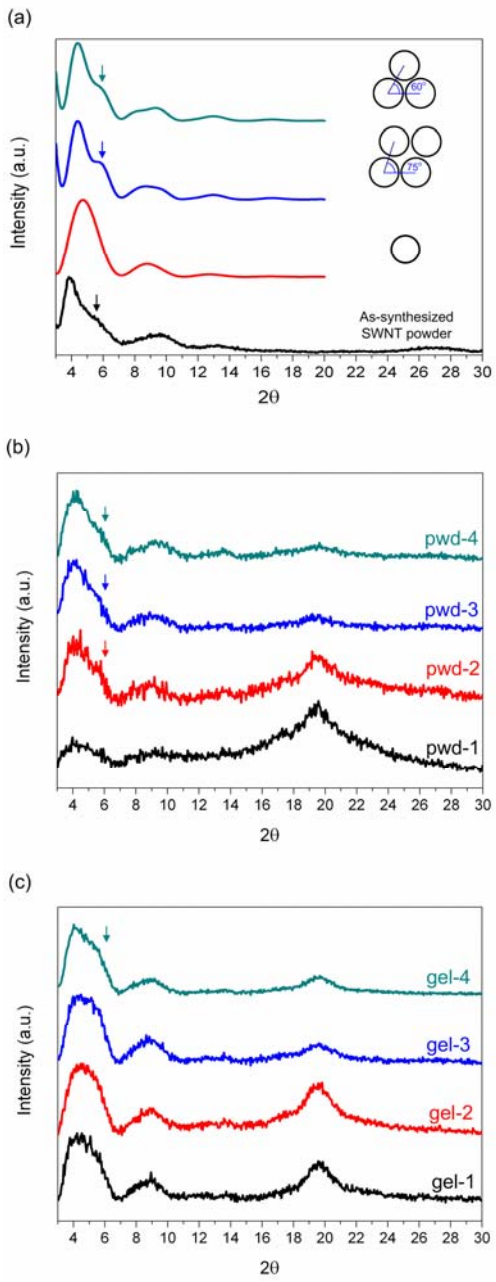

Figure 6.3 (a) Experimental SWNT XRD pattern (bottom), and simulated XRD patterns of isolated SWNTs and SWNT bundles with different bundling arrangements. The arrows indicate the shoulder peak distinctive to bundle formation. (b) XRD patterns for PVA/SWNT membranes prepared from SWNT powders. (c) XRD patterns for PVA/SWNT membranes prepared from SWNT gels. The arrows in (a)-(c) point out the "shoulder" in the patterns.

The XRD patterns of PVA/SWNT membranes prepared from powder samples (Figure 6-3b) show clear shoulder peaks for pwd-2, pwd-3, and pwd-4, indicating that the SWNT powders do not fully redisperse into individual SWNTs in the composite membranes. This observation is consistent with the SEM images, where SWNT agglomerated particles are observed in the PVA matrix. The shoulder peak in the pwd-1 sample is more difficult to observe due to the low signal-to-noise ratio of the nanotube scattering intensity at low volume fractions. The sharp peak at 19.5^{o} 2θ in all the membrane samples is due to the crystallinity of PVA polymer chains,[132] and is also observed in pure PVA membranes (Supporting Information). Composite membranes prepared using SWNT gel samples (gel-1, gel-2, and gel-3) show the absence of the shoulder peak at 5-6^{o} 2θ. (Figure 6.3c), and these experimental patterns match the simulated pattern of an isolated SWNT (Figure 6.3a), thereby providing clear evidence that the SWNTs disperse in the PVA matrix as isolated SWNTs. The PVA chains may effectively penetrate the loosely coordinated network of SWNT-water bonds existing in the gel, but are not likely able to penetrate the interstices between SWNTs in the powder. In other words, the methodology of preparing PVA/SWNT composites starting from SWNT gels overcomes the problem of obtaining individually dispersed SWNTs in a polymer matrix with high loadings (> 20 vol %).[133,134]

Small angle X-ray scattering (SAXS) can be used to assess the intertubular distances between SWNTs in the polymeric matrix. For well-dispersed cylindrical particles, the transformation of SAXS data from the momentum transfer (Q) domain into the spatial (d) domain is given by:[135-137]

$$g(d) = \frac{1}{(2\pi)^2} \int_0^\infty I(Q) \cdot Q \cdot d \cdot \sin(Q \cdot d) \cdot \exp(-D \cdot Q^2) dQ \qquad (6.1)$$

Here, d is the inter-tubular distance, $g(d)$ is the distribution function of the inter-tubular distance, Q is the X-ray momentum transfer, $I(Q)$ is the scattering intensity, and $exp(-DQ^2)$ is added to remove the "termination effect" of the transformation. Generally, the parameter D is of the same order of magnitude as $1/Q^2$,[137] and its value is taken as 500 Å^2 for calculation of all the distance distribution transformations reported in this paper. The intertubular distance distribution functions, $g(d)$, for PVA/SWNT membranes prepared from SWNT gels are summarized in Figure 6.4.

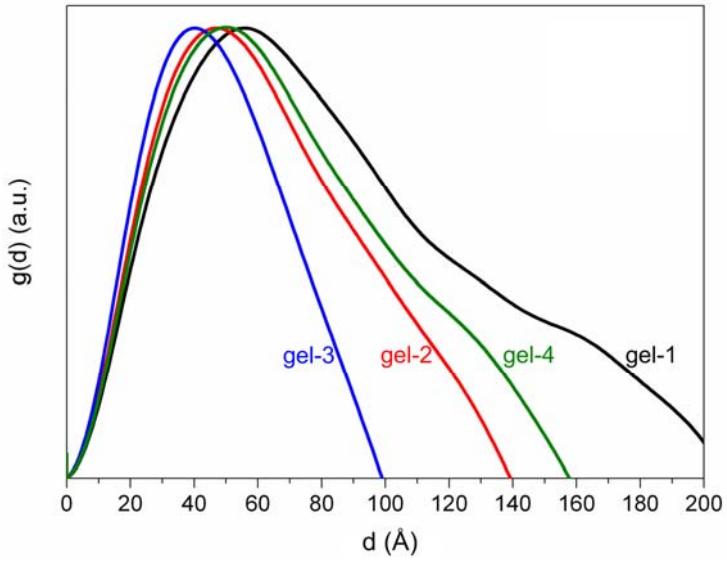

Figure 6.4 The inter-tubular distance distribution, derived from SAXS data, of SWNTs dispersed in PVA/SWNT composite membranes prepared by SWNT gel.

Generally, the most likely intertubular distance as well as the width of the distance distribution both decrease, as expected, when the SWNT volume fraction increases from 7.6% (gel-1) to 19% (gel-3). However, at higher volume fractions of 37% (gel-4), the distribution width and the most likely intertubular distance increases, perhaps due to the onset of bundle formation in the gel-4 sample as suggested by the XRD data. The most likely intertubular distance as read from Figure 6.4 is compared to the theoretical average intertubular distance between dispersed SWNTs at a given volume fraction in Table 6.1. The two quantities are in close agreement for samples gel-1, gel-2, and gel-3. In

conjunction with the clear XRD evidence presented earlier, this result further supports the notion of a uniform distribution of individual SWNTs in the PVA matrix. On the other hand, the theoretical intertubular distance for the gel-4 sample is much smaller than the distance deduced from SAXS data, suggesting that the intertubular distance distribution for gel-4 is influenced by the formation of SWNT bundles instead of individually dispersed SWNTs. Additionally, the raw SAXS data were fitted with developed models for dispersed rod-like materials[138-141] to extract the SWNT dimensions (Table 6.1).

Table 6.1 Intertubular distance, outer radius, and length of SWNTs in PVA/SWNT composite membranes prepared from SWNT gels.

SWNT vol %	8	20	33	38
d from theoretical calculation *(nm)*	6.9	4.3	3.4	3.2
d from SAXS analysis *(nm)*	5.6	4.7	4.0	5.0
r_o from SAXS analysis *(nm)*	1.15	1.15	1.12	1.20
L from SAXS analysis *(nm)*	380	550	580	500

6-4 Mixture separation by PVA/SWNT composite membranes

Recent computational studies suggest that the aluminosilicate SWNTs allow a high water diffusivity (10^{-5}-10^{-4} cm^2/s)[10,46] that is one to two orders of magnitude higher than in other microporous materials such as zeolites,[142] and also a high adsorptive water selectivity over alcohols (greater than 50 for a 1:9 water:methanol mixture).[46] PVA also has high water selectivity over organics and is the dominant polymeric material used in pervaporation membranes that dehydrate organic/water mixtures for applications such as bioethanol production.[143,144] It is hypothesized that PVA/SWNT composite membranes could allow higher throughput in such applications (due to the high permeability of water in PVA) while maintaining a high selectivity over organic molecules. An investigation on

this hypothesis was performed by a combination of experimental pervaporation measurements, transport modeling, and molecular simulations.

The permeation properties of PVA/SWNT composite membranes prepared from SWNT powders and SWNT gels were measured by pervaporation at 60 ^{o}C with an 80 wt % ethanol feed solution. The permeability and selectivity results are summarized in Figure 6.5 as a function of the SWNT volume fraction (Φ_f). Membranes prepared from SWNT gels show a monotonic water permeability increase with SWNT volume fraction. The water permeability of membranes prepared with SWNT powders show no significant improvement at lower volume fractions, but the permeabilities increase abruptly after Φ_f = 0.2. Similar trends are found for the ethanol permeability. The intrinsic membrane selectivity ($S_{water/ethanol}$) is defined as the ratio of the water and ethanol permeabilities and the values are shown in Figure 6.5. Membranes prepared from SWNT gels show a monotonic decrease in selectivity from 58 (pure PVA) to 35 (Φ_f = 0.4).

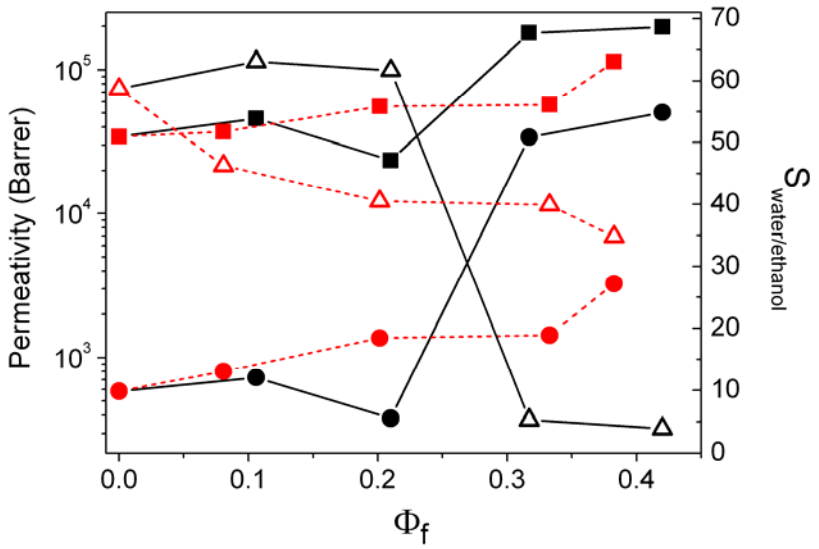

Figure 6.5 The water (solid squares) and ethanol (solid circles) permeability, and the water/ethanol selectivity (open triangles), of membranes prepared from SWNT powder (black solid lines) and gel (red dashed lines) with different SWNT volume fractions.

Membranes prepared from SWNT powders show no change in selectivity at low SWNT volume fractions, but the selectivity drops dramatically to below 5 at higher volume fractions. These results indicate that the properties of membranes made from aggregated SWNT powders are likely affected by the occurrence of defects such as interfacial voids. Therefore, the following discussion focuses only on the composite membranes made from SWNT gels.

To gain more insight into the above membrane properties, the expected water/ethanol separation performance of the SWNT at the operating conditions was computationally estimated, and coupled this information with models described in Chapter 5 for estimating the permeability of composite membranes with tubular fillers. Figure 6.6 shows the predicted permeabilities of water and ethanol, and $S_{water/ethanol}$, of the aluminosilicate SWNT in the pressure region relevant to the pervaporation measurements (0.1-45 kPa), as obtained from molecular simulations of adsorption and diffusion (as described in the Methods sections). At higher total pressures (greater than 1 kPa), the SWNT shows excellent water permeability (four orders of magnitude higher than that of PVA). At low total pressure (below 1 kPa), the SWNT has significantly diminished permeability, which is nevertheless two orders of magnitude higher than that of PVA. The ethanol permeability of the SWNT does not exhibit a strong pressure dependence, and is approximately two orders of magnitude higher than that of PVA. As a consequence, the SWNT is estimated to have a high intrinsic $S_{water/ethanol}$ of 55-75 at higher pressures, but a $S_{water/ethanol}$ of approximately unity at low pressures. The molecular simulations provide clear mechanistic insight into this phenomenon. At low pressure, both water and ethanol transport are dominated by the strong surface interactions between these molecules and the hydroxyl groups lining the SWNT wall. Strong hydrogen bonding leads to relatively slow surface diffusion of both molecules. At higher pressures, water fills the SWNT pore to a much greater extent than ethanol, forming multilayers in

the SWNT channel and exhibiting almost bulk-liquid-like diffusive behavior. The predicted high selectivity in this regime is mainly driven by strong preferential filling of water in the SWNTs and not by diffusivity differences.

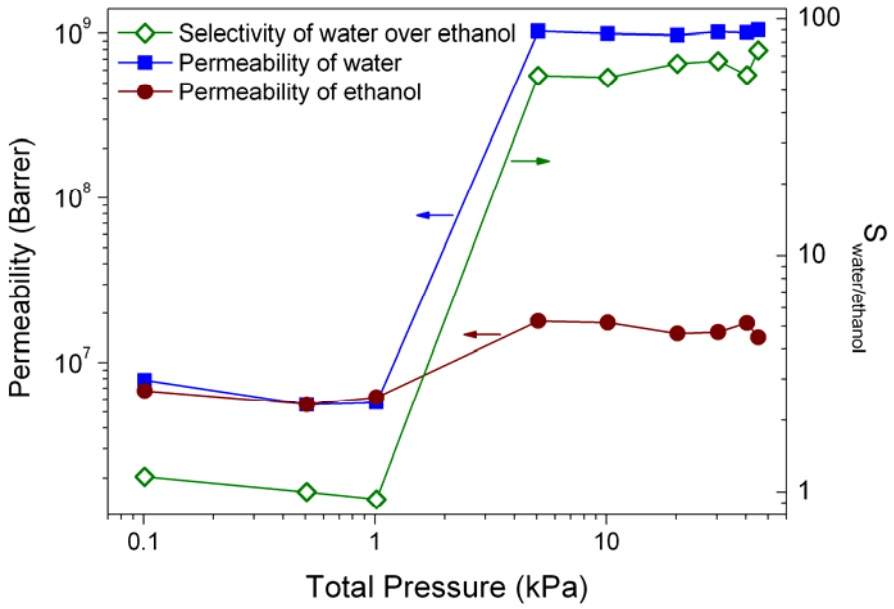

Figure 6.6 Predicted water and ethanol permeabilities, and water/ethanol selectivity, of the SWNT at different pressures as obtained from grand canonical Monte Carlo and molecular dynamics simulations.

Using the above information on the permeability of the SWNT, the experimental pervaporation results were interpreted with a macroscopic transport model. The Kang-Jones-Nair (KJN) model,[145] described in Chapter 5, is specifically for composite membranes with tubular fillers that possess perfectly anisotropic 1D transport properties. For a fixed tubular filler orientation, the KJN model predicts the effective permeability (P_{eff}) of the composite membrane as a function of the filler volume fraction (Φ_f) (Equation 5.7 and 5.14). The KJN model somewhat underestimates the effective permeability and can be considered as a close lower bound, whereas the Hamilton-

Crosser (HC) model (Equation 5.17) for isotropic cylindrical fillers can be utilized as an upper bound for predicting the effective permeability of the composite membranes.

The model predictions are compared to experiment in Figure 6.7. The experimentally measured water and ethanol permeabilities of PVA are used for the matrix ($P_{m,water}$ = 3.4×10^4 Barrer, $P_{methanol}$ = 5.8×10^2 Barrer). The average water and ethanol permeability of the SWNTs (from Figure 6-7) are $P_{f,water}$ = 5×10^8 Barrer and $P_{m,ethanol}$ = 1.1×10^7 Barrer. The aspect ratio is α = 217, and the fillers are taken to have a random orientation distribution (as known from XRD data above). Although the molecular simulations predict that the SWNT permeability varies by two orders of magnitude between low- and high-pressure conditions (Figure 6.6), it was found that the membrane permeation model results are insensitive to the SWNT permeability because the SWNT permeability is at least two orders of magnitude greater than the permeability of the matrix (PVA) at all pressures. It is well known that the effective permeability of a composite membrane becomes insensitive to the filler permeability when it exceeds the matrix permeability by more than a factor of 100. The KJN model predictions of the water permeability are in good agreement with the experimental results except at Φ_f = 0.4, whereas the HC model considerably overestimates the membrane permeability.

Both the KJN and HC models predict a higher water-over-ethanol selectivity than the experimental observations. Due to the high water selectivity of both PVA (experimentally known) and the SWNT (predicted by molecular simulation), the effective membrane selectivity in both models becomes insensitive to the SWNT volume fraction. A pronounced deviation of both permeability and selectivity from the KJN model prediction is observed at higher Φ_f = 0.4 for the membranes prepared from SWNT gels. On the other hand, the membranes pwd-1 and pwd-2 prepared from SWNT powders

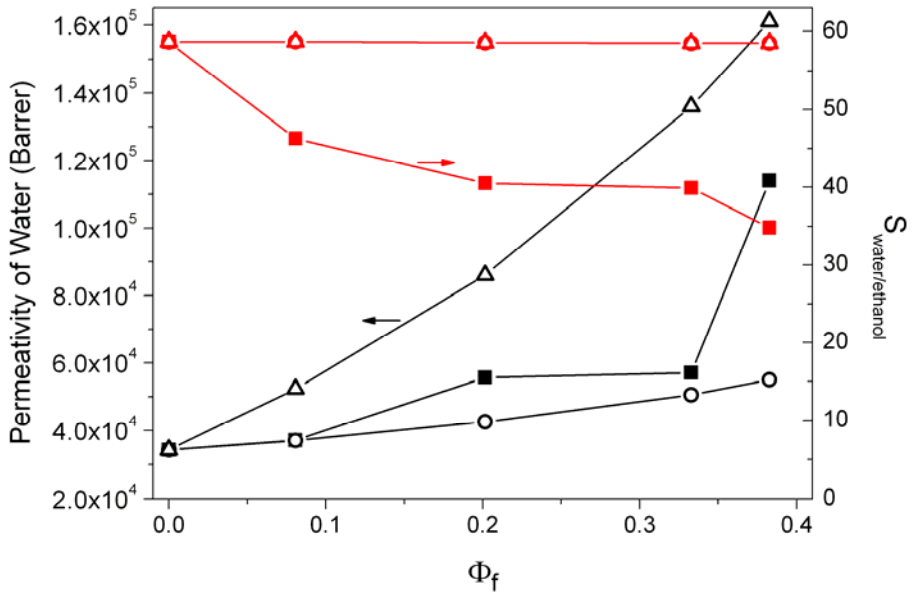

Figure 6.7 Comparison of water permeability and water/ethanol selectivity obtained from pervaporation experiments (solid squares), predictions of the KJN model (open circles), and predictions of the HC model (open triangles), for PVA/SWNT membranes prepared from SWNT gels.

maintain the water permeability and water/ethanol selectivity at the expected level (similar to the pure PVA membrane). These observations can be explained by several potential mechanisms, of which two appear to be most likely. Firstly, it is possible that the lower experimental value of the selectivity reflects an inaccuracy in the predictions of water selectivity in the SWNT. The permeability of ethanol during binary permeation along with water through the SWNT could be substantially different from the single-component permeability. A second possibility is the occurrence of changes in the microstructure and transport properties of the PVA matrix in the presence of large quantities of SWNT fillers and a large interfacial area between the PVA matrix and the outer surfaces of the SWNTs. For example, the molecular-scale structure of the PVA chains and the swelling behavior of PVA in the presence of water could be significantly altered by the presence of well-dispersed SWNT fillers.[146] In the membranes made from

SWNT gels, the average intertubular distance is in the range of 3.5-6 nm, so that there is nanoscale confinement of PVA in the spaces between the dispersed SWNTs. Furthermore, the nanotube-PVA interfacial area in these composites is relatively large (0.32-1.5×10^{11} m^2/m^3 membrane volume). As a consequence, the water permeability and selectivity of the PVA matrix in the nanocomposite membranes could deviate substantially from those of the pure PVA membranes, due to altered molecular transport properties in the nanoconfined PVA chains and near the PVA/SWNT interfaces, The PVA/SWNT membranes prepared from SWNT powder samples display poor dispersion of the SWNTs in PVA and a much lower nanotube-PVA interfacial area than the PVA/SWNT membranes prepared from SWNT gel samples, and hence the polymeric matrix remains as a continuous phase with properties essentially identical to the pure PVA membrane. The pwd-1 and pwd-2 membranes therefore have fairly similar water/ethanol transport properties as the pure PVA membrane, since the microstructure of PVA does not change significantly and the incorporated SWNTs become "inactive fillers" due to their severe agglomeration. A detailed molecular-level study of the microstructure and dynamics of the nanoconfined PVA matrix is presented in the following section.

6-5 Crystallinity and dynamics of PVA

The crystallinity of the PVA matrix with different SWNT loadings is determined from the XRD patterns shown in Figure 6.8. The peak at 19.5° 2θ is assigned to the $(10\bar{1})$ reflection.[147,148] This peak can be deconvoluted into two parts: a sharp crystalline domain and a broader amorphous component. The crystallinity of the PVA matrix is taken as the ratio of the diffraction intensity of the crystalline domain to the total intensity. For composite membranes prepared using the SWNT gels, the crystallinity monotonically decreases as the SWNT loading increases (from 46% for the pure PVA membrane to 27% for the composite incorporated with 38 vol% of SWNTs). The cause of the decrease in

crystallinity is perhaps that the well-dispersed SWNTs interfere with the formation of hydrogen bonds between PVA polymer chains, impeding the formation of crystalline domains in the PVA matrix.

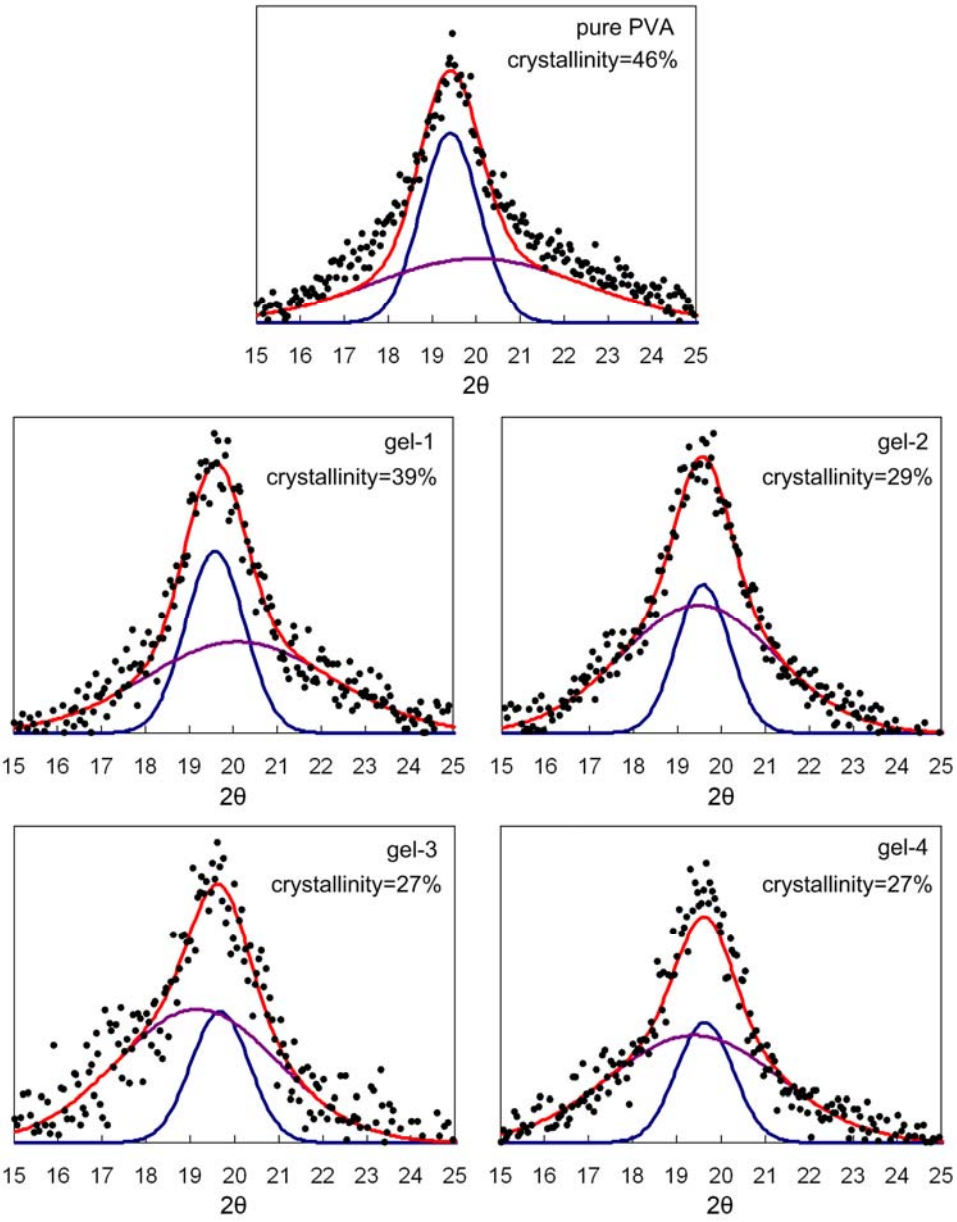

Figure 6.8 XRD patterns highlighting the crystalline phase in the PVA matrix, for the pure PVA and the PVA/SWNT composite membranes. The black dots are raw experimental data. Each pattern is fitted by two Gaussian distributions, representing the crystalline phase (blue) and the amorphous phase (purple) respectively. The red curves represent the summation of contributions from both the crystalline and the amorphous phases.

While XRD probes the crystallinity of the PVA matrix, solid-state NMR is an excellent tool for studying the polymer chain dynamics. Specifically, a higher relative intensity between the central band and the spinning side band in ^{1}H NMR implies a higher proton concentration and mobility.[56,57] Given approximately the same amounts of sample packed into the NMR rotor, the PVA/SWNT composite samples would possess a lower proton concentration from PVA than the pure PVA membrane. However, a much stronger central-band-to-spinning-side-band ratio is observed for the gel-4 sample in comparison to the pure PVA membrane (Figure 6.9a). This observation suggests that the protons from the PVA polymer chains in the gel-4 sample have significantly higher mobility than in the pure PVA sample. Faster proton dynamics implies a higher PVA chain mobility in the matrix phase of the gel-4 sample. Furthermore, the spectral resolution for the gel-4 sample is much higher than the pure PVA sample at very similar experimental conditions (Figure 6.9b). Peak assignments for the area of 0-5 ppm are based upon a structure of the partially crosslinked PVA by glutaraldehyde. Peaks between 5-10 ppm in the spectrum for the gel-4 sample are contributed by protons from SWNTs. The proton denoted by "e" at 9-10 ppm in the partially crosslinked PVA structure, is not observed in the PVA/SWNT composite membrane, likely due to its low intensity in comparison to signals from the SWNTs in that region. Since the spectral resolution of ^{1}H NMR can be enhanced by the proton mobility, the higher resolution seen in the gel-4 sample also supports its higher proton/PVA chain mobility in comparison to the pure PVA membrane. The observed higher PVA chain mobility for the PVA/SWNT composite membranes is in agreement with its lower crystallinity (determined by XRD), since amorphous polymer chains are expected to have faster dynamics than ordered crystalline polymers.

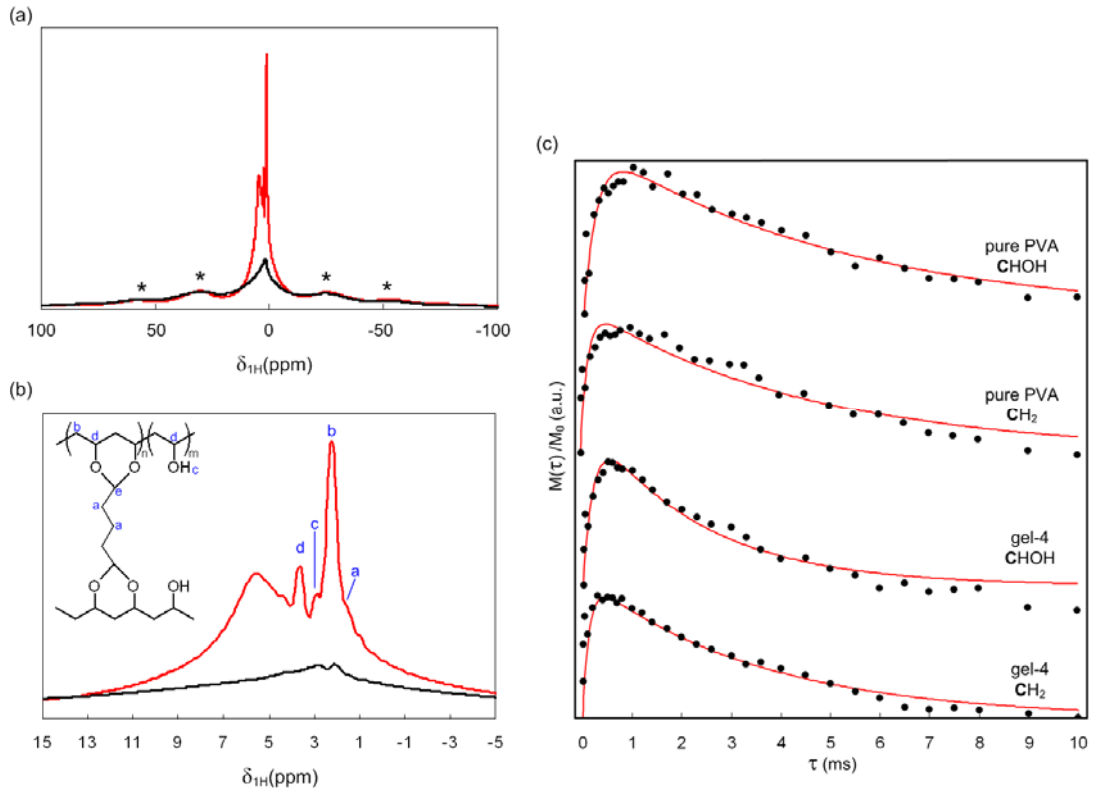

Figure 6.9 (a) A large spectral region of the ^{1}H spectra for the pure PVA (black) and the gel-4 (red) samples. The asterisks (*) denote to the spinning side bands. (b) A narrower spectral region of the ^{1}H spectra for the pure PVA (black) and the gel-4 (red) sample. (c) The normalized peak intensity of two different carbons (**C**HOH and **C**H_2) in PVA versus the contact time for both the pure PVA and the gel-4 samples. The black dots are the raw data and the red curves are the fitted results.

Additionally, $^{1}H \rightarrow {}^{13}C$ cross-polarization (CP) measurements with a series of CP contact times (τ) were used to obtain microstructural and dynamical information on the PVA matrix. ^{13}C CP-NMR spectra were recorded for the pure PVA and the gel-4 sample with various contact times. In the obtained spectra, there are two distinct peaks contributed by two different carbon atoms in PVA (**C**H_2 and **C**HOH). The intensity of the NMR signals for these two carbons is estimated respectively from the obtained spectra as a function of τ. The peak intensity from the raw ^{13}C CP spectra, normalized by the maximum intensity among the series of measurements, is summarized in Figure 6.9c. Two time constants, $T_{1\rho}(^{1}H)$ and T_{CH}, can be derived by fitting the normalized peak intensity with the following equation:[149,150]

$$\frac{M(\tau)}{M_0} = \left[\frac{e^{-\tau / T_{1\rho}(^{1}H)} - e^{-\tau / T_{CH}}}{1 - T_{CH} / T_{1\rho}(^{1}H)} \right] \qquad (6.2)$$

where $M(\tau)$ is the intensity for a specific carbon in the ^{13}C spectra at a given contact time and M_0 is the maximum peak intensity among the performed experimental series. The derived $T_{1\rho}(^{1}H)$ and T_{CH} are summarized in Table 6.2.

Table 6.2. Parameters derived from the contact time measurements by the pure PVA and the gel-4 sample.

	$T_{1\rho}(^{1}H)$ (ms)		T_{CH} (ms)	
	CHOH	**C**H_2	**C**HOH	**C**H_2
pure PVA membrane	4.98	4.48	0.25	0.14
gel-4	2.25	1.96	0.20	0.13

For semi-crystalline materials (such as the prepared PVA/SWNT membranes), the amorphous phase acts as a relaxation sink. The constant $T_{1\rho}(^{1}H)$ for semi-crystalline materials represents the spin-diffusion time for the nuclear magnetization from the

crystalline phase to the amorphous phase. The crystalline domain size, $\langle x \rangle$, can be correlated to $T_{1\rho}(^1H)$ as

$$\langle x \rangle \sim \left(D_s \times T_{1\rho}(^1H) \right)^{\frac{1}{2}} \qquad (6.3)$$

where D_s is the spin-diffusion coefficient.[151] The lower $T_{1\rho}(^1H)$ values of **C**H_2 and **C**HOH for the gel-4 sample in comparison to the pure PVA membrane, suggest that the SWNT-containing PVA matrix has a smaller crystalline domain size than pure PVA. On the other hand, the constant of T_{CH} represents the characteristic time for polarization transfer from the protons to the carbon nuclei.[152] The value of T_{CH} is thus determined by both dynamical and structural effects: the mobility of the carbon adjacent to protons, and the proton concentration around the carbon. Specifically, a short T_{CH} implies low carbon mobility or fewer protons in its immediate environment.[153] However, similar T_{CH} values are observed for the pure PVA and the gel-4 sample. Since the investigation suggests a higher polymer chain mobility for the gel-4 sample, the observation of similar T_{CH} values is attributed to the fact that the carbons in the PVA/SWNT composite membranes have a larger number of adjacent protons, due to the presence of SWNTs with a dense coverage of hydroxyl groups on their outer surfaces.

6-6 Summary

The presented work has demonstrated the fabrication and detailed characterization of free-standing nanocomposite membranes containing a high loading (up to ~40 vol %) of aluminosilicate single-walled nanotubes (SWNTs) well-dispersed in a PVA matrix. PVA/SWNT membranes prepared using SWNT gels were characterized by XRD (including rocking curve measurements), EDS, and SAXS measurements and analysis. These membranes show high uniformity, excellent dispersion of individual SWNTs (up

to ~30 vol %), and the onset of bundle formation (3-4 SWNTs per bundle) at a SWNT loading of ~40 vol %. Analysis of SAXS data reveals the SWNT dimensions and the intertubular distance distribution. The transport properties of the PVA/SWNT membranes relevant to applications in the dehydration of ethanol/water mixtures, were investigated by pervaporation measurements, molecular simulation, and transport modeling. The membranes substantially enhance the water throughput with increasing SWNT volume fraction (up to 200% higher water permeability than pure PVA membranes at a SWNT loading of ~40 vol %), but led to a moderate reduction of the water/ethanol selectivity from 58 (pure PVA) to 35 (SWNT loading ~ 40 vol %). Detailed XRD and solid-state NMR studies suggest that the reduction of water/ethanol selectivity is likely due to the microstructural change of the PVA matrix with incorporation of SWNTs. Specifically, the crystallinity of the PVA matrix goes down (from 46% to 27% with 38 vol% of SWNT incorporated) and the mobility of PVA chains increases with the presence of SWNTs in the matrix. This study shows that it is possible to fabricate SWNT/polymer nanocomposite membranes with a high-quality microstructure by inexpensive solution processing techniques, and gain insight into their permeation properties by a combination of experimental measurements and predictions by computational and theoretical methods.

CHAPTER 7

THIN (SUBMICRON) SUPPORTED ALUMINOSILICATE NANOTUBE/POLY(VINYL ALCOHOL) NANOCOMPOSITE MEMBRANES

In this chapter, the preparation, characterization, and permeation properties of thin (thickness < 500nm) supported polymer/SWNT composite membranes with high loading is reported. Specifically, the loading of well-dispersed SWNTs in poly(vinyl alcohol) (PVA) membranes is systematically increased up to 60% by mass and the properties of the nanotubes are assessed. The microstructure of the thin supported membranes is assessed qualitatively and quantitatively by scanning electron microscopy (SEM), and X-ray diffraction (XRD). Subsequently, the mass transport properties of the PVA/SWNT composite membranes are studied by CO_2/CH_4 permeation measurements.

7-1 Experimental details

7-1-1 Preparation of supported aluminosilicate SWNT/PVA composite membranes

A porous poly(propylene) support was placed in a poly(styrene) petri dish and masked with waterproof tapes. A 30 mL mixture containing water, SWNT gels, and PVA was poured to the petri dish. 8mg of PVA was added in the mixture for making pure PVA membranes, 4mg of PVA and 1.2g SWNT gels for 45 wt% PVA/SWNT composite membranes, and 2mg of PVA and 1.55g SWNT gels for 60 wt% PVA/SWNT composite membranes. The aqueous mixture in the petri dish was placed in a 50^{o}C oven for 24 hours for casting membranes. The resulting membranes were annealed at 100^{o}C for 12 hours. To repair the pinholes in the as-made membranes, a 20 wt% PDMS solution in iso-octane was dropwised on the top of the membranes. During the PDMS treatment, the membranes were placed on a manifold in a 60^{o}C oven and vacuum was applied on the

bottom side of the membranes. The treated membranes were placed in a 60^{o}C oven for 12 hours to cure applied PDMS.

7-1-2 Scanning Electron microscopy (SEM)

The morphology of SWNT/PVA composite membranes was imaged with a scanning electron microscope (SEM, Hitachi S-3700N). To observe the cross-sectional morphology, the membranes were cryogenically fractured in liquid N_2. Energy dispersive spectroscopy (EDS) analysis of the cross-sections was carried out with the same instrument.

7-1-3 XRD measurements and simulations

X-ray diffraction (XRD) scans in grazing-angle geometry were performed on a PAnalytical X'pert Pro MPD diffractometer operating with a Cu Kα source. Diffraction data were collected with a collimator and Miniprop detector, in the range of 3-30^{o} 2θ and a step size of 0.05^{o}. XRD simulations were performed to investigate the extent of SWNT bundling. The Reflex module of the Materials Studio 3.2 molecular simulation package (Accelrys, Inc.) was used, and the details of such simulations have been reported in Chapter 2.

7-1-4 CO_2/CH_4 permeation

The composite membranes were placed in a sealed manifold and degassed at 100^{o}C for 72 hours prior to the permeation measurements. The outgassed membranes were exposed to a 4-bar CO_2 or CH_4 as a feed. The volume on the permeate side of tested membranes was kept constant. The pressure on the permeate side was about 10^{-3} bar at the beginning of a measurement. The measurement was stopped when the pressure on the permeate side went to about 10^{0} bar. The flux of CO_2 or CH_4 was estimated from the increase of the permeate pressure, the duration of the measurement, and the membrane area.

7-2 Membrane morphology and SWNT dispersion

The morphology of prepared thin supported membranes was probed by scanning electron microscopy (SEM) (Figure 7.1). The cross-sectional SEM images clearly suggest that a continuous PVA/SWNT layer can be cast on the top of the PP support without observable micron-/sub-micron-level defects. The thickness of supported pure PVA membranes is about 460 nm, 45 wt% SWNT membranes about 320 nm, and 60wt% SWNT membranes about 330 nm.

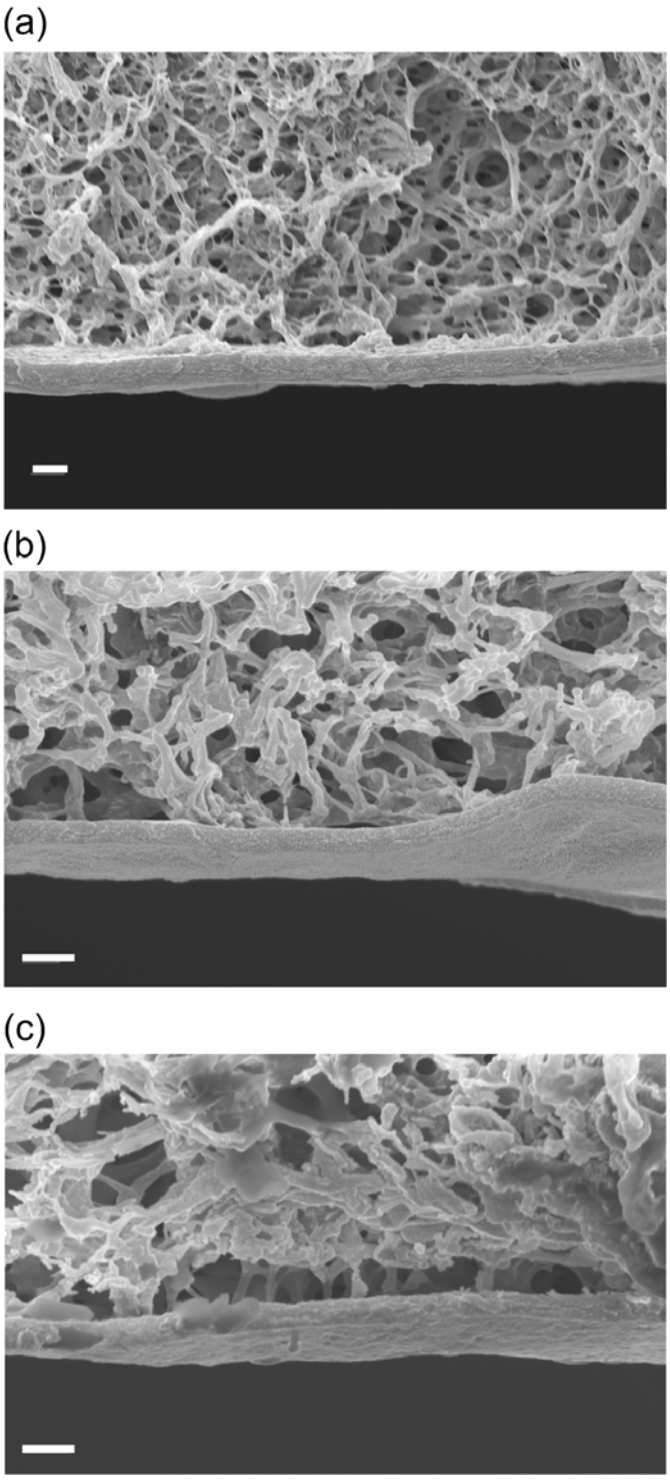

Figure 7.1 Cross-sectional SEM images of thin supported (a) PVA (b) 45 wt% SWNT (c) 60 wt% SWNT membranes. In each image the top layer is the PP support and the bottom layer is the PVA/SWNT membrane. The scale bars represent 500 nm.

X-ray diffraction (XRD is an excellent tool for investigating the bundling character of SWNTs. The simulated and experimental XRD patterns are summarized in Figure 7.2

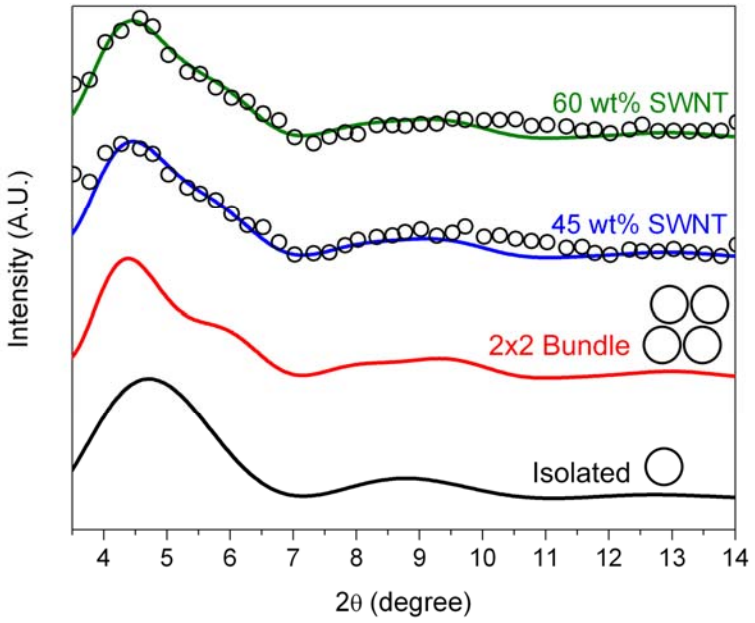

Figure 7.2 Simulated (solid curves) and experimental (open circles) XRD patterns. Two simulated patterns on the bottom represent the isolated SWNT and SWNT forming 2-by-2 bundles. The two simulated patterns on the top are linear combinations of the bottom two patterns for achieving the best fits for experimental results.

The investigation in Chapter 5 suggest that SWNT can disperse in PVA matrix as individual nanotubes at low SWNT loading (< 40 wt%). However, according to the presented XRD patterns for the composite membranes with 45 wt% and 60 wt% SWNT, it is likely that a portion of SWNTs form small bundles (bundles composed of three or four SWNTs) in the matrix whereas the other portion of SWNT disperses individually. To quantify the degree of SWNT bundling in the matrix, it was assumed that the experimental XRD patterns are linear combinations of patterns coming from isolated SWNTs and SWNTs forming 2-by-2 bundles. The coefficients for the linear combinations of these two simulated patterns were adjusted to achieve the best fits for

experimental XRD patterns (Figure 7.2). The degree of the bundling of SWNTs in the supported composite membranes can thus be determined. Based upon the fitting results, there are 40% of SWNT in the membrane composed of 45 wt% SWNT dispersing individually, and 35% of SWNT in the membrane composed of 65 wt% SWNT dispersing individually.

7-3 Molecular separation performance of supported SWNT/PVA nanocomposite membranes

CO_2 and CH_4 single gas permeation measurements were performed to evaluate the permeation properties of the thin supported nanocomposite membranes. The permeation results are summarized in Table 7.1.

Table 7.1 CO_2/CH_4 single gas permeation results.

	CO_2 Permeance (GPU)	CH_4 Permeance (GPU)	CO_2/CH_4 Selectivity (--)
PVA	24.9 +/- 0.1	29.4 +/- 4	0.85 +/- 0.3
PVA treated with PDMS	1.79 +/- 0.1	0.68 +/- 0.1	2.6 +/- 0.5
45 wt% bare SWNT*	13.8 +/- 2.1	4.91	2.8 +/- 0.4
60 wt% bare SWNT*	16.4 +/- 2.9	5.8 +/- 0.1	2.7 +/- 0.5
45 wt% amine SWNT*	6.24 +/- 2.7	2.01 +/- 0.4	3.1 +/- 0.4
60 wt% amine SWNT*	9.93	2.79 +/- 0.1	3.6 +/- 0.1

*Membranes composed of SWNTs were treated with PDMS prior to the permeation measurements

According to the CO_2/CH_4 selectivity (0.85), which is close to the Knudsen selectivity (0.6), of supported bare PVA membranes without a PDMS treatment, it is likely that the

pinholes present in the thin membrane dominate the mass transport. With a post-casting PDMS treatment, the supported PVA membranes show a CO_2/CH_4 selectivity of 2.6, which indicates that the mass transport is now dominated by the dense PVA matrix. This PDMS treatment was thereby applied in the preparation of nanocomposite membranes with nanotubes as fillers and PVA as matrix.

In the composite membranes with 45 and 60 wt% of bare SWNTs, significant increases of membrane permeance for both CO_2 and CH_4 was observed (Table 7.1). At the same time, these two membrane samples preserve the CO_2/CH_4 selectivity of pure PVA membranes, which suggests that the enhancement of the CO_2 permeance is likely due to the incorporated SWNTs but not due to the pinholes, which might not be fully repaired via the PDMS treatment. The CO_2 permeance enhancement factor (7.7 for 45 wt% SWNT incorporation and 9.2 for 60 wt% SWNT incorporation) is much higher than model prediction for the thick-film architecture (1.8 for 45 wt% SWNT incorporation and 2.4 for 60 wt% SWNT incorporation, assuming that the CO_2 permeability of SWNT is higher than the CO_2 permeability of PVA by at least three order of magnitude). It is likely that this enhancement is caused by a portion of the incorporated SWNTs spanning across the membrane providing direct mass transport pathways for increasing the permeance. The hypothesis of a portion of SWNTs in the thin membranes spanning across the membranes can be supported by the relative dimensions of the membrane and the SWNTs. The incorporated SWNTs have an average length of 380 nm, and the average thickness of the nanotube membranes is about 320 nm. Therefore, it is reasonable that a certain portion of SWNTs in the composites can span across the membrane. To quantify the percentage of SWNTs spanning across the membrane, I compared the observed CO_2 permeabilities with the model-predicted permeabilities for (a) the composite membranes wherein no tubular fillers span across the membranes (Equation 5.7) and (b) membranes wherein every tubular filler spans across the

membrane (Equation 5.8). The comparison is shown in Table 7.2. Given the information in Table 7.1, the percentage of tubular fillers spanning across the membranes can be estimated. There are 0.013 % SWNTs in the membrane with 45 wt% SWNT and 0.011 % SWNTs in the membrane with 60 wt% SWNT spanning across the membrane. The results suggest that even though only a small portion (~0.01 %) of SWNTs can provide direct mass transport pathways, the overall membrane permeamance can be substantially enhanced by one order of magnitude. The supported thin nanotube membrane is thus demonstrated experimentally to be a possibly ideal architecture for enhancing the membrane performance with incorporated SWNTs.

Table 7.2 Measured and model-predicted CO_2 permeabilities (in GPU) of thin SWNT-PVA membranes

	45 wt% bare SWNT	60 wt% bare SWNT
Measured CO_2 permeance	13.8	16.4
Predicted CO_2 permeance assuming no fillers spanning across the membranes	3.0	4.1
Predicted CO_2 permeance assuming all fillers spanning across the membranes	8.6×10^4	1.1×10^5

When incorporating the amine-functionalized SWNTs (prepared by the direct-synthesis approach described in Chapter 4), a decrease in permeance and an increase in selectivity are observed in comparison to bare-SWNT-containing membranes (Table 7.1). The decrease in permeability is likely due to a smaller pore size of amine-functionalized SWNTs than bare SWNTs. Additionally, the non-uniform interior surface created by a *ca.* 20% amine-group substitution for hydroxyl groups might also contribute to the decrease

of the permeance. The observed increase of CO_2/CH_4 selectivity could be attributed to the amine groups present in the SWNT interior, which possess higher affinity to CO_2 than CH_4. When comparing the separation properties between the pure PVA and composite membranes with amine-functionalized SWNTs, significant enhancements on both permeance (permeance enhancement factor of 3.5 for 45 wt% incorporation and of 5.5 for 60 wt% incorporation) and selectivity were observed. Therefore, the incorporation of amine-functionalized SWNTs in thin supported membranes has been demonstrated as a new approach for achieving high separation performance.

CHAPTER 8

CONCLUSIONS AND OUTLOOK

The work described in this thesis develops the science and technology of nanotubes and nanotube-containing membranes for molecular transport and separations. A number of significant challenges exist along this path, which were addressed by a strategy that combined surface property investigations, interior functionalization, synthesis of hybrid materials, mass transport modeling, and free-standing and supported membrane fabrication and characterization techniques. The investigations have addressed several long-standing challenges of nanotube technology and created opportunities for applying nanotube materials in scalable membrane separation units. The key achievements are the following:

1. Molecular level details of dehydration and dehydroxylation phenomena of aluminosilicate nanotubes have been elucidated. This critical information enables a number of phenomena such as interior modification, molecular transport, and controlled delivery of molecules.

2. A post-synthesis interior functionalization methodology has been successfully developed. Through surface reactions, diverse organic entities can be immobilized at the inner surface of aluminosilicate nanotubes and thereby the hydrophilicity and interior surface properties can be tailored. This study is the first demonstration of covalent modification of the interior of single-walled nanotubes.

3. A direct synthesis route for functionalizing aluminosilicate nanotubes has been developed via using silanes with functional groups as starting materials for the nanotube synthesis. This approach allows for a one-step route for the incorporation of

functional groups at the interior of nanotubes. The two functionalization methods developed (post-synthesis and direct functionalization) may allow for a new class of applications of nanotube materials, including separations, catalysis, and molecular capture/encapsulation/storage.

4. Analytical models have been developed for quantitatively predicting the separation properties of composite membranes with tubular fillers. These models provide a useful guidance for evaluating/optimizing existing nanotube-based membranes as well as preparing nanotube-based membranes with novel device architectures and enhanced separation performance.

5. Free-standing nanotube/polymer composite membranes with good organic-inorganic interface adhesion and good nanotube dispersion have been successfully fabricated and applied in scalable membrane separation devices. Molecular-level insights of morphological changes of polymer chains due to nanotube incorporation have been elucidated.

6. Thin supported composite membranes (thickness < 500 nm) with bare and amine-functionalized nanotubes have been fabricated and evaluated for their CO_2/CH_4 separation performance. A significant improvement (nearly one order of magnitude) on membrane permeance and CO_2/CH_4 selectivity (with incorporation of amine-functionalized nanotubes) was observed. Such performance enhancement is likely due to a portion of incorporated nanotubes spanning across the membranes that provides direct mass transport pathways for molecules.

To allow the nanotube-based membranes to realize their potential of transcending the limitations of current nanocomposite membranes and to further push the limits on

nanotube membrane technology, it is worth identifying some key directions for future investigations:

1. The self-assembly mechanisms for the synthesis of functionalized nanotubes

   To optimize the separation performance of nanotubes, it is critical to be able to create desirable interior functionalities. Although the present study has discovered a direct synthesis methodology for partially substituting silanol with amine groups, the substitution ratio and the types of functional groups that can be incorporated in the nanotube frameworks are limited. To overcome such limitations, it is necessary to understand the self-assembly mechanisms for synthesizing nanotubes with starting materials possessing functional groups. A recently-developed approach for investigating the synthesis mechanism for bare aluminosilicate nanotubes from kinetic and thermodynamic perspectives[44,154,155] can be effectively applied in the assembly-mechanism studies for functional nanotubes.

2. Transfer of nanotubes from the aqueous phase to the organic phase

   The fabrication of aluminosilicate nanotube/polymer composites is limited by the poor compatibility of nanotubes and organic solvents. The aluminosilicate nanotubes are known to be able to disperse individually in an aqueous phase but suffer from a severe agglomeration in organic phases.[156] Such a characteristic makes it challenging to fabricate inorganic-organic composites with polymers that can only dissolve in organic solvents. Although several reports have described the modification of the external surfaces of aluminosilicate nanotubes for their dispersion in organic solvents,[157-159] the bundling character of nanotubes dispersed in organic solvents has never been rigorously evaluated. The transfer of aluminosilicate nanotubes from the aqueous phase to the organic phase could be realized via controlled external surface modifications at the aqueous-organic interface[160,161] followed by dispersion

characterization, such as small angle X-ray scattering[162] or dynamic light scattering.[42,43]

3. Thin (submicron) nanotube membranes with vertically aligned nanotubes

   The mass transport modeling work described in Chapter 5 suggests that a high membrane separation performance could be achieved via ultra-thin nanotube membranes with vertically aligned tubular fillers spanning across the membranes. Previous reports described the alignment of carbon nanotubes via applying shear flow[16,116] or electric field,[15] or depositing nanotubes on substrates that have distinct surface properties than the external surface of nanotubes.[163,164] Another potential challenge for the fabrication of ultra-thin (~ 50-100 nm) nanotube membranes for separations is to avoid the presence of defects. Defect-free membranes could either be prepared by optimizing the membrane fabrication conditions or be obtained with post-fabrication treatments for repairing/sealing the defect spots.[165-167]

REFERENCES

(1) Iijima, S. *Nature* **1991**, *354*, 56-58.
(2) Lau, K. T.; Gu, C.; Hui, D. *Composites Part B-Engineering* **2006**, *37*, 425-436.
(3) Wang, J. *Electroanalysis* **2005**, *17*, 7-14.
(4) Bokobza, L. *Polymer* **2007**, *48*, 4907-4920.
(5) Choi, W.; Abrahamson, J. T.; Strano, J. M.; Strano, M. S. *Materials Today* **2010**, *13*, 22-33.
(6) Dai, H. J.; Javey, A.; Pop, E.; Mann, D.; Kim, W.; Lu, Y. R. *NANO* **2006**, *1*, 1-13.
(7) Whitby, M.; Quirke, N. *Nature Nanotechnol.* **2007**, *2*, 87-94.
(8) Konduri, S.; Tong, H. M.; Chempath, S.; Nair, S. *J. Phys. Chem. C* **2008**, *112*, 15367-15374.
(9) Sholl, D. S.; Johnson, J. K. *Science* **2006**, *312*, 1003-1004.
(10) Zang, J.; Konduri, S.; Nair, S.; Sholl, D. S. *ACS Nano* **2009**, *3*, 1548-1556.
(11) Holt, J. K.; Park, H. G.; Wang, Y. M.; Stadermann, M.; Artyukhin, A. B.; Grigoropoulos, C. P.; Noy, A.; Bakajin, O. *Science* **2006**, *312*, 1034-1037.
(12) Talapatra, S.; Krungleviciute, V.; Migone, A. D. *Phys. Rev. Lett.* **2002**, *89*.
(13) Gordon, P. A.; Saeger, P. B. *Ind. Eng. Chem. Res.* **1999**, *38*, 4647-4655.
(14) Arora, G.; Sandler, S. I. *J. Chem. Phys.* **2005**, *123*.
(15) Mauter, M. S.; Elimelech, M.; Osuji, C. O. *ACS Nano* **2010**, *4*, 6651-6658.
(16) Pujari, S.; Rahatekar, S. S.; Gilman, J. W.; Koziol, K. K.; Windle, A. H.; Burghardt, W. R. *J. Chem. Phys.* **2009**, *130*.
(17) Chen, W.; Tao, X. M. *Macromol. Rapid Commun.* **2005**, *26*, 1763-1767.
(18) Song, C. S.; Kwon, T.; Han, J. H.; Shandell, M.; Strano, M. S. *Nano Lett.* **2009**, *9*, 4279-4284.
(19) Zhao, Y.-L.; Stoddart, J. F. *Acc. Chem. Res.* **2009**, *42*, 1161-1171.
(20) Singh, S.; Kruse, P. *Int. J. Nanotechnol.* **2008**, *5*, 900-929.
(21) Vaisman, L.; Wagner, H. D.; Marom, G. *Adv. Colloid Interface Sci.* **2006**, *128*, 37-46.
(22) Moniruzzaman, M.; Winey, K. I. *Macromolecules* **2006**, *39*, 5194-5205.
(23) Kuzmany, H.; Kukovecz, A.; Simon, F.; Holzweber, A.; Kramberger, C.; Pichler, T. *Synth. Met.* **2004**, *141*, 113-122.
(24) Singh, P.; Campidelli, S.; Giordani, S.; Bonifazi, D.; Bianco, A.; Prato, M. *Chem. Soc. Rev.* **2009**, *38*, 2214-2230.
(25) Bernardo, P.; Drioli, E.; Golemme, G. *Ind. Eng. Chem. Res.* **2009**, *48*, 4638-4663.
(26) Robeson, L. M. *J. Membr. Sci.* **2008**, *320*, 390-400.
(27) Baker, R. W. *Ind. Eng. Chem. Res.* **2002**, *41*, 1393-1411.
(28) Robeson, L. M.; Freeman, B. D.; Paul, D. R.; Rowe, B. W. *J. Membr. Sci.* **2009**, *341*, 178-185.
(29) Bae, T. H.; Liu, J. Q.; Lee, J. S.; Koros, W. J.; Jones, C. W.; Nair, S. *J. Am. Chem. Soc.* **2009**, *131*, 14662-+.
(30) Shimekit, B.; Mukhtar, H.; Murugesan, T. *J. Membr. Sci.* **2011**, *373*, 152-159.
(31) Mahajan, R.; Koros, W. J. *Polym. Eng. Sci.* **2002**, *42*, 1420-1431.
(32) Mahajan, R.; Koros, W. J. *Polym. Eng. Sci.* **2002**, *42*, 1432-1441.
(33) Tseng, H. H.; Kumar, I. A.; Weng, T. H.; Lu, C. Y.; Wey, M. Y. *Desalination* **2009**, *240*, 40-45.

(34) Ismail, A. F.; Goh, P. S.; Sanip, S. M.; Aziz, M. *Sep. Purif. Technol.* **2009**, *70*, 12-26.
(35) Rao, P. S.; Wey, M. Y.; Tseng, H. H.; Kumar, I. A.; Weng, T. H. *Microporous Mesoporous Mater.* **2008**, *113*, 499-510.
(36) Cong, H. L.; Zhang, J. M.; Radosz, M.; Shen, Y. Q. *J. Membr. Sci.* **2007**, *294*, 178-185.
(37) Tenne, R.; Seifert, G. *Annu. Rev. Mater. Res.* **2009**, *39*, 387-413.
(38) Rao, C. N. R.; Govindaraj, A. *Adv. Mater.* **2009**, *21*, 4208-4233.
(39) Farmer, V. C.; Fraser, A. R.; Tait, J. M. *J. Chem. Soc. Chem. Commun.* **1977**, 462-463.
(40) Wada, S. I.; Eto, A.; Wada, K. *J.Soil Sci.* **1979**, *30*, 347-352.
(41) Bursill, L. A.; Peng, J. L.; Bourgeois, L. N. *Philos. Mag. A* **2000**, *80*, 105-117.
(42) Mukherjee, S.; Bartlow, V. A.; Nair, S. *Chem. Mater.* **2005**, *17*, 4900-4909.
(43) Mukherjee, S.; Kim, K.; Nair, S. *J. Am. Chem. Soc.* **2007**, *129*, 6820-6826.
(44) Yucelen, G. I.; Choudhury, R. P.; Vyalikh, A.; Scheler, U.; Beckham, H. W.; Nair, S. *J. Am. Chem. Soc.* **2011**, *133*, 5397-5412.
(45) Bonelli, B.; Bottero, I.; Ballarini, N.; Passeri, S.; Cavani, F.; Garrone, E. *J. Catal.* **2009**, *264*, 15-30.
(46) Zang, J.; Chempath, S.; Konduri, S.; Nair, S.; Sholl, D. S. *J. Phys. Chem. Lett.* **2010**, *1*, 1235-1240.
(47) Borrego, T.; Andrade, M.; Pinto, M. L.; Silva, A. R.; Carvalho, A. P.; Rocha, J.; Freire, C.; Pires, J. *J. Colloid Interface Sci.* **2010**, *344*, 603-610.
(48) Kupiec, K.; Konieczka, P.; Namiesnik, J. *Crit. Rev. Anal. Chem.* **2009**, *39*, 60-69.
(49) McMorn, P.; Hutchings, G. J. *Chem. Soc. Rev.* **2004**, *33*, 108-122.
(50) De Vos, D. E.; Dams, M.; Sels, B. F.; Jacobs, P. A. *Chem. Rev.* **2002**, *102*, 3615-3640.
(51) Choi, J. H.; Cho, Y. W.; Ha, W. S.; Lyoo, W. S.; Lee, C. J.; Ji, B. C.; Han, S. S.; Yoon, W. S. *Polym. Int.* **1998**, *47*, 237-242.
(52) NIST Mass Spec Data Center, S. E. S., director, "Mass Spectra" in NIST Chemistry WebBook, NIST Standard Reference Database Number 69, Eds. P.J. Linstrom and W.G. Mallard, National Institute of Standards and Technology, Gaithersburg MD, 20899, http://webbook.nist.gov, (retrieved January 25, 2010). .
(53) Bronnimann, C. E.; Zeigler, R. C.; Maciel, G. E. *J. Am. Chem. Soc.* **1988**, *110*, 2023-2026.
(54) Liu, C. H. C.; Maciel, G. E. *J. Am. Chem. Soc.* **1996**, *118*, 5103-5119.
(55) Trebosc, J.; Wiench, J. W.; Huh, S.; Lin, V. S. Y.; Pruski, M. *J. Am. Chem. Soc.* **2005**, *127*, 3057-3068.
(56) Eckert, H.; Yesinowski, J. P.; Silver, L. A.; Stolper, E. M. *J. Phys. Chem.* **1988**, *92*, 2055-2064.
(57) Yesinowski, J. P.; Eckert, H.; Rossman, G. R. *J Am. Chem. Soc.* **1988**, *110*, 1367-1375.
(58) Vega, A. J.; Scherer, G. W. *J. Non-Cryst. Solids* **1989**, *111*, 153-166.
(59) Barron, P. F.; Wilson, M. A.; Campbell, A. S.; Frost, R. L. *Nature* **1982**, *299*, 616-618.
(60) Mackenzie, K. J. D.; Bowden, M. E.; Brown, I. W. M.; Meinhold, R. H. *Clays Clay Miner.* **1989**, *37*, 317-324.

(61) Goodman, B. A.; Russell, J. D.; Montez, B.; Oldfield, E.; Kirkpatrick, R. J. *Phys. Chem. Miner.* **1985**, *12*, 342-346.
(62) Wada, S. I.; Wada, K. *Clay Miner.* **1977**, *12*, 289-298.
(63) Abidin, Z.; Matsue, N.; Henmi, T. *J. Comput. Aided Mater. Des.* **2007**, *14*, 5-18.
(64) Lippmaa, E.; Magi, M.; Samoson, A.; Engelhardt, G.; Grimmer, A. R. *J. Am. Chem. Soc.* **1980**, *102*, 4889-4893.
(65) Merzbacher, C. I.; McGrath, K. J.; Higby, P. L. *J. Non-Cryst. Solids* **1991**, *136*, 249-259.
(66) Akitt, J. W. *Prog. Nucl. Magn. Reson. Spectrosc.* **1989**, *21*, 1-149.
(67) Gilson, J. P.; Edwards, G. C.; Peters, A. W.; Rajagopalan, K.; Wormsbecher, R. F.; Roberie, T. G.; Shatlock, M. P. *J. Chem. Soc. Chem. Commun.* **1987**, 91-92.
(68) Haddix, G. W.; Narayana, M.; Gillespie, W. D.; Georgellis, M. B.; Wu, Y. *J. Am. Chem. Soc.* **1994**, *116*, 672-674.
(69) Schmucker, M.; MacKenzie, K. J. D.; Schneider, H.; Meinhold, R. *J. Non-Cryst. Solids* **1997**, *217*, 99-105.
(70) Farnan, I.; Dupree, R.; Forty, A. J.; Jeong, Y. S.; Thompson, G. E.; Wood, G. C. *Philos. Mag. Lett.* **1989**, *59*, 189-195.
(71) Ingram-Jones, V. J.; Slade, R. C. T.; Davies, T. W.; Southern, J. C.; Salvador, S. *J. Mater. Chem.* **1996**, *6*, 73-79.
(72) Luan, Z. H.; Cheng, C. F.; He, H. Y.; Klinowski, J. *J. Phys. Chem.* **1995**, *99*, 10590-10593.
(73) Man, P. P.; Klinowski, J.; Trokiner, A.; Zanni, H.; Papon, P. *Chem. Phys. Lett.* **1988**, *151*, 143-150.
(74) Sing, K. S. W.; Everett, D. H.; Haul, R. A. W.; Moscou, L.; Pierotti, R. A.; Rouquerol, J.; Siemieniewska, T. *Pure Appl. Chem.* **1985**, *57*, 603-619.
(75) Creton, B.; Bougeard, D.; Smirnov, K. S.; Guilment, J.; Poncelet, O. *J. Phys. Chem. C* **2008**, *112*, 10013-10020.
(76) Guimaraes, L.; Enyashin, A. N.; Frenzel, J.; Heine, T.; Duarte, H. A.; Seifert, G. *ACS Nano* **2007**, *1*, 362-368.
(77) Alvarez-Ramirez, F. *Phys. Rev. B* **2007**, *76*.
(78) Hoshino, H.; Urakawa, H.; Donkai, N.; Kajiwara, K. *Polym. Bull.* **1996**, *36*, 257-264.
(79) Cambedouzou, J.; Pichot, V.; Rols, S.; Launois, P.; Petit, P.; Klement, R.; Kataura, H.; Almairac, R. *Eur. Phys. J. B* **2004**, *42*, 31-45.
(80) Kawasaki, S.; Matsuoka, Y.; Yokomae, T.; Nojima, Y.; Okino, F.; Touhara, H.; Kataura, H. *Carbon* **2005**, *43*, 37-45.
(81) Kawasaki, S.; Hara, T.; Yokomae, T.; Okino, F.; Touhara, H.; Kataura, H.; Watanuki, T.; Ohishi, Y. *Chem. Phys. Lett.* **2006**, *418*, 260-263.
(82) Brunauer, S.; Emmett, P. H.; Teller, E. *J. Am. Chem. Soc.* **1938**, *60*, 309-319.
(83) Lippens, B. C.; Deboer, J. H. *J. Catal.* **1965**, *4*, 319-323.
(84) Cape, J. A.; Kibby, C. L. *J. Colloid Interface Sci.* **1990**, *138*, 515-520.
(85) Scherdel, C.; Reichenauer, G.; Wiener, M. *Microporous Mesoporous Mater.* **2010**, *132*, 572-575.
(86) Kakei, K.; Ozeki, S.; Suzuki, T.; Kaneko, K. *Journal of the Chemical Society-Faraday Transactions* **1990**, *86*, 371-376.
(87) Harkins, W. D.; Jura, G. *J. Am. Chem. Soc.* **1944**, *66*, 1362-1366.

(88) Deboer, J. H.; Lippens, B. C.; Linsen, B. G.; Broekhof.Jc; Vandenhe.A; Osinga, T. J. *J. Colloid Interface Sci.* **1966**, *21*, 405-414.
(89) Rols, S.; Almairac, R.; Henrard, L.; Anglaret, E.; Sauvajol, J. L. *European Physical Journal B* **1999**, *10*, 263-270.
(90) Bendiab, N.; Almairac, R.; Rols, S.; Aznar, R.; Sauvajol, J. L.; Mirebeau, I. *Phys. Rev. B* **2004**, *69*, 195415.
(91) Bachmann, S.; Wang, H.; Albert, K.; Partch, R. *J. Colloid Interface Sci.* **2007**, *309*, 169-175.
(92) El Rassy, H.; Pierre, A. C. *J. Non-Cryst. Solids* **2005**, *351*, 1603-1610.
(93) Hair, M. L.; Hertl, W. *J. Phys. Chem.* **1969**, *73*, 2372-2378.
(94) Low, M. J. D.; Severdia, A. G.; Chan, J. *J. Colloid Interface Sci.* **1982**, *86*, 111-118.
(95) Sindorf, D. W.; Maciel, G. E. *J. Am. Chem. Soc.* **1981**, *103*, 4263-4265.
(96) Sindorf, D. W.; Maciel, G. E. *J. Am. Chem. Soc.* **1983**, *105*, 3767-3776.
(97) Kang, D.-Y.; Zang, J.; Wright, E. R.; McCanna, A. L.; Jones, C. W.; Nair, S. *ACS Nano* **2010**, *4*, 4897-4907.
(98) Fyfe, C. A.; Feng, Y.; Grondey, H.; Kokotailo, G. T.; Gies, H. *Chem. Rev. (Washington, DC, U. S.)* **1991**, *91*, 1525-1543.
(99) Field, L. D.; Sternhell, S. *Analytical NMR*; Wiley: Chichester ;, 1989.
(100) Clark, J. C.; Barnes, C. E. *Chem. Mater.* **2007**, *19*, 3212-3218.
(101) Shimizu, H.; Watanabe, T.; Henmi, T.; Masuda, A.; Saito, H. *Geochem. J.* **1988**, *22*, 23-31.
(102) Wilson, M. A.; Wada, K.; Wada, S. I.; Kakuto, Y. *Clay Miner.* **1988**, *23*, 175-190.
(103) Cejka, J.; Bekkum, H. v. *Zeolites and ordered mesoporous materials : progress and prospects : the 1st FEZA School on Zeolites, Prague, Czech Republic, August 20-21, 2005*; 1st ed. ed.; Elsevier: Amsterdam ;, 2005.
(104) Mooney, R. W.; Keenan, A. G.; Wood, L. A. *J. Am. Chem. Soc.* **1952**, *74*, 1367-1371.
(105) Stromme, M.; Mihranyan, A.; Ek, R.; Niklasson, G. A. *J. Phys. Chem. B* **2003**, *107*, 14378-14382.
(106) Tomczak, E.; Kaminski, W. *Drying Technol.* **2009**, *27*, 1286-1291.
(107) Socrates, G. *Infrared and Raman characteristic group frequencies : tables and charts*; 3rd ed. ed.; Wiley: Chichester ;, 2001.
(108) Bottero, I.; Bonelli, B.; Ashbrook, S. E.; Wright, P. A.; Zhou, W.; Tagliabue, M.; Armandi, M.; Garrone, E. *Phys. Chem. Chem. Phys.* **2011**, *13*, 744-750.
(109) Holland, G. P.; Alam, T. M. *Phys. Chem. Chem. Phys.* **2005**, *7*, 1739-1742.
(110) Grey, C. P.; Vega, A. J. *J. Am. Chem. Soc.* **1995**, *117*, 8232-8242.
(111) Kassaee, M. H.; Sholl, D. S.; Nair, S. *The Journal of Physical Chemistry C* **2012**, *115*, 19640-19646.
(112) Maxwell, J. C. *A treatise on electricity and magnetism*; Unabridged 3d ed. ed.; Dover Publications: New York :, 1954.
(113) Hashemifard, S. A.; Ismail, A. F.; Matsuura, T. *J. Membr. Sci.* **2010**, *347*, 53-61.
(114) Hamilton, R. L.; Crosser, O. K. *Ind. Eng. Chem. Fund.* **1962**, *1*, 187-191.
(115) Das, S. K.; Choi, S. U. S.; Patel, H. E. *Heat Transfer Eng.* **2006**, *27*, 3-19.
(116) Fan, Z. H.; Advani, S. G. *Polymer* **2005**, *46*, 5232-5240.
(117) Zimmerman, C. M.; Singh, A.; Koros, W. J. *J. Membr. Sci.* **1997**, *137*, 145-154.

(118) Chung, T.-S.; Jiang, L. Y.; Li, Y.; Kulprathipanja, S. *Prog. Polym. Sci.* **2007**, *32*, 483-507.
(119) Guan, H.-M.; Chung, T.-S.; Huang, Z.; Chng, M. L.; Kulprathipanja, S. *J. Membr. Sci.* **2006**, *268*, 113-122.
(120) Caro, J.; Noack, M.; Kolsch, P.; Schafer, R. *Microporous Mesoporous Mater.* **2000**, *38*, 3-24.
(121) Stern, S. A. *J. Membr. Sci.* **1994**, *94*, 1-65.
(122) Robeson, L. M. *Current Opinion in Solid State & Materials Science* **1999**, *4*, 549-552.
(123) Cong, H. L.; Radosz, M.; Towler, B. F.; Shen, Y. Q. *Sep. Purif. Technol.* **2007**, *55*, 281-291.
(124) Qiu, S.; Wu, L. G.; Pan, X. J.; Zhang, L.; Chen, H. L.; Gao, C. J. *J. Membr. Sci.* **2009**, *342*, 165-172.
(125) Kim, S.; Chen, L.; Johnson, J. K.; Marand, E. *J. Membr. Sci.* **2007**, *294*, 147-158.
(126) Tanaka, K.; Kita, H.; Okano, M.; Okamoto, K. *Polymer* **1992**, *33*, 585-592.
(127) Cecopieri-Gomez, M. L.; Palacios-Alquisira, J.; Dominguez, J. M. *J. Membr. Sci.* **2007**, *293*, 53-65.
(128) Keskin, S. *The Journal of Physical Chemistry C* **2010**, *114*, 13047-13054.
(129) Keskin, S.; Sholl, D. S. *Energy Environ. Sci.* **2010**, *3*, 343-351.
(130) Sridhar, S.; Smitha, B.; Aminabhavi, T. M. *Sep. Purif. Rev.* **2007**, *36*, 113-174.
(131) Houde, A. Y.; Krishnakumar, B.; Charati, S. G.; Stern, S. A. *J. Appl. Polym. Sci.* **1996**, *62*, 2181-2192.
(132) Qian, X.-F.; Yin, J.; Huang, J.-C.; Yang, Y.-F.; Guo, X.-X.; Zhu, Z.-K. *Mater. Chem. Phys.* **2001**, *68*, 95-97.
(133) Chu, K.; Wu, Q.; Jia, C.; Liang, X.; Nie, J.; Tian, W.; Gai, G.; Guo, H. *Composites Science and Technology* **2010**, *70*, 298-304.
(134) Jain, R.; Minus, M. L.; Chae, H. G.; Kumar, S. *Macromol. Mater. Eng.* **2010**, *295*, 742-749.
(135) Glatter, O. *J. Appl. Crystallogr.* **1980**, *13*, 7-11.
(136) Glatter, O.; Kratky, O. *Small angle x-ray scattering*; Academic Press: London ;, 1982.
(137) Morita, T.; Hatakeyama, Y.; Nishikawa, K.; Tanaka, E.; Shingai, R.; Murai, H.; Nakano, H.; Hino, K. *Chem. Phys.* **2009**, *364*, 14-18.
(138) Pedersen, J. S. *Adv. Colloid Interface Sci.* **1997**, *70*, 171-210.
(139) Biswas, K.; Das, B.; Rao, C. N. R. *J. Phys. Chem. C* **2008**, *112*, 2404-2411.
(140) Wang, B. N.; Bennett, R. D.; Verploegen, E.; Hart, A. J.; Cohen, R. E. *J. Phys. Chem. C* **2007**, *111*, 17933-17940.
(141) Oster, G.; Riley, D. P. *Acta Crystallographica* **1952**, *5*, 272-276.
(142) Demontis, P.; Jobic, H.; Gonzalez, M. A.; Suffritti, G. B. *J. Phys. Chem. C* **2009**, *113*, 12373-12379.
(143) Chapman, P. D.; Oliveira, T.; Livingston, A. G.; Li, K. *J. Membr. Sci.* **2008**, *318*, 5-37.
(144) Van Baelen, D.; Van der Bruggen, B.; Van den Dungen, K.; Degreve, J.; Vandecasteele, C. *Chem. Eng. Sci.* **2005**, *60*, 1583-1590.
(145) Kang, D.-Y.; Jones, C. W.; Nair, S. *J. Membr. Sci.* **2011**, *381*, 50-63.

(146) Zhang, Q. G.; Liu, Q. L.; Zhu, A. M.; Xiong, Y.; Ren, L. *J. Membr. Sci.* **2009**, *335*, 68-75.
(147) Assender, H. E.; Windle, A. H. *Polymer* **1998**, *39*, 4295-4302.
(148) Ricciardi, R.; Auriemma, F.; De Rosa, C.; Laupretre, F. *Macromolecules* **2004**, *37*, 1921-1927.
(149) Voelkel, R. *Angew. Chem., Int. Ed.* **1988**, *27*, 1468-1483.
(150) Gabrielse, W.; Gaur, H. A.; Feyen, F. C.; Veeman, W. S. *Macromolecules* **1994**, *27*, 5811-5820.
(151) Bai, S.; Hu, J. Z.; Pugmire, R. J.; Grant, D. M.; Taylor, C. M. V.; Rubin, J. B.; Peterson, E. J. *Macromolecules* **1998**, *31*, 9238-9246.
(152) Ibbett, R. N. *NMR spectroscopy of polymers*; 1st ed. ed.; Blackie Academic & Professional: London ;, 1993.
(153) Rasburn, J.; Seker, F.; Kulbaba, K.; Klein, P. G.; Manners, I.; Vancso, G. J.; Macdonald, P. M. *Macromolecules* **2001**, *34*, 2884-2891.
(154) Konduri, S.; Mukherjee, S.; Nair, S. *Phys. Rev. B* **2006**, *74*, 033401.
(155) Konduri, S.; Mukherjee, S.; Nair, S. *ACS Nano* **2007**, *1*, 393-402.
(156) Kang, D.-Y.; Tong, H. M.; Zang, J.; Choudhury, R. P.; Sholl, D. S.; Beckham, H. W.; Jones, C. W.; Nair, S. *ACS Appl. Mater. Interfaces* **2012**, *4*, 965-976.
(157) Yamamoto, K.; Otsuka, H.; Takahara, A. *Polym. J.* **2007**, *39*, 1-15.
(158) Jiravanichanun, N.; Yamamoto, K.; Irie, A.; Otsuka, H.; Takahara, A. 2009, p 885-888.
(159) Yamamoto, K.; Otsuka, H.; Wada, S. I.; Sohn, D.; Takahara, A. *Polymer* **2005**, *46*, 12386-12392.
(160) Wang, R. K.; Reeves, R. D.; Ziegler, K. J. *J. Am. Chem. Soc.* **2007**, *129*, 15124-15125.
(161) Wang, R. K.; Park, H.-O.; Chen, W.-C.; Silvera-Batista, C.; Reeves, R. D.; Butler, J. E.; Ziegler, K. J. *J. Am. Chem. Soc.* **2008**, *130*, 14721-14728.
(162) Maillet, P.; Levard, C.; Spalla, O.; Masion, A.; Rose, J.; Thill, A. *Phys. Chem. Chem. Phys.* **2011**, *13*, 2682-2689.
(163) de Heer, W. A.; Bacsa, W. S.; Chatelain, A.; Gerfin, T.; Humphreybaker, R.; Forro, L.; Ugarte, D. *Science* **1995**, *268*, 845-847.
(164) Kim, S.; Jinschek, J. R.; Chen, H.; Sholl, D. S.; Marand, E. *Nano Lett.* **2007**, *7*, 2806-2811.
(165) Ryi, S.-K.; Park, J.-S.; Hwang, K.-R.; Lee, C.-B.; Lee, S.-W. *Int. J. Hydrogen Energy* **2011**, *36*, 13776-13780.
(166) Zhang, B. Q.; Wang, C.; Lang, L.; Cui, R. L.; Liu, X. F. *Adv. Funct. Mater.* **2008**, *18*, 3434-3443.
(167) Clausi, D. T.; Koros, W. J. *J. Membr. Sci.* **2000**, *167*, 79-89.